Stability and Motion of Foams and Films in confined Geometries

by
Wiebke Drenckhan

FOAM PHYSICS
at Trinity College Dublin

A Thesis submitted to
The University of Dublin
Trinity College
for the degree of

Doctor of Philosophy
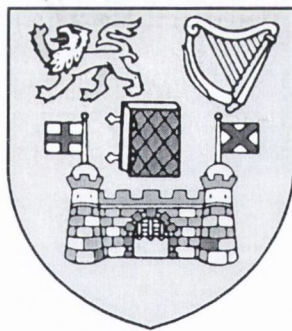
DEPARTMENT OF PHYSICS
TRINITY COLLEGE
UNIVERSITY OF DUBLIN

2005
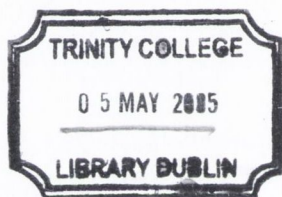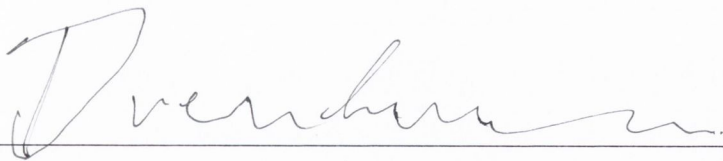
Declaration

This thesis has not been submitted as an exercise for a degree at any other University.

Except where otherwise stated, the work described herein has been carried out by the author alone.

This thesis may be borrowed or copied upon request with the permission of the Librarian, Trinity College Dublin, University of Dublin. The copyright belongs jointly to the University of Dublin and Wiebke Drenckhan.

Wiebke Drenckhan   Dublin 10.03.2005

Summary

The last 20 years of research in the physics of foams display the development of a thorough understanding of dry and static foams. In the realm of wet and dynamic foams, however, many interesting and puzzling effects have been observed experimentally but lack theoretical explanation. It has become clear at this stage that a mere extension of existing theories is not sufficient, but that new approaches have to be taken to establish a more complete understanding of dynamic effects in foams.

This thesis aims at providing a new angle on foams by establishing a road map of effects encountered upon leaving the familiar ground of dry and static foams. It proceeds by establishing exciting new aspects related to the structure of foams, before investigating the fluid dynamic properties of their individual building blocks and the rheological properties of some ordered foam structures. The emphasis of this research is on experiments with systems of quasi-two-dimensional nature. Wherever possible, these are accompanied by computer simulations and theoretical considerations. This "Trinity approach" has proven extraordinarily successful.

Within the realm of static foams, it is demonstrated how mono-layers of bubbles between angled or non-planar surfaces can be employed to beautifully reproduce conformal transformations of the honeycomb pattern.

Studies of the fluid dynamic properties of individual surface Plateau borders and soap films shed light on the influence of the physical properties of the gas/liquid interfaces on drainage in foams. By studying high drainage rates, elucidating observations and measurements tie in well to break away from the traditional picture of foam drainage. Beautifully regular and reproducible meandering instabilities of extended Plateau borders establish a new angle on the stability of foams.

Investigation of the flow of ordered foam structures in confined geometries does not only provide ideal test beds for models of viscous foam flow (Viscous Froth Model), but offers great potential for technological applications in the real of microfluidics. We termed this novel concept of discrete fluid and sample handling "Discrete Microfluidics".

Acknowledgments/Foreword

It is interesting, how documents like these are always written "backwards": the author writes last what the reader is going to encounter first. To a certain extent, these acknowledgments symbolise a door which irretrievably closes a stage of one's life. Closing this door at the beginning of the thesis is like demonstrating that one is not departing from this stage by turning the back to it, but by facing and embracing it.

These pages seem the only space left to sneak in some very personal thoughts. On the hunt for objectiveness modern science provides very little room for the scientist himself, his emotions, excitement, doubts, personal insights or sense of beauty.

"All unnecessary rubbish" said one of my colleagues whilst crossing out all the words like "beautiful" or "exciting" in my papers.

We all know that doing a PhD is above all a very personal struggle. It is not only a link, but a very important "switch" between the student and the professional life. It is the time to find out what science means to you in a philosophical and practical sense. And who would not agree that the key qualities of a good scientist are everything else but objective: creativity, curiosity, passion, intuition, ... In my opinion, it is not the universe, which is at the centre of science. It is the human being and its struggle to understand and describe the universe. Very little of this shows through in our literature, which for me is an important reason for the decreasing popularity of science. The excessive use of romantic and philosophical quotations in scientific books and talks is a desperate sign of people trying to make some space for their emotional outlook on their work. Why, however, is it accepted to put a famous person's poem into a physics book, but not your own? Even though I am writing this, I have not dared myself to break this pattern (and would not know how to, at this stage); except for

implementing some of my drawings. The three years of working on this thesis and in science, however, have left me with the strong desire to look for a way out of this misery.

"It must be such a great excitement to finish your thesis!", people say.

They are disappointed that I cannot really agree. It is a great excitement to *be doing* the PhD. One probably never again gets the chance to spend three years exploring the world of physics in an almost childlike manner; and to have time and plenty of opportunities to find out what science means to you in general. The thesis itself is in this sense rather disappointing, as it shows very little of the really important processes going on during the years of working towards it. Very little is said about the doubts and the excitement, the many wrong turns you took, the many small and big moments of enlightenment, the periods when you simply did not care any more, and those when all you wanted was to pitch a tent in the lab.

Being a scientist is not just a job, it is a way of being. The years of working on the PhD are the time during which this way of life is being tediously established. The "Who am I, what do I want?" – questions from childhood are haunting you again. And just like then, you spend a lot of time learning to walk on your own feet and to develop an independent mind. And those who never fell during this process probably never learned how to walk.

One pretends in the thesis that its subject is the centre of the universe. But everybody knows (including yourself) that it is not. However, it is one of many doors to a better understanding of our universe. And for me, the physics of foams has indeed been a particularly beautiful and exciting one.

I have no shame to confess that the most important part of my PhD has been the collaboration or general interaction with some amazing scientists who inspired me on various levels, of which the physics of foams was only a part. Becoming a good scientist, in my opinion, means learning to broaden your mind. By sharing their time and most of all their thoughts with me, these people have given me invaluable presents on my way. I cannot and will not single out people, apart from one: my supervisor

Denis Weaire. He has been much more than a supervisor by re-evoking my love for science. Like many other people, I had lost this love during my years at university. When I came to Dublin, I only wanted to do a Masters to make sure that I would not ask myself for the rest of my life what it would have been like to do research. Working with Denis gave me the chance to absorb his energy and creativity, but most of all his childlike fascination for this world as a whole. At the same time, I found the world of science opening up in front of me as a result of him supporting every aspect of my very personal exploration of it. This greatly helped me to realise that the kind of science and scientists I had set out to look for when I decided to study physics did exist after all. And here I mean science in its very broad sense: an inquisitive approach to the world, which includes arts just as much as philosophy or mathematics. In this sense, this PhD marks a return. A return of someone who knows much better what she wants, because she has come through a long period of doubt.

I will never be able to repay this. But I can and will always try to give to students what he – and many other people who I got a chance to meet and to work with – have given to me. Thank you.

Somebody said "Be careful with the acknowledgments. They are the only part of the thesis which everybody is going to read, because they are all hoping to find their names in it".

But is it really possible to single out people? To me, the security man at the gate, who starts my day with a "Morning, luv!" and a smile, or the cleaning ladies who shared their cigarettes with me on my night shifts, are just as important as the secretaries, technicians or academics who helped solving difficult problems. Where would I start, and where would I stop, if I wanted to go through all the wonderful people in this department and college, who, through their unconditional technical and personal support, have created a place I simply loved working in for the last three years? Starting from my students, the technical and administrative staff, to the people in my group and my office, and the academics in the department.

A fulfilled private life is just as important for the success of a PhD as the time in College itself. The girls from my volleyball team have been like my sisters, the club and the Irish volleyball scene as a whole like a big family.

Above all I would like to thank my dear friends in and outside of Ireland for their unconditional love, support and inspiration; for allowing me to look at this world through their eyes and for making me feel home in my house, in Dublin, in Ireland and in this world as a whole!

My gratitude and love for my family is beyond words!

What I hope is that I do not need to acknowledge individual people in this thesis, but that I have been and will be able to show my gratitude, appreciation and love in my personal and professional interaction with every single one of them every day. Thank you!

Last but not least, I would like to thank the German National Merit Foundation. They have not only supported me financially throughout my studies and PhD. They have most of all provided a fascinating environment, in which like-minded people from all fields could get together to find inspiration and broaden their minds.

Would I do a PhD again? YES!

Would I do anything differently? A LOT!

Would I want to go back? NO!

Because there is a whole new world opening up in front of me which I am very much looking forward to explore.

What I wish for myself? That I get much wiser, but never grow up...

Publications

W. Drenckhan, F. Elias, S. Hutzler, D. Weaire, E. Janiaud and J.-C. Bacri, Bubble size control and measurement in the generation of ferrofluid foams, *J. App. Phys.*, 93(12):10078–10083, 2003

W. Drenckhan, S. Cox and D. Weaire, The demonstration of conformal maps with two-dimensional foams, *Eur. J. Phys.*, 25:429–438, 2004

W. Drenckhan, D. Weaire and S. Gatz, Wave patterns of a rivulet of surfactant solution in a Hele-Shaw cell, *Phys. Fluids*, 16(8):3115–3121, 2004

W. Drenckhan, S. Hutzler and D. Weaire, Foam physics: the simplest example of soft condensed matter, Conference procedings "Modern Trends of Physics Research 2004", AIP, 2004

W. Drenckhan, S. Cox and D. Weaire, Rheology of oredered foam structures - on the way to discrete microfluidics, to appear in *Colloids and Surfaces A: Physicochemical and Engineering Aspects*, 2005

W. Drenckhan and D. Weaire, Flow in vertical Plateau border: a reluctance to coalesce", submitted to *Eur. Phys. J. E*

S. Hutzler, N. Peron, D. Weaire and W. Drenckhan, The Foam/Emulsion Analogy in Structure and Drainage, *Eur. Phys. J. E*, 14:381–386, 2004

D. Weaire, S. Hutzler, W. Drenckhan, S. Cox, M.-D. Alonso and W. Drenckhan, The fluid dynamics of foams, *J. Phys.: Condens. Matter*, 15:65–73,2003

E. Colle, W. Drenckhan and N. Rivier, The Joule-Thompson throttling fof ordered foams, to appear in *Colloids and Surfaces A: Physicochemical and Engineering Aspects*, 2005

Contents

Chapter 1

Introduction

1.1 Introduction to foams and scope of this thesis

Foams have found their way into many areas of our everyday lives. The types they come in are as versatile as the applications they are used for: soaps, food, beverages, fire fighting, refined oil recovery, upholstery, insulation, metal foams, foam flotation or foam fractionation.

Their popularity, however, is not only a result of their usefulness; foams provide a very accessible system which interlinks a plethora of subjects ranging from elegant mathematical theories via fluid dynamics and chemistry to the aesthetic beauty of pattern formation and growth. The physics of foams is therefore a fascinating conglomerate of interdisciplinary research, bringing together a variety of fields and reaching out into just as many. Insights from the physics of foams have been applied to various subjects dealing with cellular structures and pattern formation. Particularly popular examples are found in biology, rock formations in geography, or the cellular distribution of galaxies in the universe [125, 46, 97, 93, 8].

Intermingled with all these aspects is certainly the human fascination for the dazzling beauty and graciousness of soap bubbles in general, which for most of us started very early in our lives - as demonstrated in figure 1.1.

Traditionally the subject of foams was mostly studied by engineers. About 2 decades ago, however, the attention of physicists was drawn to this field, when a growing interest in increasingly complex foam applications began to demand a much better understanding of their physical properties.
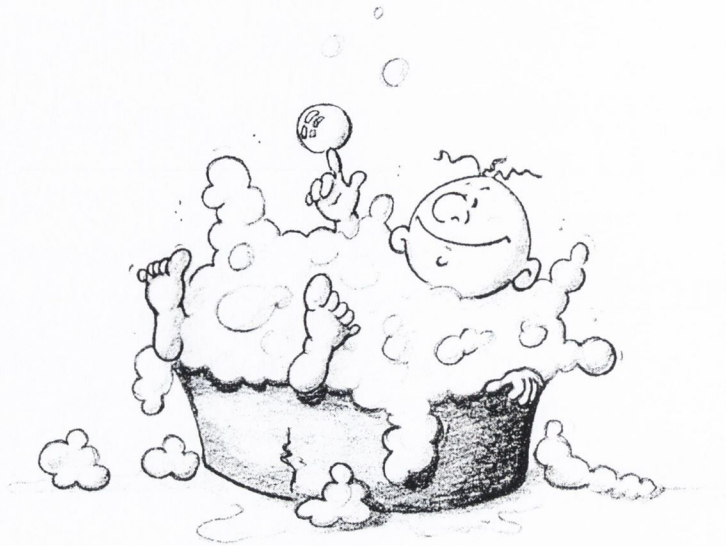
Figure 1.1: The fascination of bubbles and foams begins at an early age for many people.
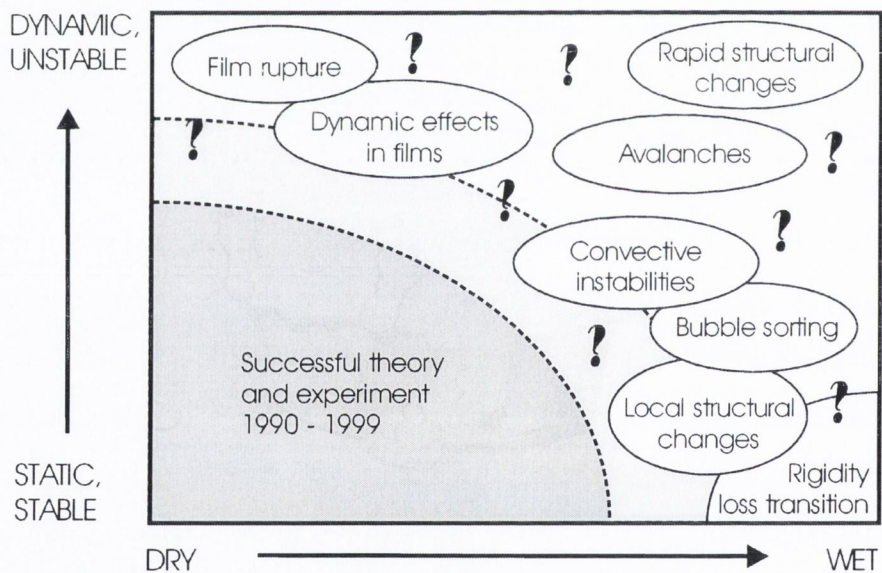
Figure 1.2: A phase diagram of our current understanding of foams and the attempted outreach of this thesis (light gray area). The physics of dry (very little liquid) and static/stable foams is very well understood and theoretically grounded. In the regime of wet and dynamic/unstable foams a number of striking observations have been made, which yet await theoretical explanation. It is clear at this stage, that a mere extension of existing theories will not be sufficient to account for effects encountered in this regime.

The last 20 years of foam research display the development of a thorough understanding of dry and static/stable foams (Fig. 1.2). This was greatly enhanced through the availability of increasing computer power and the application of successful computational models [125, 46, 97]. In the regime of wet and dynamic foams, however, a wide range of complex and puzzling phenomena has been experimentally observed and studied [126], but could not be included into the existing theories. After several, rather unsuccessful, attempts of merely extending the existing theories, it seems clear that the physics of foams is now at some borderline that demands new ideas incorporated into new models and theories. In order to succeed in this undertaking, researchers need to approach the subject from a new angle. The search for this new angle is very much at the heart of this thesis.

Until very recently, foams were mainly studied from a *macroscopic* point of view, which most of all ignored the subtle chemistry involved. It has become clear, however, that in order to proceed further, we will have to assume a *microscopic* approach by focusing on the dynamic properties of the individual building blocks of a foam. The understanding of these elements can then be put together to re-create the complex scenario of a complete foam in a "bottom-up" approach.

By employing this microscopic approach, this thesis aims at mapping out a range of effects encountered beyond the borderline (light gray area in Fig. 1.2) of the well understood physics of dry and static/stable foams (dark gray area in Fig. 1.2). From my journey through this unknown territory I have brought back plenty of surprising and unexpected observations. Most of them are reported and studied for the first time. This is very much in the spirit of this thesis, which I would like to consider an attempt to map out some of the yet unfamiliar terrain lying ahead of us, in which some of the painted scenarios have to remain fairly speculative. However, the frame they provide is necessary guidance and most of all a frame of reference for any further work. Maps like these are needed in order to decide which areas will be most vital to the understanding we are seeking, and to prepare the thorough scientific conquest of the yet unknown. Often it turns out in science that the more speculative some interpretations the better, as they challenge other researchers' efforts and attention. And even if they

are proven wrong, they will have fulfilled their purpose, namely to advance people's understanding of the field.

I begin this conquest in this chapter with an introduction to the basic properties of foams that will be required for an understanding of the following investigations. In order to establish a general overview of the relevance of the problems introduced in this thesis, I use this introduction to point towards the missing links or holes in the existing understanding of foams, which are then tackled separately in the remaining thesis.

Part I moves on the familiar grounds of "foam structure" by introducing new aspects of conformal transformations into the physics of two-dimensional foams. Part II crosses the border to wet and dynamic foams by focusing on microscopic aspects of the flow of liquid in foams. Part III focuses on the flow of foam itself.

During the first year of my PhD, I programmed a software tool to simulate liquid flow in a solidifying metal foam in order to support preparations of micro-gravity experiments in collaboration with the IFAM in Bremen. Since I have not used the program for scientific investigations myself, I have only attached a brief overview as Appendix A. The program itself can be found on the CD provided with this thesis.

In writing a document like this, there always arises the question of whether to use a personal or technical perspective and writing style. I believe that personal styles, implying the use of "I" and "we", are not only much more pleasant to read, but allow to distinguish in a much more straightforward way between what has been done and thought by the author and co-workers, and what is already generally accepted knowledge. Even though I have been the key driver of the work reported here, hardly any of it would have been possible without the constant interaction with other people in the science community and their input on practical and intellectual levels. This ranges from summer students, technical staff, colleagues and collaborators to my supervisor. For these reasons and to make the document more consistent I will use the term 'we" throughout the thesis.

1.2 Static foams

1.2.1 General properties of foams

Foams are two-phase systems consisting of a continuous liquid phase and a dispersed gaseous phase forming a closed cell structure. For many applications the liquid phase is chosen such that it solidifies after foam generation, which leads to *solid foams*. This thesis focuses on the physics of *liquid foams*, in particular *aqueous foams*, in which the continuous phase is water.

The total area of the gas/liquid interfaces separating the two phases can be understood to represent the energy of the foam. Like in any other physical system, this energy is at a minimum when the foam is in equilibrium and therefore determines the *topology* of its closed-cell structure. Most foams have a very complex structure and therefore an equally complex energy landscape. Hence, when dealing with foams – experimentally or computationally – we hardly ever encounter *global* energy minima. Only for simple cases can we find the structure that presents the absolute energy minimum of a system [122, 125, 28, 27]

The stability of foams is provided by the presence of *surface active agents* (" surfactants"), dissolved in the liquid phase. These are generally molecules which are attracted to the gas/liquid interface as a result of their amphiphilic nature, generated by a hydrophobic tail and a hydrophilic head. Research over the last decades has provided the community with a vast selection of different surfactants. These are commonly grouped into *non-ionic*, *anionic* (negatively charged), *cationic* (positively charged) and *amphoteric* (charge depends on pH level of solution). The presence of surfactants significantly reduces the interfacial tension, but more importantly prevents film rupture by steric (non-ionic surfactants) and/or electrostatic (ionic surfactants) repulsion.

A very important parameter in the description of foams is their *liquid fraction* ϕ, which is given by the volume fraction of the continuous phase. It has a significant effect on many physical properties of a foam and re-occurs in various parts of this thesis.

In the *wet limit* the bubbles of a foam are spherical and barely touch each other. In

The building blocks of:
3D foams   **2D** foams

continuous
phase
film

109.6°

120°
Plateau border

vertex

edge

120°

vertex
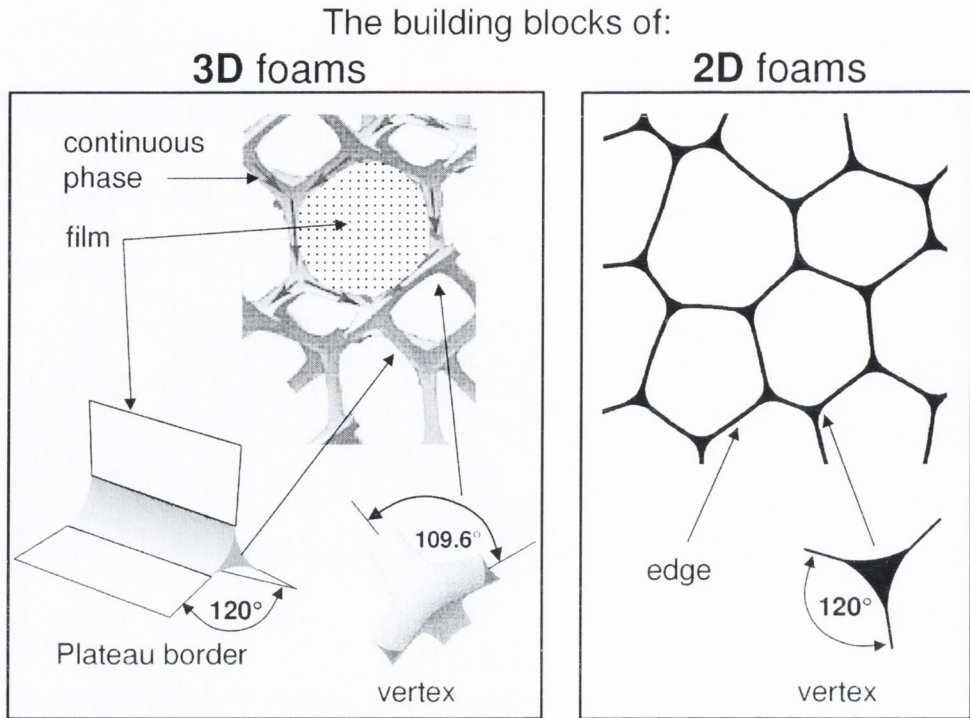
Figure 1.3: Overview of the building blocks and equilibrium properties of three-dimensional (3D) and two-dimensional (2D) foams. (Simulations by S. Cox and S. Hutzler)

the *dry limit* they form polyhedral cells, separated by thin films.

Despite the complex topology of a foam, the local equilibrium rules governing its structure are surprisingly simple. The essential building blocks of a dry foam and their equilibrium rules are show in Fig. 1.3 a). They can be described as follows:

1. **Films** are formed where bubbles touch. They consist of two gas/liquid interfaces separated by a thin layer of liquid. The mean curvature κ of such a film is related to the pressure drop Δp across it by

$$\Delta p = 2\gamma\kappa = 2\gamma(\kappa_1 + \kappa_2). \tag{1.1}$$

Here κ_1 and κ_2 are the two principle curvatures and γ is the surface tension. This equation is called the *Young-Laplace law* (or simply *Laplace law*) and lies at the heart of foam physics [137, 77].

2. **Plateau borders** are formed were films meet. In equilibrium it is always three films that meet at angles of $120°$ [95].
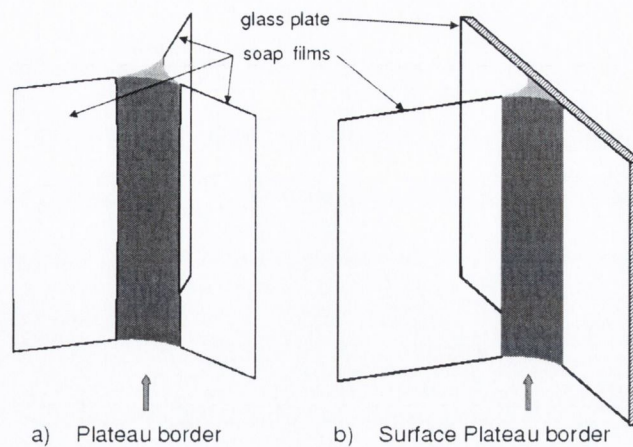
Figure 1.4: The two possible cases of Plateau borders in a foam: a) The *interior Plateau border*, which is formed where three films meet; and b) the *surface Plateau border* which is formed where a film is attached to a surface. Nearly all of the liquid transport in a foam occurs along these interior and exterior "channels". (Simulations by S. Cox.)

The three sections of the boundary of the cross-section of a Plateau border are arcs of circles whose radius of curvature is determined by the Laplace law (Equ. (1.1)), and therefore by the pressure difference between the liquid in the Plateau border and the gas in the adjoining bubble.

A special type of Plateau border (*surface Plateau border*) is formed where films are attached to surfaces (see Fig. 1.4 b)). In equilibrium the angle between the surface and the film is always $90°$.

The Plateau borders form a network of channels, which generally contains more than 99% of the total liquid content of a foam. Nearly all liquid transport, driven by gravity or a pressure drop, occurs along these channels. Therefore, understanding the fluid dynamic properties of these elegant "pipes" is a key to understanding the flow of liquid in foams. Part II of this thesis is devoted to this subject.

3. **Vertices** are the junctions formed where Plateau borders meet. Stable junctions are always four-fold with angles of $109.6°$ between any two borders. Like the Plateau borders, they are a vital part of the liquid network.

4. The ***energy*** of a foam is represented by the total area of its gas/liquid interfaces.

1.2.2   Two-dimensional foams

Many of the challenges of visualisation and analysis of complex foam structures can be met by working with *two-dimensional* (2D) cell structures. The building blocks and equilibrium rules of such 2D-foams are illustrated in Fig. 1.3 b) and can be described as follows.

1. Films are represented by ***edges*** of constant curvature κ (arcs of circles) given by the simplified Laplace law

$$\Delta p = 2\gamma\kappa, \tag{1.2}$$

   where Δp is the pressure difference across the edge.

2. Edges meet three-fold at angles of $120°$ at the *2D-**vertex***, which contains nearly all of the liquid phase. The geometry of the vertex is the same as that of the cross-section of a 3D-Plateau border. It is formed by three arcs of circles, whose curvatures are given by Equ. (1.2). Here, Δp is the pressure difference between the liquid in the vertex and the gas in the adjoining 2D-bubble.

3. The ***energy*** of a 2D foam is represented by the total line length of its one-dimensional gas/liquid interfaces.

A wet 2D foam of reasonably low liquid fraction can be thought of as a dry equilibrium foam "decorated" with appropriate liquid pockets at its vertices [123].

Experimentally, *quasi-2D* foams are generated by producing mono-layers of bubbles. This can be achieved by collecting bubbles on the surface of the surfactant solution (*Bragg raft* [14]), by trapping a layer of bubbles between the liquid surface and a plate (*Fatima* configuration), or by squeezing a layer of bubbles between two narrowly spaced plates (*Hele-Shaw* configuration).

The reduction of dimensions from three to two greatly reduces the complexity of a problem whilst leaving most of the significant physics untouched. Major discoveries in the physics of foams have been made with or guided by these simple "foam sandwiches" following the lead of Bragg and Nye [14] and Smith [113] [125, 19, 65].

A major strength of 2D systems is provided by the opportunity to guide experimental and theoretical approaches by computer simulations. With the availability of the powerful Surface Evolver Software by Brakke [16], this "Trinity approach" of combining experiment, theory and simulation (termed by Stefan Hutzler) has become fairly straightforward and has proven very successful over the recent years. Nearly all of the experiments reported in this thesis make use of this very fruitful approach in two dimensions. In Part I we explore the pattern formation of mono-layers of equal-volume bubbles between two non-planar surfaces. In Part II we investigate the properties of liquid flow through a single film in a Hele-Shaw configuration. In Part III we study the flow of quasi-2D foams in Hele-Shaw cells of specific geometries.

For a better understanding of the investigations reported in this thesis it is important to be aware of the peculiarities and approximative nature of 2D foam experiments, in which the third dimension may still play a significant role:

- As expressed in §1.2.1, films form surface Plateau borders where they are attached to (liquid or solid) surfaces. It is these Plateau borders that we see as edges in images, not the soap films as such.

- Gravitational effects acting perpendicular to the surface normal might still play a significant role in non-vertical systems by generating an asymmetry between the top and bottom Plateau borders.

- Films contained between non-parallel surfaces will have a non-zero curvature in the direction of the surface normal. This could have a significant effect on the measured 2D-curvature, which is in the surface plane. This is a result of the 3D Laplace law (Equ. (1.1)).

The specific implications of these effects are discussed in the respective chapters.

The definition of the liquid fraction of a quasi-2D foam is still an open problem which needs to be addressed rather urgently. Due to the 3D effects mentioned above, the 3D volume fraction of a 2D foam can only be an approximation of the apparent 2D liquid fraction. As most of the properties of a 2D foam are determined by the size of

its surface Plateau borders and vertices, much more thought will have to go into their quantitative description as a function of liquid content, cell geometry and bubble size.

Despite these limitations, however, the two-dimensional approach has proven extraordinarily successful in the understanding of foams and related systems and has provided scientists with very important stepping stones into the realm of 3D foams.

1.3   Dynamic foams

The dynamic aspects of the physics of foams can be grouped into two physically different phenomena: ***foam drainage*** and ***foam rheology***. Drainage (§1.3.1) deals with the flow of liquid within the network of Plateau borders, vertices and films in an otherwise static foam structure. Foam rheology (§1.3.2), on the contrary, focuses on flow of the foam itself. Naturally, both aspects are interlinked, particularly for wet foams and high liquid or foam flow rates. For most purposes, however, it has proven sufficient to focus on each aspect separately.

1.3.1   Foam drainage

Foam drainage describes how liquid is driven through a foam by gravity or pressure gradients. To a good approximation this process can be considered as the flow of liquid through the network of Plateau borders and vertices, neglecting the contribution of the thin films. For low liquid fractions ($\phi < 10\%$) this process is well described by the drainage equation [125, 71], which is essentially a non-linear diffusion equation.

It is important to distinguish between *free drainage* and *forced drainage*. In free drainage the foam is left to drain freely, whilst in forced drainage liquid is added at a constant flow rate at the top of the foam so that a steady state of flow is established in the foam.

For a long time neglected, it has been established in recent years that the dynamic properties of the gas/liquid interface have a significant influence on the drainage properties of a foam. Depending on the type of surfactant used to stabilise the foam, its interfacial mobility can range from *mobile* to *rigid*, resulting in plug-like or Poisseuille-like flow in the Plateau borders and vertices. This leads to two different types of

drainage. In foams with very mobile interfaces most of the energy is dissipated in the nodes. Hence, this type of drainage is called *node dominated* [71, 72]. In a foam with very rigid interfaces most of the dissipation occurs in the Plateau borders and is therefore called *Plateau border dominated* drainage [119, 128, 125]. Most cases lie between these limits.

Even though the existing drainage theories apply well to both extremes , we are yet in the process of establishing a description for intermediate cases [107, 42, 114, 108]. Two different approaches are currently being taken to establish this missing link. The *macroscopic approach* [108], which investigates the drainage of a bulk of foam, and the *microscopic approach* [73, 41], in which the flow in individual Plateau borders is at the centre of interest.

This thesis introduces studies of the microscopic type, in which the properties of a simple system of two surface Plateau borders connected by a thin film are investigated (Part II). We have exploited this system by studying it from various angles, focusing on different aspects of the microscopic flow properties and the stability of the Plateau borders (Chapter 4) and the connecting film (Chapter 5). Most of the introduced effects are reported for the first time and therefore await theoretical explanation. We do provide some theoretical key ideas.

We believe that with the insights gained from this thesis we can draw a bigger picture of microscopic effects in foams. These should be considered carefully for high drainage rates, as many of the reported observations and conclusions go well beyond the question of interface mobility. In particular, they challenge the traditionally held point of view that the liquid flow velocity is zero at the point where the film is attached to the Plateau border [78].

1.3.2 Foam rheology

The rheology of foams deals with the shearing flow of the foam itself. The interaction between the structure of the foam and its flow gives rise to interesting non-Newtonian effects. For instance, under small shear stress foams behave like elastic solids, whereas at large shear stress they behave like viscous liquids.
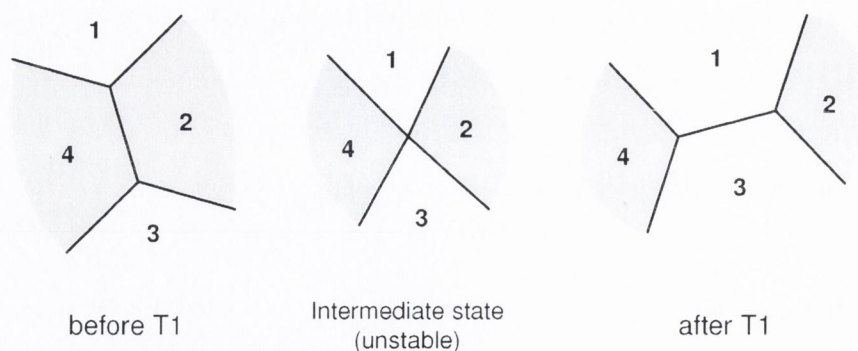
Figure 1.5: Neighbour switching ("T1") of bubbles in a 2D foam - the key process of topological rearrangements.

The apparent viscosity of a foam is related to two key aspects of its flow:

1. ***Topological rearrangements*** within the foam structure

   In our 2D geometry these occur via the neighbour-switching of bubbles. This is called a *T1* process, which is illustrated in Fig. 1.5. In a dry foam, the edge length between the vertices has to go to zero to initiate a T1. In a wet foam it is sufficient if the corners of the liquid loaded vertices touch. Hence, topological rearrangements occur more easily in a wet foam, which corresponds to a lower yield stress.

   In section §7.4.4, we introduce a device that can be used to study individual, successive T1 processes in a highly controlled manner.

2. ***Viscous dissipation*** of films (surface Plateau borders) sliding along container walls

   This effect is of particular importance in quasi-2D geometries as the ratio of the container surface area to the container volume is very large. The details of this dissipation mechanism have not yet been fully understood. But current attempts of modelling [19, 69] these processes seem to be converging well with accompanying experiments [20, 37]. We demonstrate this in detail in section §7.5 in Part III.

Part III of this thesis introduces experiments that provide a context in which several aspects of quasi-2D foam rheology can be studied in a tightly controlled, systematic

way. They involve ordered mono-disperse foam structures of a few bubbles only, which flow through specifically designed channel geometries of quasi-2D nature. These experiments can easily be modelled in computer simulations and therefore provide ideal testbeds for our theoretical understanding of the governing processes.

Not only do we believe that the introduced experiments and simulations will serve as excellent tools in providing keys to the understanding of foam rheology, but we see a very strong potential for commercial applications. Our systems provide methods for the highly controlled manipulation of gas (and liquid) samples, which may be very useful in a variety of applications in the chemical, medical or biological sector. Combining methods of sample manipulation (Chapter 7), sample volume control, sample detection and storage (Chapter 8) on small length scales, we introduce a novel technique within the realm of microfluidics, which we have termed *Discrete Microfluidics*.

Because much of our research in this area has been driven from this exciting applied (rather than fundamental) point of view, we retain this angle in Part III.

1.4 Interface dynamics

The dynamic properties of interfaces and the hydrodynamics of the adjacent fluid layer are strongly coupled and have become of increasing importance in many fields in physics and engineering. *Interface rheology* has therefore become an independent area of research [43, 106, 104].

Foams have a very large surface to volume ratio, and in particular a large surface to liquid volume ratio. The rheological properties of its interfaces should therefore be carefully evaluated in the study of its overall dynamic properties.

Because considerations of the interfacial properties re-occur throughout the thesis, this section is devoted to introducing some key aspects of this subject.

Interface rheology is described by four rheological parameters:

1. Interfacial dilational elasticity
2. Interfacial shear elasticity
3. Interfacial dilational viscosity
4. Interfacial shear viscosity η_S.

Of these, 1 and 4 are the most important for our purposes. The possible importance of 3 for foams is currently being discussed, but without any particular conclusions so far. Interfacial viscosity and elasticity have long been considered the same quantity by people like Plateau [95] or Boussinesq [13]. Intensive debates over the different nature of these effects started in the second half of the 20th century [79] and have now been settled with detailed theoretical description [43, 106, 104].

The ***interfacial shear viscosity*** η_s of a (Newtonian) interface in the x,y-plane is defined analogous to the bulk viscosity

$$\tau_{xy}^s = \eta_s \left(\frac{\partial v_y}{\partial x} + \frac{\partial v_x}{\partial y} \right), \tag{1.3}$$

where τ_{xy}^s is the interfacial shear stress tensor and $\frac{\partial v_y}{\partial x} + \frac{\partial v_x}{\partial y}$ is the interfacial shear rate. In the physics of wet foams this parameter plays an important role and is usually combined with the liquid viscosity η_l and the Plateau border radius r_{PB} in the dimensionless *mobility parameter* M [108],

$$M = \frac{\eta_l r_{PB}}{\eta_s}, \tag{1.4}$$

which is the inverse of the Boussinesq number B_0 [13].

The surface viscosity is determined by the kind of surfactant that is used to stabilise the foam. Small surfactant molecules generally make very mobile interfaces (large M), whereas chunky molecules like proteins or polymers generate very rigid interfaces (small M).

The ***interfacial dilational elasticity*** is a more complicated quantity, as it is linked to the concentration of surfactants adsorbed at the interface, which is in equilibrium with the bulk concentration. If an interface is expanded, the interfacial surfactant concentration is diluted temporarily until enough surfactant molecules are adsorbed from the bulk to re-establish equilibrium. The opposite happens upon compression. How long this takes depends on the adsorption/desorption time scales of the particular surfactant.

Since the surface tension γ depends on the interfacial surfactant concentration, the dynamic depletion or accumulation of surfactant molecules leads to a *dynamic surface*

tension. This in turn results in an elastic response of the interface. If the change of area occurs under quasi-static conditions, we call the associated parameter *Gibbs elasticity* E [52]:

$$E = \frac{d\gamma}{d\ln(A)} = A\frac{d\gamma}{dA}. \tag{1.5}$$

Most processes, however, are out of equilibrium processes leading to *Marangoni elasticity* [81].

The *Marangoni effect* refers to a broad variety of phenomena, generally describing interfacial flow driven by surface tension gradients. The most familiar type is related to the sensitivity of surface tension to temperature. This generates the well known interfacial swirling motion in soap films. Another equally important origin of surface tension gradients is the bulk fluid flow adjacent to the interface, dragging along the chunky surfactant molecules in the interface. This phenomenon is well known from bubbles rising in surfactant solution [47], where the viscous drag of the liquid on the gas/liquid interface leads to a re-distribution of surfactants from the top of the bubble to the bottom, hence generating Marangoni flows in the interface. We believe that this particular effect may be of importance for some of the observations reported in this thesis.

1.5 Some thoughts on surfactants

As mentioned in §1.2.1, surfactants govern the stability of a foam. Maximum stability is often reached by using subtle mixtures of ionic and non-ionic species, which have been extensively researched and optimised for the industry of washing detergents.

For most of our research up to date the specific chemistry of the surfactants has not been of importance. In search of maximum foam stability we have hence resorted to using commercial dish-washing detergents (*Fairy Liquid* by P&G [48]), even though its precise composition is, of course, a company secret.

Since some of the effects observed at the outset of the research leading to this thesis could only be reproduced using Fairy liquid, we decided to use the same detergent
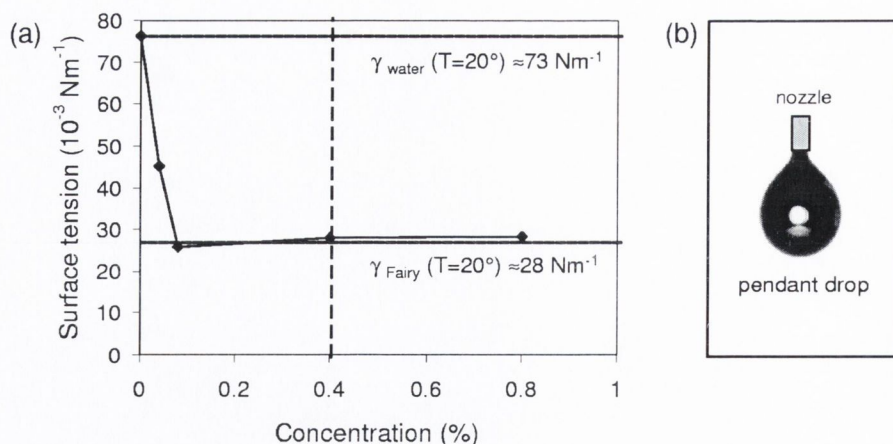
Figure 1.6: a) The surface tension of a solution of "Fairy" dish-washing detergent in de-ionised water as a function of its concentration, measured using the b) pendant drop technique [56]. A concentration of 0.4 % is used throughout the thesis.
[52]

(Fairy Series S402) throughout the whole thesis. This provides the opportunity to study the same system from various angles and hence gain a deeper understanding of its particular properties.

Figure 1.6 shows how the surface tension γ of a solution of Fairy dish-washing liquid (Fairy Series S402) in de-ionised water varies with detergent concentration. These measurements were conducted using the pendant drop technique [56]. The data shows that γ drops rapidly until the concentration reaches about 0.1% and remains constant above this value. It is a well known fact that only a minute bulk concentration is needed to reach the maximum possible concentration of surfactants adsorbed at the interface. Beyond a critical bulk concentration, which is called *critical micellar concentration* (CMC), all additionally added surfactant molecules remain in the bulk, where most of them agglomerate in micelles.

We used a solution of 0.4% Fairy (S402) in de-ionised water throughout the thesis in order to make sure that the solution was well above the CMC and to allow comparison between various experiments. Table 1.1 summarises the ingredients of Fairy.

The presence of surfactants generally does not change the physical properties of the bulk liquid. They have a major influence, however, on the dynamic properties of

Common name of chemical	Type	CAS	Concent.
Alcohols, C9-11, Ethoxylated	non-ionic	68439–46–3	1–5 %
Ethanol	non-ionic	64–17–5	1–5 %
Amies, C10-16-Alkyldimethyl, N-Oxides	cationic	70592–80–2	5–10 %
S.O.Alkyl Ethoxsulph.Fat.Alc.(AE0.6)	?	reacted ingred.	20–30 %

Table 1.1: Chemical ingredients of Fairy dish-washing liquid.

the interfaces. The surfactants contained in Fairy (listed in table 1.1) form a very rigid mesh of molecules at the gas/liquid interface, making it very immobile (small mobility parameter M). This is reinforced by polymers attached to some of the head groups ("ethoxylated"). Earlier experiments on foam drainage have confirmed this [125].

In some cases we use SDS (sodium dodecyl sulfate), which is the most commonly used pure surfactant. It produces very mobile interfaces, which can therefore be contrasted with the Fairy experiments (see Chapter 5). Care needs to be taken, however, as SDS oxidises into dodecanol, which generates very rigid interfaces.

Part I

Structure
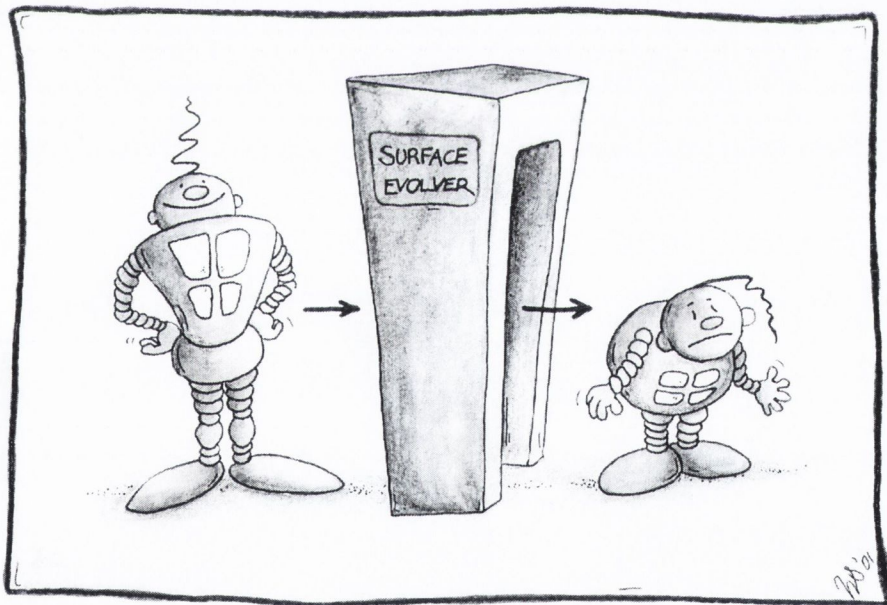
Chapter 2

Conformal maps with 2D foams

2.1 Introduction

In this chapter we present a very simple, but strikingly beautiful experiment giving new insights into the structural properties of two-dimensional (2D) foams. For this purpose we generate monodisperse, two-dimensional foams by trapping a layer of equal-volume bubbles between two glass surfaces. The application of appropriately angled or curved surfaces imposes a specific variation of the apparent bubble area in the foam. We show that upon minimising their interfacial energy within these constraints, the bubbles order in such a way as to reproduce conformal maps of the hexagonal honeycomb lattice. The *honeycomb* is the structure which minimises the line length (or energy) of a 2D foam with cells of equal area [55] (Fig. 2.1).

Conformal mapping finds uses in many areas of physics where 2D fields or patterns are found. Such a mapping can be constructed using any analytic function $w = f(z)$, according to

$$u + iv = f(x + iy)$$

where $z = x + iy$ and $w = u + iv$ [87]. The application of conformal maps is perhaps most familiar in the context of 2D incompressible fluid mechanics [96], where they are used to produce equivalent problems with simpler boundary conditions.

Certain patterns that occur naturally are immediately recognisable as conformal transformations of simpler ones. Popular examples include cellular growth patterns in biology [130], structures formed by magnetised steel balls in external force fields

(a)   (b)   (c)
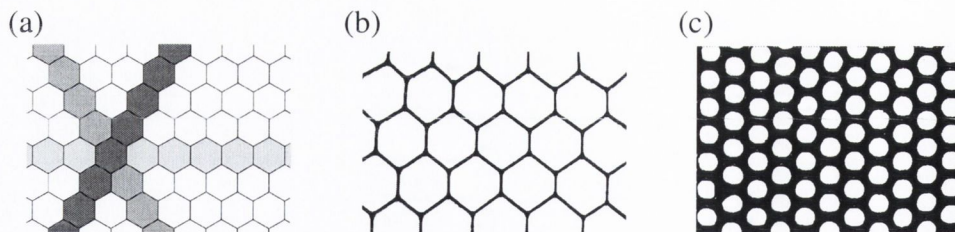
Figure 2.1: Examples of the *honeycomb* structure, which is the 2D monodisperse foam with minimum energy, used as initial pattern for the conformal transformations. (a) Computater generated honeycomb. The shading will be retained throughout this chapter to visualise the effect of the transformations. b) Experimentally obtained dry and c) wet 2D monodisperse foams sandwiched between two parallel glass plates.

[103, 102], ferrofluid foams in magnetic fields [44] or crystal growth in amorphous films [74].

One of the principal properties of conformal transformations is *isogonality*: any two curves that intersect are transformed into curves that intersect at the same angle. Isogonality upon transformation preserves a very important property of any 2D foam at equilibrium: in order to balance surface tension, edges have to meet three-fold at $120°$ (see §1.2.2). Another property is only preserved by the special class of *bilinear* conformal maps: that all edges have to be arcs of circles whose curvatures add to give zero at every vertex (see §2.2.2). Together these conditions guarantee that the new structure obeys the rules of equilibrium. For the general case, the theoretically mapped patterns will only be approximations of the experimentally observed equilibrium structures.

In the following sections we review some properties of conformal maps before showing how certain examples can be realised with our simple setup.

2.2 Conformal maps, inversion and soap froth

Locally, a conformal mapping $f(z)$ preserves angles (the isogonal property) but not areas (see Fig. 2.2). If $ds_z = (dx^2 + dy^2)^{\frac{1}{2}}$ is a small element of line in the (x, y) plane, it will be magnified according to

$$ds_w = \left| \frac{dw}{dz} \right| ds_z = |f'(z)| \, ds_z \tag{2.1}$$
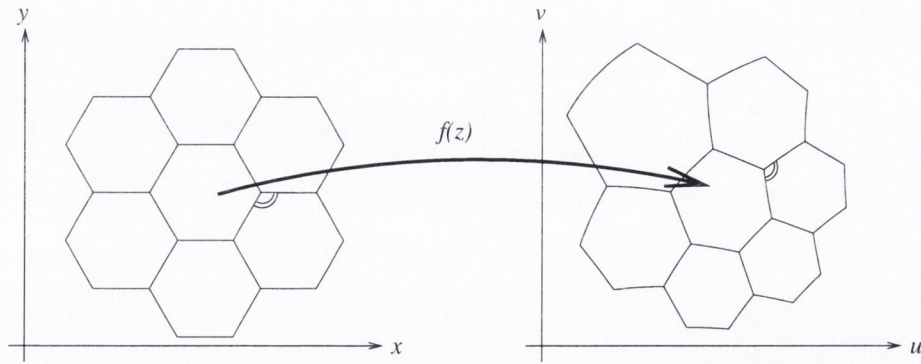
Figure 2.2: A conformal mapping of a hexagonal "bubble" preserves the angles at vertices, but not the area of each bubble. Only *bilinear* maps transform arcs of circles into arcs of circles.

upon transformation. Hence a small element of area will be scaled by a factor of $|f'(z)|^2$. We will concentrate on two types of maps of the hexagonal lattice, which are characterised by their symmetry properties, and which are of particular relevance to many areas of science:

1. Conformal transformations with translational symmetry (§2.2.1)

2. Conformal transformations with rotational symmetry (§2.2.2).

The numerical mapping has been carried out by Simon Cox. For a more detailed description of his procedure refer to [38].

2.2.1 Conformal transformations with translational symmetry

It can be shown that the *logarithmic* map is the *only* conformal transformation with translational symmetry [103]. It is

$$w = f(z) = u(z) + iv(z) = (i\alpha)^{-1}\text{Log}\,(\alpha z)\,, \tag{2.2}$$

which maps the interior of a circle of radius $1/\alpha$ onto the upper half plane. For an example of the effect of this upon the honeycomb structure see Fig. 2.3 b). This elegant pattern has been dubbed *Gravity's Rainbow*. In our case it has translation period $\pi/3\alpha$ rather than $2\pi/\alpha$ because of the 6-fold symmetry of the honeycomb pattern.

Application of Equ. (2.1) reveals that the area A of the transformed hexagons depends only on v:

(a)

(b)

(c)
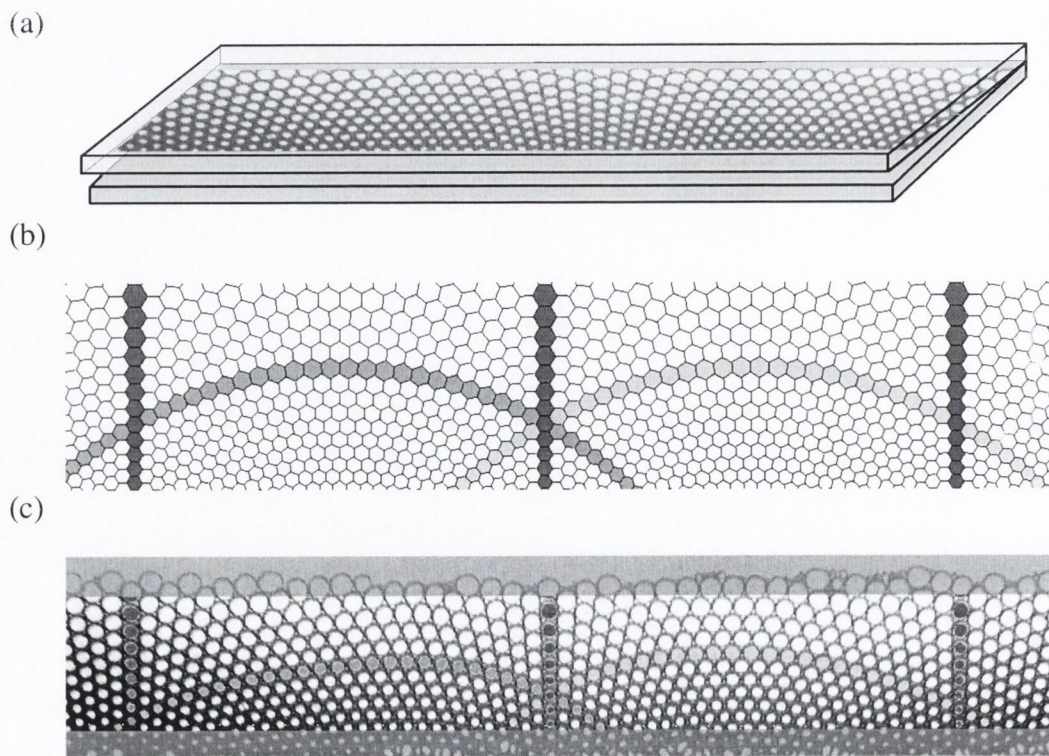
Figure 2.3: The logarithmic map (*Gravity's Rainbow*). a) Experimental setup: A mono-layer of bubbles is trapped between two inclined glass pates. The bottom plate is horizontal. b) Numerical mapping of a perfect honeycomb using Equ. (2.2). c) Experimentally obtained pattern. The shading shows how lines of neighbouring cells that were initially straight (compare Fig. 2.1) are transformed.

$$A(w) = A(v) \sim e^{2\alpha v}. \tag{2.3}$$

2.2.2   Conformal transformations with radial symmetry

Any conformal map of radial symmetry has to satisfy the differential equation [103]

$$w^{-\delta} \, dw = \beta \, dz, \tag{2.4}$$

where δ is a real and β a complex number. Equ. (2.4) has two different solutions depending on the value of δ.

For $\delta = 1$ we obtain the map

$$w = f(z) = w_0 \, e^{\beta z}, \tag{2.5}$$

which is commonly referred to as *phyllotaxis* [64] and found in many systems governed by cellular growth. Popular examples are the florets of a sunflower (Fig. 2.4 b)) or the

(a) (b) (c)
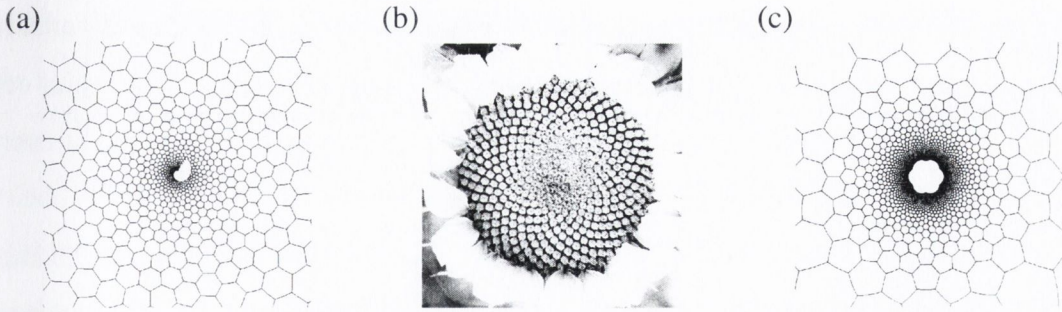
Figure 2.4: Two special cases of maps with radial symmetry. (a) Numerical example of phyllotaxis using Equ. (2.5). (b) Phyllotactic design shown by a sunflower (photograph taken by Yves Couder). (c) Numerical example of the inversion defined by Equ. (2.8) with $\delta = 2$.

scales of a pineapple [5]. The latter type of cylindrical phyllotaxis can be beautifully reproduced using the regular stacking of soap bubbles in cylindrical tubes [127], which we introduce in Part III (Fig. 6.2).

The case $\delta \neq 1$ is more general and we will refer to it as the *circle map*:

$$w = f(z) = w_0 \ z^{\frac{1}{1-\delta}}. \tag{2.6}$$

The area A of the transformed hexagons varies with distance r from the centre as:

$$A(w) = A(r) \sim r^{2\delta}. \tag{2.7}$$

The circle map also contains the important special case of *inversion* for $\delta = 2$ (see Fig. 2.4 c)):

$$f(z) = z^{-1}, \tag{2.8}$$

or more generally the bilinear or *homographic* transformation generated by

$$f(z) = (az + b)/(cz + d),$$

where a, b, c and d are real numbers. This combines the inversion with an arbitrary translation and rotation, which are of no significance in the present context. This case has additional special properties that are of particular relevance to 2D soap froths, as noted by Weaire [123]. Under inversion, arcs of circles remain circular upon transformation. They conform to a further property which may be obliquely stated as follows: any 2D soap froth structure in static equilibrium transforms into another equilibrium

structure. This requires rather more than the preservation of $120°$ angles at vertices. The existence of a unique gas pressure in each cell requires that the curvatures of cell edges (related to pressure differences by the Laplace Law) add to give zero at every vertex. This zero sum rule is preserved upon inversion [123].

Only an inversion has this *exact* property of preserving equilibrium for the 2D soap froth while changing the area of its constituent bubbles. However, a general conformal transformation can achieve a *good approximation* to this property. To see this, note that any $f(z)$ can be approximated by an inversion (or homographic transformation) in the neighbourhood of a point z_0, in the sense that terms in its Taylor expansion in $(z - z_0)$ are identical up to second order. This is a sufficient condition to allow us to assume that the conformal transformation has similar effects on local curvatures to those of the bilinear transformation which approximates it. But in general this holds only in lowest order, so the sum rule holds at every vertex, but the curvature varies along each edge.

Such arguments can be adduced to transform *any* equilibrium soap froth structure.

2.3   Experimental procedure and simulation

Bubbles of equal volume are generated by blowing nitrogen at constant pressure through a nozzle into a surfactant solution (we use tap water and Fairy Liquid). Glycerol is added to the solution to prolong the lifetime of the foam. The bubbles are then trapped between two glass surfaces, of which the bottom one is flat and horizontal. A variation of the apparent 2D bubble area with position within the pattern is imposed by using a curved upper surface. If the separation between the surfaces is $d(w)$, then the bubble areas vary as $A(w) \sim d(w)^{-1}$. The precise shapes of surfaces required by theory are difficult to manufacture. We find, however, that astonishingly good results can be obtained by using small bubbles and much simpler surfaces, which can be considered as approximations of the required ones (see next section for details). The number of available geometries is plentiful: inclined plates or cylinders for the map with translational symmetry, spheres of different radii and funnels of different shapes for maps with radial symmetry. We will concentrate on a small selection.

Even if the theoretically suggested mappings of the previous section produce the

ideal, energy-minimizing foam structures (and we make no claim to prove this), they do not occur spontaneously in this procedure. A many-bubble foam has a vast energy landscape of meta-stable states, which need to be overcome by an annealing-like experimental procedure. This involves keeping the foam very wet and varying the spacing and angles between the surfaces repeatedly. After a while, the perfect pattern begins to emerge and one can concentrate on eliminating isolated defects, which glide beautifully along the arches of the pattern.

2.4 Conformal 2D foam with translational symmetry

To obtain the Gravity's Rainbow defined in §2.2.1, we should introduce an upper plate which decreases exponentially in height in one direction, $d(w) \sim e^{-2\alpha v}$. However, we obtain an excellent approximation to this map with a linear decrease, corresponding to a tilt of the upper, flat plate. The setup is shown in Fig. 2.3 a). A large bubble cluster is produced in order to reduce any quantising influence of the boundaries of the specimen on the periodic pattern – the boundaries are so far away that they have only a negligible influence on the choice of period. Using a large cylinder instead of the slanted upper plate works equally well. Fig. 2.3 c) shows an experimental result obtained by projecting the foam with an ordinary overhead projector.

The similarity between the experimental image and the conformally mapped pattern (Fig. 2.3 b)) is striking. Apart from a few defects, we obtain the well-known pattern of interwoven rainbows, whose periodicity is determined by the bubble volume and angle between the plates.

However, the conformally mapped honeycomb is neither a true equilibrium foam structure, nor does the variation of bubble area in the experiment obey precisely that demanded from the conformal theory. We attempt to bridge the gap between the conformal and experimental pattern by considering the effect of relaxation on a true equilibrium structure. This may be accomplished using any of a number of published procedures [4, 12]. We used the Surface Evolver [16, 38] to produce the relaxed structures shown in Fig. 2.5. We began with the equilibrated free cluster of 400 equal-area bubbles shown in Fig. 2.5 a), imposed a variation of bubble area with vertical coordinate

(a)

(d)

(b)

(c)
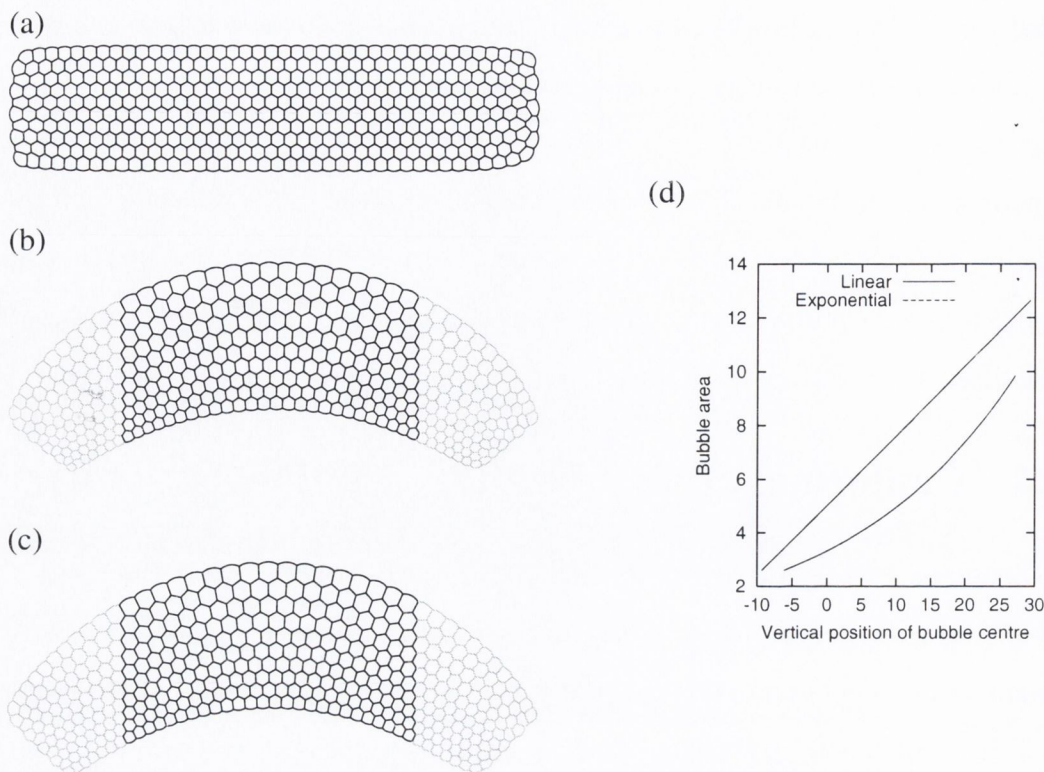
Figure 2.5: The effect of relaxation on 2D foam structures, simulated by Simon Cox [38] using the Surface Evolver [16]. (a) The initial rectangular configuration of 400 bubbles with equal areas (honeycomb). (b) The equilibrium structure for a linear increase in bubble area, and (c) for an exponential increase. The two are difficult to distinguish, even over a range of values of $A(y)$. Hence the logarithmic map is well-approximated by a linear increase in the height of the experimental sample. (d) The imposed variation of area A with vertical position y for linear and exponential growth.

y, and re-equilibrated the structure. The rectangular cluster bends to accommodate the change in cell areas, which is shown for linear and exponential $A(y)$ in Fig. 2.5 b) and c) respectively. This procedure introduces no topological defects in either case, at least for a wide range of parameters in the function $A(y)$. Indeed, the two cases are almost indistinguishable, explaining why the linear increase in the height of the experimental system is such a good approximation of the logarithmic map. The outline of the computed sample is rather arbitrary since it is essentially the transform of the outline of the corresponding arbitrary boundary of the original monodisperse sample.

2.5 Conformal 2D foam with rotational symmetry

In order to generate a circle map we would need a variation of the spacing according to $d(w) = d(r) \sim r^{-2\delta}$. The case $\delta = -1$ can be approximately realised by using a large spherical vessel or watch glass for the upper plate, as illustrated in Fig. 2.6 a). An experimental result can be seen in Fig. 2.6 c). Fig. 2.6 b) shows the corresponding conformal pattern.

We do not recover the predicted 12-fold symmetry in the experiment, but obtain an almost perfect 9-fold symmetry with a few defects, whose origins will be discussed in the next section. Analysis of Fig. 2.6 c) shows that the 2D bubble area decreases almost linearly with distance from the centre (rather than with r^{-2}, as predicted by Equ. (2.7)). This is more consistent with the case $\delta = -1/2$ and 9-fold symmetry. Such discrepancies maybe due to the effects of wetness and the 3D curvature of the films, as described in section §2.6.

To generate cases with $\delta > 0$ we stretch an elastic membrane across the end of a short cylinder and attach a piece of string to its centre, which is pulled to produce a "funnel" shape. For an experimental result refer to Fig. 2.6 e). Comparison between theoretical prediction and experiment is more difficult here, as the patterns exhibit less symmetry and the precise shape of the funnel is not known. Nevertheless, the similarities between the pattern is obvious, with almost perfect sections being separated by lines of defects.

All the circle experiments are conducted on a glass table, as we find that the best images can be obtained with transmitted light from a diffuse source.

2.6 Complications and discussion

In addition to the discrepancies entailed by the approximate representation of analytic functions, a further difficulty arises if the separation increases too steeply. At a certain critical separation, bubbles with less than six sides detach from one of the surfaces to create a three-dimensional structure [25]. For the hexagonal lattice this initially affects only the bubbles on the boundary of the cluster, but the instability then propagates
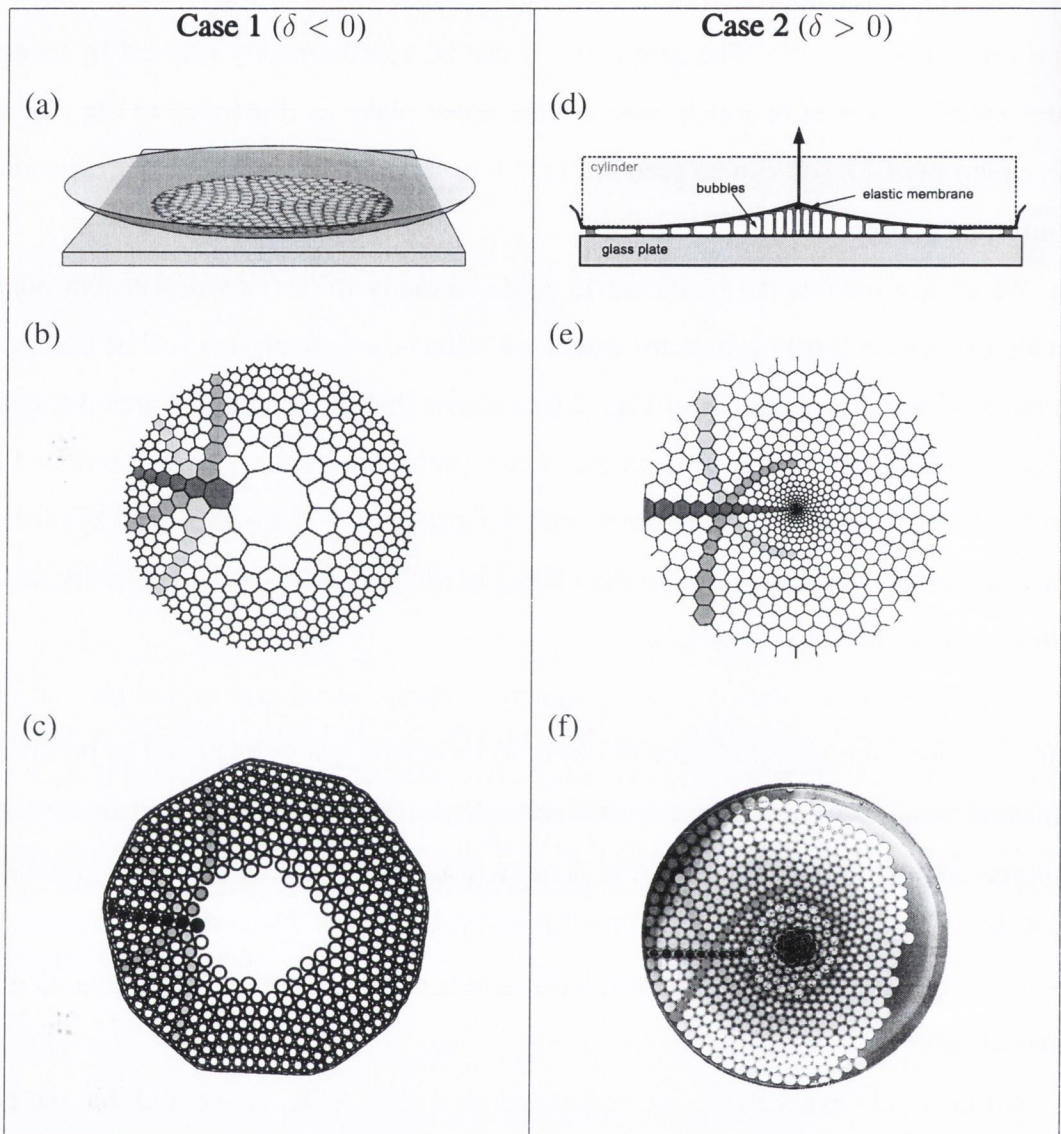
Figure 2.6: Examples for the two general cases of the circle map defined by Equ. (2.6). **Case 1**: Decrease of bubble area with distance from centre ($\delta < 0$). This can be realised experimentally by using convex vessels for the upper surface. a) A spherical vessel or watchglass can be used for an upper surface to approximate the case $\delta = -1$, for which b) shows the numerical prediction, and c) an experimental result. **Case 2**: Increase of bubble area with distance from centre ($\delta > 0$), obtained between funnel-like surfaces and a glass plate. d) Setup: A funnel shaped surface is produced by shapes by pulling the centre of a membrane which is stretched over a cylinder. e) Numerical example for $\delta = 2/3$. f) Experimental result. (The shading shows how lines of neighbouring cells that were initially straight (compare Fig. 2.1) are transformed.)

inwards to destroy the pattern.

On some occasions we have found topological defects in more or less ordered arrangements. The precise role of these defects, which might be to compensate for the approximate representation mentioned above, has not been clarified. Note that with topological arguments one can prove that any finite bubble cluster must contain at least 6 defects [99]. But this theorem can be accommodated by defects at the edge.

2.7 Conclusions and Outlook

Two-dimensional foams offer a system for very beautiful and easily accessible experiments, which improve our understanding of foams and physically related systems. In particular, we have shown that various conformal patters may be demonstrated. Other illuminating experiments with this simple "foam sandwich" include

- Coarsening, topological changes and statistics [53, 26]

- The structure of the beehive [129]

- Foam motion in various channels and networks [39]

Brakke [15] has applied inversion in 3D (which has similar properties to the 2D case), to create 3D bubble clusters, which serve to test mathematical conjectures. In the 3D case, inversion provides a mapping between equilibrium structures only in a very limited number of cases, where surfaces are spherical.

Our technique may also be useful for the investigation of more complex patterns using more complicated surfaces or polydisperse foams. Questions also remain concerning the precise distribution and role of defects, which we sometimes find to have a periodic arrangement.

Very recent theoretical work by Mancini and Oguey [80], in which they built on our suggestion of considering the curvature in the third dimension [38], has added another perspective. As a result of the curvature of the confining surfaces and the condition that films must meet these vertically, the films have a curvature in the third dimension, which has been neglected in our 2D calculations. If this additional curvature is taken

into account, the 2D pattern generated by the films touching the surface do not have to be arcs of circles any more as a result of the 3D Laplace law (Equ. (1.1)). There is some interesting physics involved in these "2D surface foams" considered by Mancini and Oguey [80]. It remains to be seen whether our foam patterns might actually be perfect conformal transformations of the honeycomb, rather than approximations, under consideration of the influence of the third dimension.

Part II

Drainage
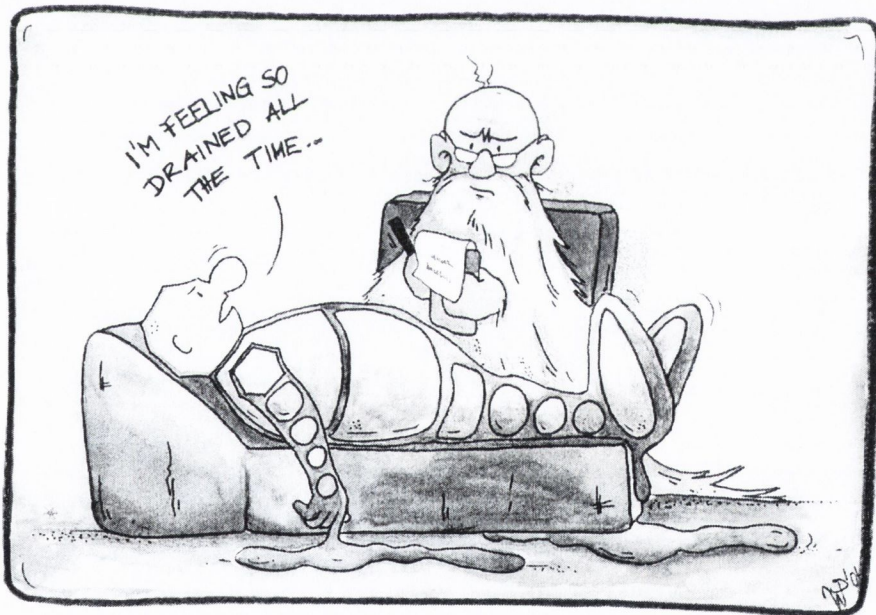
Chapter 3

Introduction to Part II

In this part we discuss the microscopic properties of foam drainage (refer to §1.3.1) by focusing on a simple system consisting of two extended surface Plateau borders (Fig. 1.4 b) in §1.2.1) connected by a thin film. Unlike interior Plateau borders (Fig. 1.4 a) in §1.2.1), these are formed where a film is attached to a surface. In our system they are generated by injecting surfactant solution at a constant rate between two narrowly spaced, vertical glass plates. The setup is shown in Fig. 4.1, cross-sections of this system for various flow rates in Fig. 4.2. Whenever we refer to the whole unit, rather than the individual Plateau borders, we call it *rivulet*. Chapter 4 focuses on the flow of liquid in the Plateau borders at a broad range of flow rates, whilst Chapter 5 investigates the flow in the connecting film.

The cross-sectional area A_{PB} of the Plateau borders depends on the flow rate applied at the top of the plates. A theoretical description of this dependence is given in §4.2.1. The point where the thin film and the Plateau border are joined, labeled S (Fig. 1.4), is of special interest here.

Upon varying the flow rate in this simple system, we study a variety of elucidating phenomena which can be grouped into four main categories:

1. The variation of the Plateau border cross-section with flow rate offers insights into the mobility of the gas/liquid interface and the flow condition at the point S. In §4.2.2.1 we show that surfactants known to make very rigid interfaces become increasingly mobile under the shear stress of high liquid flow velocities.

Furthermore we provide arguments which show that the traditionally assumed zero flow velocity at the Plateau border corner S only holds for low flow rates.

2. For large flow rates and small plate separations, the two Plateau borders swell enough to merge. Upon this merging an unexpected effect is observed: the Plateau border width remains constant over a large range of flow rates. We relate this to a change in the flow boundary conditions, which ties in well with conclusions drawn from point 1. Further supporting arguments are given in Chapter 5.

3. At a critical flow rate the entire rivulet becomes unstable, displaying beautifully regular wave patterns, which range from upward-travelling, sinusoidal forms to downward-travelling serpentine waves. We have identified four different regimes [40], which are elaborated in §4.3. The detailed physical mechanism of this instability is not yet understood. We present some theoretical key ideas, which seem to identify some important key ingredients.

4. A general assumption made in foam drainage relates to the observation that the liquid in the films moves opposite to that in the Plateau borders. By using the same system as above but focusing on the flow in the film instead, we show that this assumption is only valid for low flow rates (Chapter 5).

Unlike in most studies conducted up to date we investigate a very broad range of flow rates and focus on high flow rates in particular. These provide us with a plethora of puzzling observations, most of which await explanation. Even though it is rather unlikely that flow rates of these magnitudes will ever be encountered foams, we hope that by going to these extremes we will be able to take a different and elucidating angle at the fluid dynamics of foams, and in particular its instabilities.

Chapter 4

Drainage and stability of individual surface Plateau borders

4.1 Experimental setup and procedure

The experimental arrangement is shown in Fig. 4.1, incorporating an image of a meandering rivulet. Surfactant solution (0.4 % Fairy dishwashing solution, see §1.4) was injected with a glass nozzle at various constant flow rates at the top of two narrowly spaced, vertical glass plates of variable separation D. For all flow rates investigated the flow equilibrated within the 10 cm below the injection point. We confirmed this by measuring the variation of the rivulet width with distance from the inlet. All measurements were taken well outside this entry length to ensure equilibrium conditions.

Fig. 4.2 shows the three distinct regimes of rivulet cross-sections obtained for various flow rates and plate separations. Regime I is obtained for low flow rates and/or large plate separations, regime III for large flow rates and/or small plate separations.

The boundaries of each Plateau border's cross-section can be approximated by two circular arcs of radius r_{PB} and the flat surface of the glass plate, as shown in Fig. 4.2. Since the system is nearly perfectly wetting[1], the width W of the Plateau border, and hence the rivulet, equals twice the radius of curvature r_{PB} of the Plateau border.

The glass plates were 1.5 m high in order to reduce the influence of boundary effects. Their spacing was adjusted using shims (thin metal sheets of high precision) of various thicknesses. Before every experiment, the glass plates were carefully cleaned

---

[1] This means that the contact angle of surfactant solution on glass is close to zero.
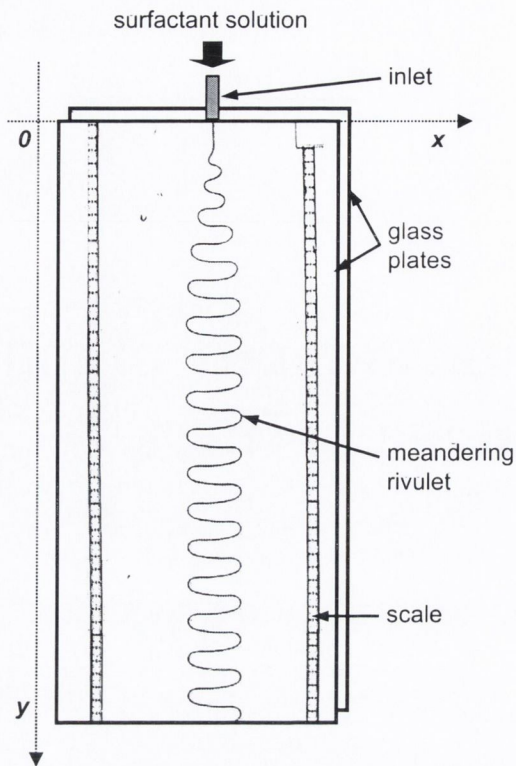
Figure 4.1: Sketch of the experimental setup. Surfactant solution is injected at various flow rates between two narrowly spaced vertical glass plates. Illustrated here is a photograph of a meandering rivulet, which is observed for high flow rates. For low flow rates, the rivulet is straight and vertical.
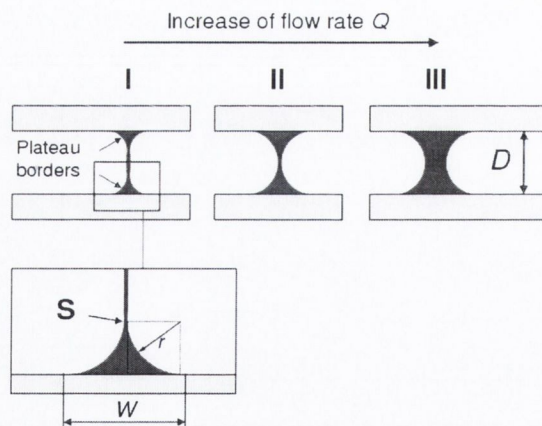
Figure 4.2: The various cross sections of the rivulet for different flow rates marking the three distinct flow regimes: (I) A thin film is attached to the plates by Plateau borders. Flow through the film can be neglected. The close-up shows the cross-section of one Plateau border, marking the point S, where film and Plateau border are connected. (II) The two Plateau borders touch. (III) The Plateau borders are merged and form a liquid bridge.
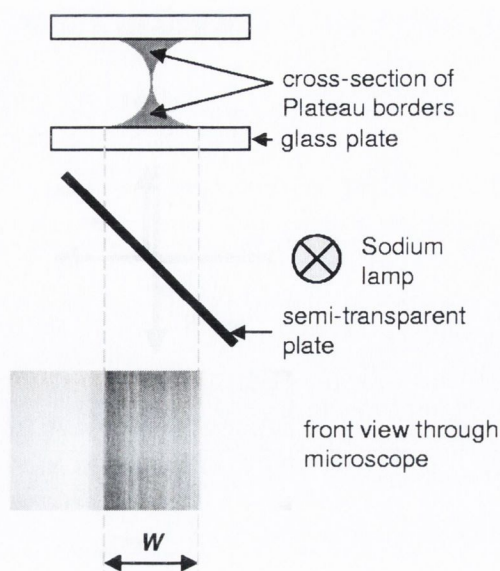
Figure 4.3: Experimental setup to measure the rivulet width W: A Sodium lamp is used in combination with a semi-transparent plate to produce a monochromatic light reflection of the rivulet. Due to the curved nature of the gas/liquid interface, the rivulet appears as a well defined shadow through the microscope.

and wiped dry with a soft cloth. Most of the observed phenomena, however, did not seem to display a significant dependence on the cleanliness of the plates.

Variable flow rates were obtained and monitored using a flow meter with a high precision needle valve. A large tank containing the solution provided constant pressure. Images were taken with a digital camera and subsequently analysed using the software tool ImageJ [61]. For high precision measurements images were taken through a microscope.

Precise measurements of the Plateau border width W pose an experimental challenge due to the curved nature of the liquid/gas interfaces and the vanishing contact angle of the surfactant solution with the glass plate. After comparing various techniques, we found that the best results were obtained by using the reflection of monochromatic light generated by a Sodium lamp (Fig. 4.3). In this set-up a clearly distinguishable shade is produced where the gas-liquid interface curves away from the plane of the glass plates.

4.2 Low flow rates - the straight rivulet

4.2.1 The fluid dynamics of surface Plateau borders

This section establishes the theoretical frame work and assumptions necessary for the quantitative description of the fluid dynamics of vertical surface Plateau borders, corresponding to the geometry present in regime I (Fig. 4.2).

As a result of the constant flow rate, the system assumes a steady state. Hence, the conservation law is given by

$$Q = A_{PB}(y)U(y) = \text{const}, \tag{4.1}$$

where Q is the flow rate and U the average flow velocity in a Plateau border of cross-section A_{PB}. y is the vertical and x the horizontal, in-plane coordinate (see Fig. 4.1).

In equilibrium, the dissipation has to be balanced by gravity (ρg) and the pressure gradient along the Plateau border ($-\partial p_l/\partial y$). ρ is the liquid density, g the gravitational acceleration and p_l the liquid pressure. For a vertical Plateau border this gives:

$$\rho g - \frac{\partial p_l}{\partial y} - \frac{\eta_l f U}{A_{PB}} = 0. \tag{4.2}$$

The dissipative term is well know from fluid flow in pipes [118]. η_l is the viscosity of the liquid. The dimensionless factor f depends on the geometry of the Plateau border and the flow boundary conditions at the liquid/gas and liquid/solid interface. It is generally determined by computer simulations and reappears at various stages in this Part. This is a result of its strong link with the much discussed *surface shear viscosity* η_s of the gas/liquid interface (refer to §1.4) and the mobility M of the Plateau border (Equ. (1.4) in §1.4) [73, 42, 88, 114, 108].

Since the liquid is driven by gravity, we consider the second term in Equ. (4.2) to be zero. We therefore know that for the straight, equilibrated rivulet A_{PB} and U are independent of y and

$$A_{PB} = \frac{\eta_l f}{\rho g} U. \tag{4.3}$$

Using Equ. (4.1) we find

$$A_{PB} = \left(\frac{f \eta_l}{2\rho g}\right)^{\frac{1}{2}} Q^{\frac{1}{2}}. \tag{4.4}$$

Keeping in mind that our system consists of two surface Plateau borders, and neglecting the very small amount of liquid flowing in the film, we obtain for the Plateau border width W

$$
\begin{aligned}
W = 2r_{PB} &= 2 \left(2 - \frac{\pi}{2}\right)^{-\frac{1}{2}} A_{PB}^{\frac{1}{2}} \\
&= \left(2 - \frac{\pi}{2}\right)^{-\frac{1}{2}} \left(\frac{8f\eta_l}{\rho g}\right)^{\frac{1}{4}} Q^{\frac{1}{4}} \\
&= G(f, \rho, g, \eta_l) \; Q^{\frac{1}{4}}.
\end{aligned}
\tag{4.5}
$$

We see from Equ. (4.5) that the width W of a (surface) Plateau border is predicted to vary as $Q^{\frac{1}{4}}$. This is a result of the self-similarity of the Plateau border cross-section for various flow-rates and hence a general scaling argument, which holds for any geometry. For this reason, the exponent is independent of any physical parameters of the liquid and the interface. These only influence the pre-factor $G(f, \rho, g, \eta_l)$. By leaving η_l, ρ and g unchanged in an experiment, we can therefore determine f by measuring the variation of W with flow rate Q. Hence, with this fairly simple experiment we were able to study implicitly the flow boundary conditions in a Plateau border (see §4.2.2.1).

Of similar importance to the mobility parameter M is the flow condition at the Plateau border corner S (refer to Fig. 4.2). Traditionally, the flow velocity has been assumed to be zero at this point, which is based on findings of Jashnani and Lemlich [63]. They report that the flow direction in the film is opposite to that in the Plateau borders, concluding that there must be a point of zero flow velocity between Plateau border and film. For low flow rates, this assumption has been indisputably established by Koehler et al. [73] in recent experiments.

For higher flow rates and long Plateau borders, however, we show that this assumption does not hold any more. At a critical flow rate, which depends on the surfactants used and the geometry of the film, the flow direction of the film is reversed from upward to downward as it is dragged along with the flow in the Plateau borders. For more detailed arguments see §4.2.2.1 and Chapter 5.
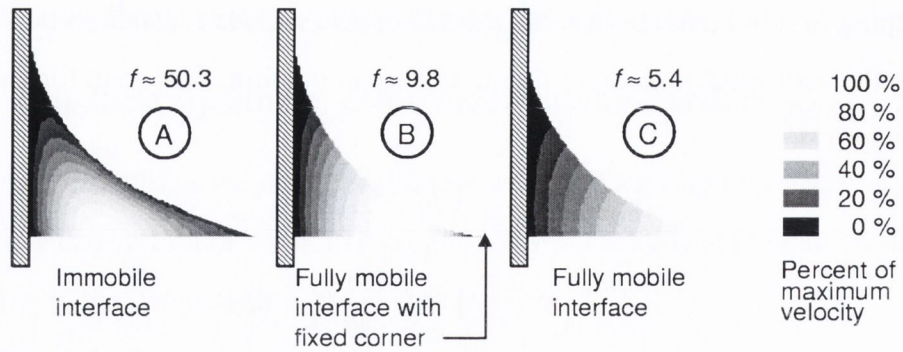
Figure 4.4: Velocity profiles and corresponding values for f obtained by numerically solving the Navier-Stokes Equ. for three sets of boundary conditions: (A) No-slip at all the boundaries; (B) no-slip at the wall and the Plateau border corner S (see 4.2), and full slip at the gas/liquid interface; (C) no-slip at the wall and full slip everywhere else. (Simulations by S. Cox)

Fig. 4.4 shows numerically predicted flow profiles and the corresponding values for f obtained by solving the Navier-Stokes equation for a vertical surface Plateau border for three different sets of boundary conditions (simulations by S. Cox). Due to symmetry reasons it is sufficient to consider only one half of a Plateau border. The three cases are chosen such that they represent limits, which we compare with our experimental findings.

Case A considers fully rigid interfaces ($f = 50.3$). Case B implements no-slip at the wall and the Plateau border corner S, and full slip at the interfaces ($f = 9.8$). This value depends on the width of the film and should at this stage only be taken as an approximation. In case C the interfaces and the corner point are fully mobile; the drag force is only asserted by the no-slip condition at the wall ($f = 5.4$).

By combining Equ. (4.1) and (4.3) we find for the average flow velocity in the Plateau borders

$$U = \left(\frac{\rho g}{2f\eta_l}\right)^{\frac{1}{2}} Q^{\frac{1}{2}}. \tag{4.6}$$

The maximum flow rate Q applied in the experiments reported in this thesis was 250 mm^{3}s^{-1}. Using the smallest possible $f = 5.4$ from the simulations gives us a maximum average velocity of $U \approx 0.5$ ms^{-1}. Using the typical Plateau border radius $r_{PB} \approx 0.5$ mm for the length scale l, we can calculate the Reynolds number $Re = \rho U l \eta_l^{-1} \approx 250$. Since this is well in the laminar regime, we do not expect effects
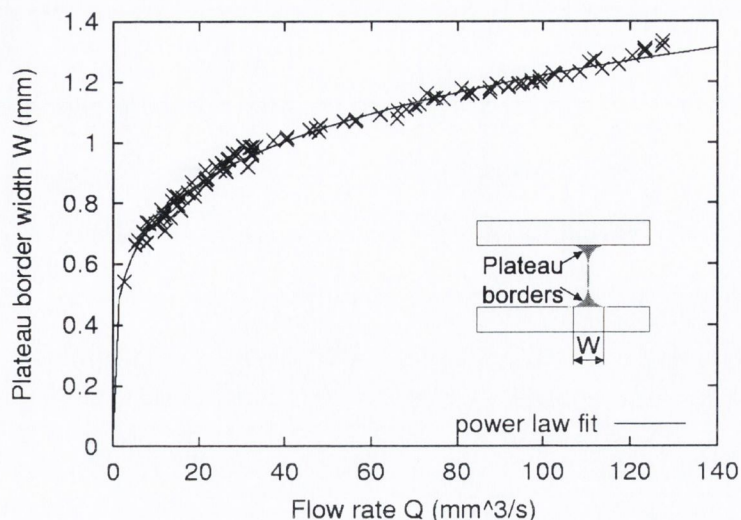
Figure 4.5: Variation of Plateau border width W with flow rate for a plate separation of $D = 2$ mm. The data is fitted to a power law, conforming well to Equ. (4.5).

of turbulence in our system.

4.2.2 Experimental results and analysis

4.2.2.1 Separate Plateau borders – regime I

Fig. 4.5 shows a typical set of data for the variation of the Plateau border width W with flow rate Q for a plate separation of $D = 2$ mm. Fitting it to Equ. (4.5) shows that the power law is indeed reasonably well obeyed with an exponent of (0.22 ± 0.01) (ms)$^{-1/4}$. We find that the deviation from the expected $1/4$ is systematically related to the range of flow rates investigated, being much smaller for low flow rates.

We obtain typical pre-factors in the range

$$6.93 \ 10^{-2} \ (\text{ms})^{1/4} \ < \ G(f, \rho, g, \eta_l) \ < \ 7.16 \ 10^{-2} \ (\text{ms})^{1/4} \ (\text{see Equ. (4.5))},$$

which gives $5.2 < f < 7.2$. The smaller prefactors are obtained for higher flow rates. Comparison of these values with those predicted by our numerical calculations (refer to Fig. 4.4) imply that we are dealing with highly mobile interfaces and Pleateau border corner "S". From earlier work [128], on the contrary , we know that Fairy produces very rigid interfaces of $f \approx 50$.

Part of this deviation could be due to the possibility that we may only measure a certain fraction of the actual Plateau border width due to the zero wetting angle. We

$Q = 20$ mm^3 s^{-1} $Q = 25$ mm^3 s^{-1} $Q = 28$ mm^3 s^{-1}
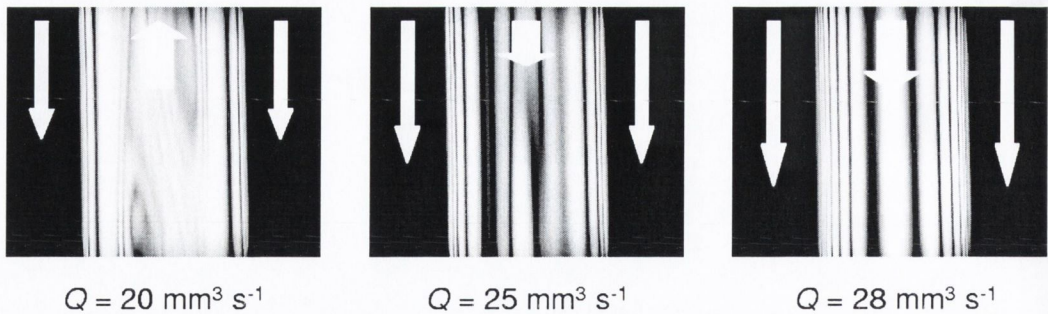
Figure 4.6: Interference pattern generated by the thickness variation of the film (see Chapter 5) show that for low flow rates ($Q = 20$ mm^{3}s^{-1}) the film between the Plateau borders (black stripes) moves upwards in a turbulent fashion. At a critical flow rate (here $Q \approx 25$ mm^{3}s^{-1}) the flow reverses direction and becomes increasingly laminar. At high flow rates it is being dragged along with the flow in the Plateau borders in a totally laminar fashion. ($D = 2$ mm in this example.)

confidently approximate this systematic error to be smaller than 10%. Using linear error propagation, this leads to an error of 40% in f, hence $f_{min} = 5.2 \pm 2.1$ and $f_{max} = 7.2 \pm 2.9$. This error seems large, but is still well outside the originally expected $f \approx 50$. Hence, the deviation must have a physical origin. The most obvious condition to question is that of the rigid interfaces and corner point "S".

By observing and probing the flow of the film, which connects the two Plateau borders, we could indeed show that for elongated Plateau borders connected by narrow films there exists a flow rate at which the movement of the film reverses from upward to downward. This effect is shown in Fig. 4.6. It results in the Plateau border corners being released as the flow rate is increased, which leads to a higher average velocity and smaller Plateau border width for a given flow rate. For an extensive analysis and description of this particular experiment refer to Chapter 5.

Changes in the boundary condition at the point S do not only influence the pre-factor, but also the exponent of Equ. (4.5). An increasing mobility of the Plateau border corner leads to a smaller exponent as we go to higher Q; which is what we observe in the experiment.

We have not quantitatively determined the critical flow rate at which the film flow reverses as a function of plate separation. We can state qualitatively from observations that it occurs earlier for smaller plate separations - and hence narrower films. Further-

more, it occurs for flow rates at the very bottom of the range of flow rates considered in our experiments and is therefore expected to have a significant influence on the flow properties of the overall system.

Nguyen [88] has provided a numerically predicted relationship between the average flow velocity and the mobility parameter M of an interior Plateau border with fixed corners. This can be related to our f as follows:

$$f = \left(\frac{aM^{\frac{1}{2}}}{b + M^{-m}} + 0.020 \right)^{-1}, \tag{4.7}$$

where $a = 0.0655$, $b = 0.209$ and $m = 0.628$. Surface Plateau borders are quite different to interior Plateau borders. But we can employ Equ. (4.7) to obtain an approximation of the *order of magnitude* of M and η_s for our system. For $5.2 < f < 7.2$ we obtain $3.3 > M > 2.2$, which (using a Plateau border radius of $r_{PB} = 0.5$ mm) leads to 1.5×10^{-7} kg s^{-1} $< \eta_s < 2.3 \times 10^{-7}$ kg s^{-1}.

These values compare well with what Saint-Jalmes et al. [108] obtain experimentally for surfactant systems combining SDS and dodecanol, which are known to have similar interface properties as Fairy. They find $0.5 < M < 1.5$, but work at much smaller flow rates and hence with much thinner Plateau borders, which give smaller mobility parameters (refer to Equ. (1.4)).

4.2.2.2   Merging Plateau borders - a reluctance to coalesce?

In the previous section we investigated the behaviour of two separate Plateau borders connected by a thin film. We have seen that the film plays an important role in the fluid dynamics of Plateau borders by setting additional flow boundary conditions.

Using the same set-up, we study what happens when the film vanishes and the two Plateau borders merge (regime II in Fig. 4.2). This is achieved either by bringing the plates together at constant flow rate, or by increasing the flow rate whilst keeping the plate separation D constant. For easier experimentation, we decided to do the latter.

Fig. 4.2 shows the possible geometries of the cross-section of the rivulet as the flow rate is increased. For low flow-rates (regime I in Fig. 4.2) the system consists

of the two separate Plateau borders studied in the previous section. Their self-similar cross-sectional area A_{PB} increases as $Q^{1/2}$. For high flow rates (regime III in Fig. 4.2) the two Plateau borders are merged, forming a liquid bridge between the plates. The geometrical boundaries of its cross-section are given by the walls and two semi-circles with radius of curvature $D/2$. Arguments of self-similarity upon change of flow rate cannot be employed in this regime, hence we do not expect to find a power-law relating its width to the applied flow-rate.

For sufficiently small plate separations ($D < 1.4$ mm, because of the meandering instability §4.3) it is possible to study what happens in the transition regime II when the Plateau borders merge. Following geometrical arguments, this happens when $W \approx D$. During this merging process we observe an interesting effect: it appears that the Plateau borders refuse to merge over a fairly large range of flow rates. This shows up as a plateau in the $W(Q)$ curves with $W = $ const. $\approx D$. Fig. 4.7 a) shows two sets of data for $D = 1$ mm and $D = 1.2$ mm. Before the onset of the plateau, the curves correspond very well to the predicted power law $W \sim Q^{1/4}$. Unfortunately, data can only be taken up to the onset of the meandering instability. We do not believe that this plateau is related to the instability itself. This is because the instability is also observed for large plate separations for which the Plateau borders never merge.

Assuming that the flow rate at the end of the plateau is a certain multiple of that of that of the onset, we sketch a $Q - D$ phase diagram for the three rivulet cases, which is shown in Fig. 4.7 b). The area shaded in dark gray represents the flow rates and plate separations for which we expect to find the "non-merging" Plateau borders. The area shaded in light gray represents the phase space of the unstable meander (see §4.3.2.2). In this presentation, the $W(Q)$ data sets are given by straight, vertical lines.

From the phase diagram we expect to be able to measure full plateaus and the W-variation for regime III for sufficiently small plate separations. This, however, requires experiments to be conducted with a precision which we cannot provide with our equipment. Furthermore, measurements for small D tend to be less reliable, as the very thin (therefore light) Plateau borders of small interface area get pinned to the plates very easily and therefore tend to be of rather irregular shape – even before the onset of the
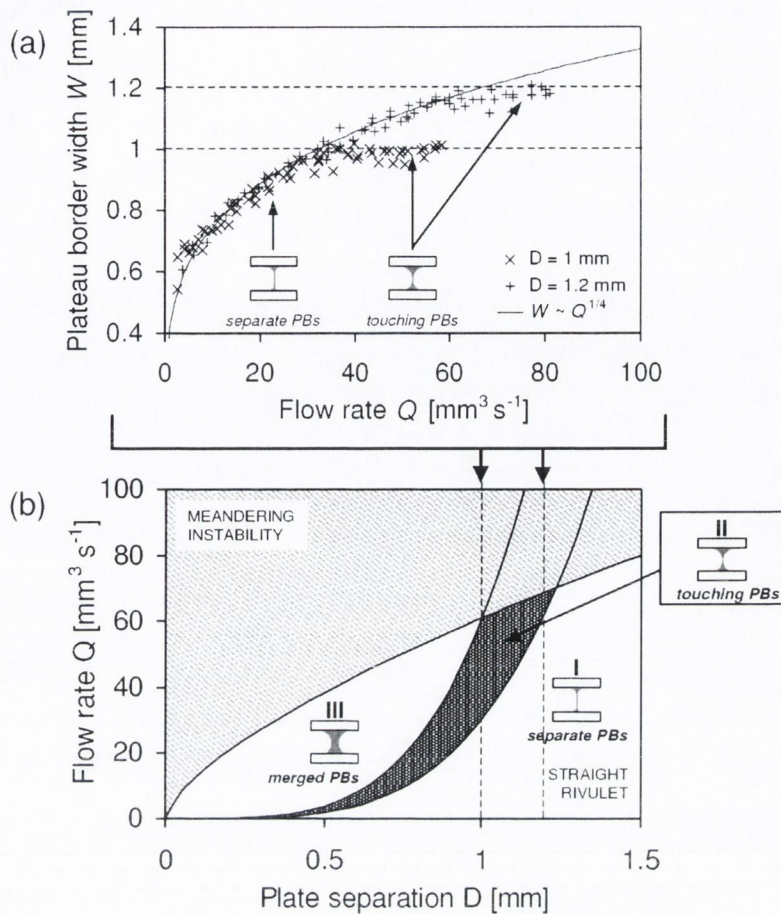
Figure 4.7: Plateau borders refuse to merge: a) The Plateau border width W remains constant over a significant range of flow rates Q when both Plateau borders touch. This shows up as a plateau with $W(Q) = \text{const} = D$. b) Sketch of a Q–D phase diagram for the three rivulet cross sections shown in Fig. 4.2. In this presentation the data from a) represents vertical lines crossing various regimes.

instability.

We have not observed any hysteresis upon increasing or decreasing the flow rate.

We believe that these observations may be explained using very similar arguments to the ones employed in the previous section. Even though the "fixed corner approximation" does not seem to apply for the flow rates and film widths (not thickness) considered here, this point still seems to be of lower mobility than the free gas/liquid interface. We concluded this from the fact that the film moves at significantly lower velocities than the average velocity calculated for the flow in the Plateau borders. As this film vanishes, the Plateau border corners are slowly released until the system consists

of two large, separate gas/liquid interfaces which are much less resistant to shear.

To sum up, we argue that once again an increase in flow rate is compensated by a change in boundary conditions, rather than an increase in the rivulet width.

4.2.3   Conclusions, outlook and remaining challenges

We have been able to demonstrate that our theoretical understanding of fluid flow in Plateau borders ties in well with our observations for low flow rates. For higher flow rates, however, we need to develop a much better understanding of the flow boundary conditions at the gas/liquid interfaces and Plateau border corners. These conditions have a significant influence on foam drainage and should therefore receive close attention.

The most important conclusions from this work could be summarised as follows.

- At high drainage rates interfaces are significantly sheared, even with surfactants known to make very rigid interfaces.

- The assumption of zero flow velocity at the Plateau border corner "S" only holds for low flow rates. Its finite velocity and width has to be taken into account. This problem is re-visited in Chapter 5.

Computer simulations in the style of Nguyen [88] and Koehler et al. [73] are heading into the right direction, but should be taken further to consider the finite flow velocity at the Plateau border corner. They should furthermore go hand in hand with thorough experimental investigations of various surfactant systems and Plateau border geometries. Particle velocimetry seems a very good method to obtain velocity profiles in the Plateau borders [73]. Laser-Doppler velocimetry may be a good method to measure the local interface velocities.

An assumption that we would suggest to consider more carefully in the future is that of the interfaces being approximated by arcs of circles. At high flow rates, the locally varying interface velocity and dynamic surface tension should surely have an effect on the Plateau border geometry and hence its fluid dynamics.

To make things even more complicated, shear thinning effects might come into play as well. This would result in even lower interface mobilities at higher flow rates

and might already play a role in the effects reported in this Chapter.

Most of all, we will have to establish quantitative criteria in order to be able to decide under which circumstances the traditional assumptions can be confidently applied.

4.3 High flow rates - meandering instabilities

4.3.1 Introduction

As part of an investigation into various instabilities that are encountered in the physics of foams [125, 126], we explore the stability of the rivulet discussed in the previous chapter. A surprisingly rich variety of phenomena is observed for flow rates such that the straight downward motion of the rivulet becomes unstable, causing it to meander. The meandering ranges from sinusoidal waves of small amplitude to serpentine waves of larger amplitude. The waves can travel either upward or downward. More complex waves and disordered motion are observed in some regimes. The ensemble of these results presents a complicated scenario and a considerable challenge to theory, of which we have only some elements at this stage. Analogous, but much less regular patterns are familiar from investigations of the meandering motion of a rivulet on an inclined hydrophobic plane [86, 121, 85, 109]. Our system, however, seems to be quite distinct in its behaviour and produces elegant wave patterns that have no counterpart in earlier work, so far as we are aware. For a more detailed comparison of both systems refer to §4.3.5.

4.3.2 Experimental results and analysis

4.3.2.1 Main Observations

Fig. 4.8 encapsulates much of the content of this chapter. It indicates the various regimes that are encountered as the flow rate is increased.

For low flow rates we observe the straight, vertical rivulet which has been studied in detail in §4.2.2. At a critical flow rate Q_1 it becomes unstable assuming the shape of a sinusoidal *upward* travelling wave. The wave velocity is finite at the point of onset
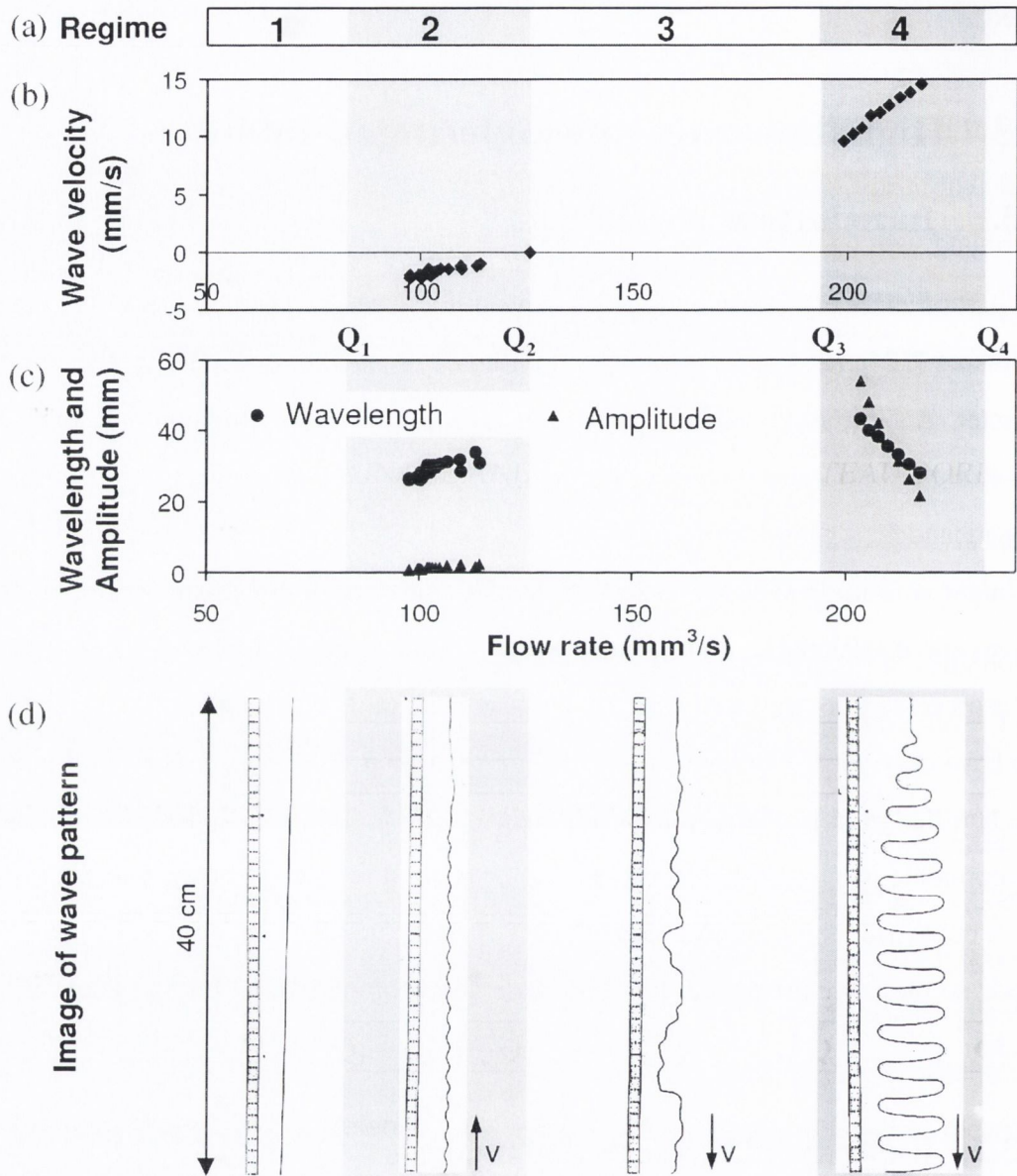
Figure 4.8: Overview of the physical characteristics of the wave patterns in the four distinguished regimes found for different flow rates. This data is taken for a plate separation of $D = 2$ mm. A detailed description of the phenomena can be found in §4.3.2.1. a) Regime. b) Wave velocity. bc) Wavelength and Amplitude. d) Photograph of the pattern.

Q_1, and decreases steadily in regime 2 up to a second critical flow rate Q_2, where it vanishes. At this point, a stationary wave is observed. Beyond Q_2 we observe a motion similar to the garden hose instability just below the inlet, whose frequency increases with flow rate. This results in downward travelling waves of irregular form in regime 3. Only when a much higher flow rate Q_3 is reached does the pattern restabilise (beginning at the inlet). The pendulum motion below the inlet now generates essentially perfect, downward travelling waves of large-amplitude, serpentine form in regime 4. In this regime the amplitude increases linearly close to the inlet, but eventually tends to a limiting value further down. This value decreases with flow rate, leading to increasingly sinusoidal wave forms at the end of regime 4. For even higher flow rates, the rivulet breaks into sub-rivulets which, due to the surfactants, do not detach from the main rivulet and hence generate a foam between the plates.

Of the three regimes which exhibit travelling waves, 2 and 4 have proven to provide the most reproducible behavior. We shall concentrate on these for the analysis in §4.3.2.2 and §4.3.2.3.

4.3.2.2 Regime 2

In regime 2 we observe the onset of the instability at a very well defined flow rate Q_1, which depends on the plate separation. The small-amplitude, sinusoidal waves travel upwards. Their velocity decreases with increasing flow rate until a stationary wave is obtained at Q_2, marking the end of this regime. Amplitude and wavelength increase with flow rate, as seen in the example in Fig. 4.8.

The variation of the wave velocity V (upward and hence negative in our convention) with flow rate Q may be explained or rationalised as follows. In a simple model we consider the forces acting horizontally on a segment of the slender rivulet at the point of maximum amplitude. We believe the two key ingredients to be the destabilising centrifugal force F_c, caused by the liquid being forced around the bend of local curvature κ,

$$F_c = 2 A_{PB} \rho (U - V)^2 \kappa, \qquad (4.8)$$

and the stabilising surface tension force F_γ related to the same curvature,

$$F_\gamma = 2\,D\,\gamma\,\kappa. \tag{4.9}$$

Here U is the average fluid velocity in the Plateau borders, ρ the fluid density, D the plate separation, A_{PB} the cross-section of one Plateau border and γ the surface tension. For the derivation of F_c see APPENDIX B. Liquid flow through the thin film connecting the Plateau borders is neglected in the derivation of F_c. The surface tension force is roughly estimated by ignoring the Plateau borders, so that a film of width D spans the plate. Note that both forces are proportional to κ.

In equilibrium $F_c = F_\gamma$. Equating (4.8) and (4.9), and expressing U and A_{PB} through Q as given by the equations (4.4) and (4.6), we obtain for the wave velocity

$$V = -a\,Q^{-\frac{1}{4}} + b\,Q^{\frac{1}{2}}, \tag{4.10}$$

with

$$a = (\gamma\,D)^{\frac{1}{2}} \left(\frac{2g}{\rho f \eta} \right)^{\frac{1}{4}} \quad \text{and} \quad b = \left(\frac{\rho g}{2f\eta} \right)^{\frac{1}{2}}. \tag{4.11}$$

This is negative for low Q and becomes positive beyond a critical value which we identify with Q_2 in Fig. 4.8. Downward travelling waves, roughly consistent with this trend, are indeed observed in regime 3. But we have refrained from trying to characterize them here in account of their disordered form.

Even though the model qualitatively reflects the system's key behaviour, it fails to quantitatively reproduce the experimental figures. Note furthermore, that since both forces employed in the model scale with κ, it is not elaborate enough to reproduce the observed wavelengths at the onset (see Fig. 4.9).

For the steady wave at Q_2 we establish a relationship between the flow rate and the plate separation by setting $V = 0$ in Equ. (4.10),

$$Q_2 = \frac{2}{\rho} \left(\frac{f\eta\gamma^2}{g} \right)^{\frac{1}{3}} D^{\frac{2}{3}}. \tag{4.12}$$

Unfortunately, Q_2 is difficult to determine experimentally, as the wave velocity varies gradually over a fairly large range of flow rates. Qualitatively it can be said that the flow
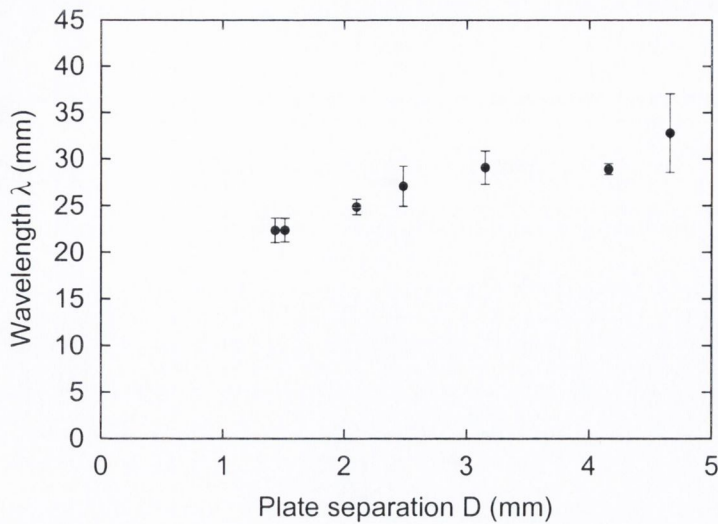
Figure 4.9: Wavelength λ at the onset of the instability as a function of plate separation. We have no model yet to describe this data.

rates obtained for stationary wave patterns are about twice as high as those predicted by Equ. (4.12).

Measurements of the flow rate Q_1 at the very well defined onset of the instability as a function of plate separation (Fig. 4.10) display the proportionality predicted in Equ. (4.12) very well. The data is fitted to $Q_1 = \alpha \, D^{2/3}$, with $\alpha = (57.7 \pm 1.4) \, \mathrm{mm}^{7/3}\mathrm{s}^{-1}$, which is about one third of what is theoretically predicted for Q_2 in Equ. (4.12) using f determined in §4.2.2.1.

We have as yet no theoretical explanation of the onset of the instability, but the above argument leads us to believe that it occurs at a certain fraction of Q_2. A more elaborate model is needed, in particular, to account for the measured wavelengths at the onset of the instability (see Fig. 4.9) and the deviation between the quantitative predictions of the model and the experimental findings. At this stage our derivations either lack important ingredients, or first-order approximations do not suffice for the description of the problem. Among other attempts we have tried to take into account normal and tangential dissipation. But we have not succeeded so far in finding a model that leads to a physically meaningful dissipation relation. This may be the point where the properties of the wetting film could come into the equation, literally.

For reasons yet unknown, we observed an *anomalous dispersion relation* in regime
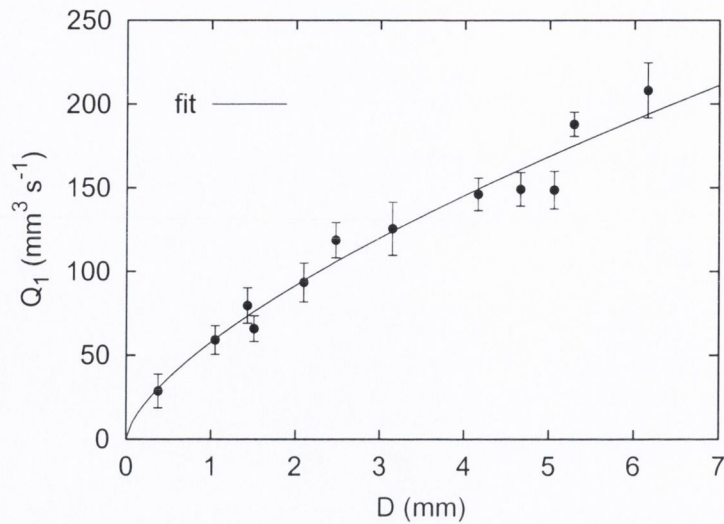
Figure 4.10: Flow rate Q_1 at the onset of the instability as a function of plate separation D. The data is fitted with the power law $Q_1 \sim D^{\frac{2}{3}}$ (compare Equ. (4.12)).

2, meaning we occasionally found that the wavelength decreases with increasing flow rate (see Fig. 4.11).

4.3.2.3   Regime 4

In this regime, the rivulet performs a pendulum motion below the inlet, which generates highly regular, downward-travelling wave patterns. The frequency of the pendulum motion depends on the nozzle size (unlike in regime 2), the plate separation and the flow rate. So does the wave velocity V, which is shown in Fig. 4.12 for three different plate separations. V seems to depend linearly on the flow rate Q, with the slope being similar for all plate separations and nozzle sizes, but shifted along the Q axis. As the waves descend, their amplitude A and wavelength λ grow in a very linear manner until they saturate.

Fig. 4.13 shows the variation of amplitude A and wavelength λ with distance from the inlet for various flow rates in regime 4. In some cases a fitting procedure[2] is needed to infer the limiting values. Like the pendulum frequency, these values depend on the nozzle size, with smaller nozzles resulting in higher undulation frequency, higher wave

---

[2]The data was fitted to $F(x) = A(1 + Bx^{-C})^{-1}$, with A, B and C being the fitting parameters. There is no physical reason for using this formula, apart from the fact that it describes the data very well.
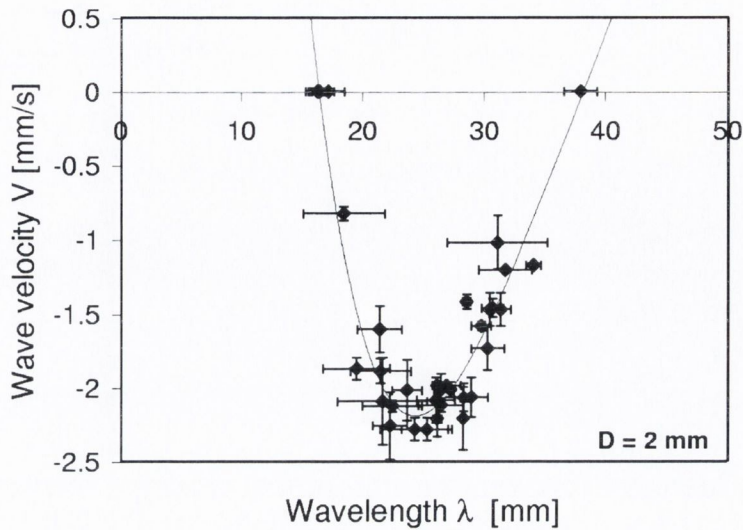
Figure 4.11: Anomalous dispersion relation for the wave velocity at the onset of the instability.
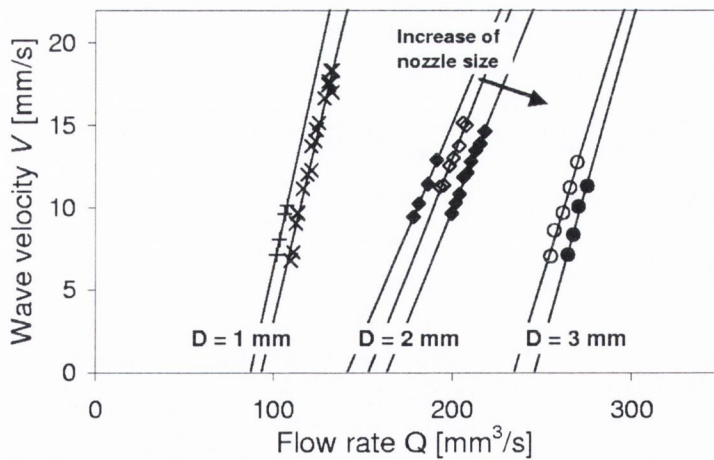
Figure 4.12: Wave velocity V as a function of flow rate for three different plate separations, $D = 1, 2$ and 3 mm. The different lines for each plate separation correspond to different nozzle sizes.
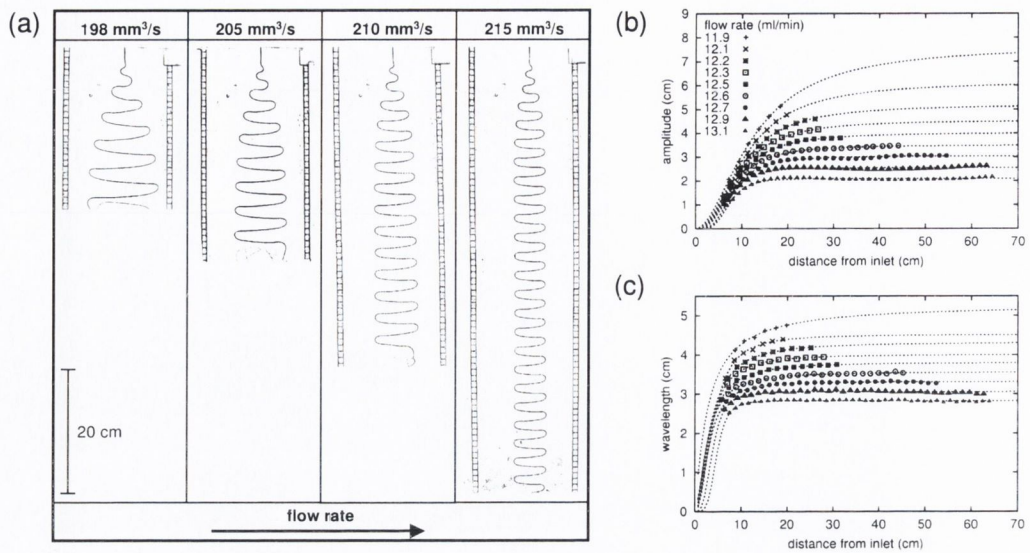
Figure 4.13: Wave pattern in regime IV (here $D = 2$ mm): a) Photographs of the rivulet for different flow rates. The length of the pattern is determined by the instability of large amplitudes. b) Variation and saturation of amplitude and c) wavelength with distance from inlet, including the data from the images of a).

velocity and smaller amplitudes/wavelengths. We found, however, that amplitudes and wavelengths for *all* nozzle sizes can be related to the plate separation D in a very simple way, as all of the acquired data conforms well to

$$\lambda^2 \sim AD. \tag{4.13}$$

This is demonstrated in Fig. 4.14, which comprises data for different plate separations and nozzle sizes. The fitted curve is given by

$$\lambda D^{-\frac{1}{2}} = (4.55 \pm 0.01)\, A^{(0.45 \pm 0.01)}. \tag{4.14}$$

It is clear that the large-amplitude serpentine waves of regime IV are not a simple continuation of the trends discussed in §4.3.2.2 for lower flow rates. We believe this is because the trend to larger amplitudes, and hence larger maximum curvature, eventually encounters an upper bound on the possible curvature of the rivulet. To see this, consider the same type of argument as advanced above, but applied only to the thin film which spans the plates between the Plateau borders. This has negligible inertia and hence negligible centrifugal force: hence the surface tension force on an element
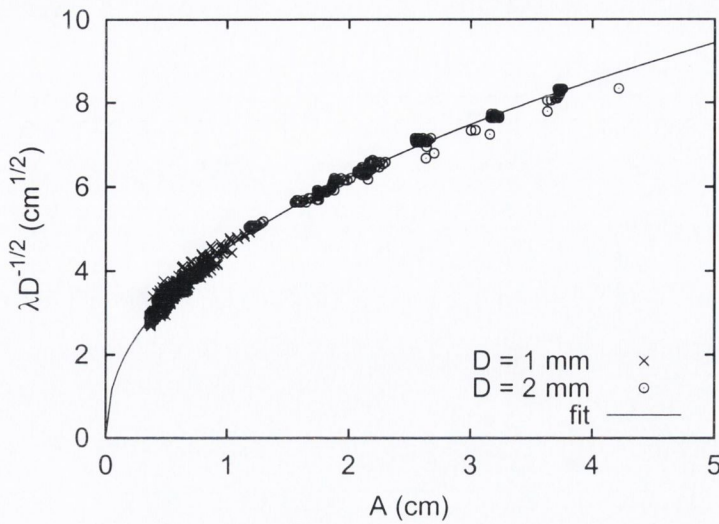
Figure 4.14: Data for different plate separations, nozzle sizes and flow rates collapses on the same graph when $\lambda D^{-1/2}$ is plotted against A.

of film must be approximately zero. This means that the two principal radii of curvature – one parallel to the plane of the plates, the other perpendicular – must be equal and opposite. Any increase in the curvature of the rivulet must be matched by an equal and opposite increase of the transverse curvature. So long as the Plateau borders are small, this transverse curvature cannot exceed $2/D$, where D is the plate separation. We therefore attribute to the remarkable relation (4.13) the significance of maintenance of approximate constant curvature, close to its maximum allowed value.

This general idea may be mathematically expressed in an admittedly simplistic model: The local curvature $\kappa(x)$ of a sinusoidal wave pattern $y(x) = A\ e^{ikx}$ with $k = 2\pi\lambda^{-1}$, can be derived to be

$$\kappa(x) = \frac{d^2 y(x)}{dx^2} = -\frac{4\pi^2}{\lambda^2}\, y(x). \tag{4.15}$$

Which, assuming constant curvature κ_0 for the points of maximum amplitude, would give us the relationship

$$\lambda^2 = \frac{4\pi^2}{\kappa_0}\, A. \tag{4.16}$$

Assuming that $\kappa_0 = 2/D$, as reasoned above, we obtain

$$\lambda D^{-\frac{1}{2}} = \sqrt{2}\ \pi\ A^{\frac{1}{2}}, \tag{4.17}$$

identifying the constant of proportionality as $C = \sqrt{2}\,\pi \approx 4.44$, which agrees extraordinarily well with the fitting results from Equ. (4.14).

However, while this argument may have identified the correct physical basis for the relation, in detail it relies on assumptions, namely small Plateau borders and sinusoidal waves, which do not apply well in regime 4. Clearly a detailed analysis is called for and should be possible using such tools as the Surface Evolver [16] in combination with more detailed fluid dynamic simulations.

4.3.3   The role of the wetting film

Due to the vanishing contact angle of surfactant solution on glass, the surfaces of the plates are coated with a wetting film in the vicinity of the moving rivulet. The precise role of this surrounding film is not clear, but it may well be responsible for some of the patterns and trends observed. In particular, it could have a significant contribution to the stabilisation of the wave patterns and hence play a similar role to that of contact angle hysteresis in the traditional meandering experiments on hydrophobic surfaces. Stabilising forces could, for instance, be related to the Gibbs elasticity (§1.4) of the wetting film. This could be caused by local depletion of surfactant concentration in the gas/liquid interface as a result of the rivulet dynamics.

Fig. 4.15 gives some indication of the existence and motion of the wetting film. It shows monochromatic light interference patterns of a downward sliding wave in a sequence of successive time steps (0.2 s intervals). The interference pattern in the background of the black rivulet displays the thickness variations of the wetting film as the rivulet is sliding across it (V= 20 mm/s). Surprisingly, this pattern seems to be more or less static with respect to the glass plates, rather than to the rivulet.

4.3.4   Further observations

In view of the wide extent of the data presented here, we do not elaborate it with any detailed consideration of various further effects that we have observed. These include the occasional observation of waves which appear to contain two Fourier components, "beating" together (Fig. 4.3.4 a)). Also, for wave patterns with large amplitudes or
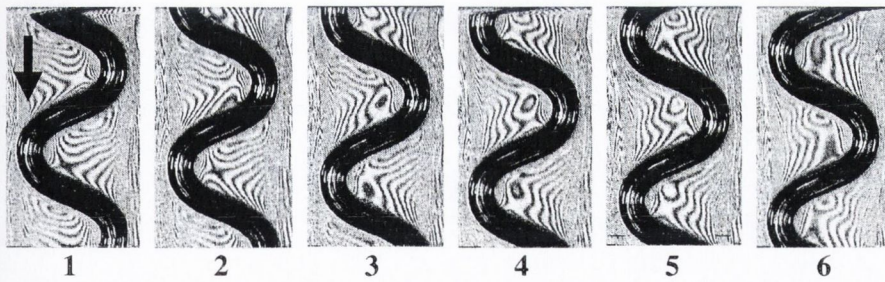
Figure 4.15: Observation of the wetting film using monochromatic light interference. Images 1-6 display successive time steps of a downward sliding wave in regime IV.

at very high flow rates, there is a local thickening of the rivulet, leading to "varicose" instabilities (Fig. 4.3.4 b) and c)).

The rivulet width varies significantly along the wave pattern for high flow rates, with the horizontal parts of the rivulet being distinctively thicker than the vertical parts. There does not seem to be a general rule for the respective rivulet cross-sections (according to Fig. 4.2) required to produce a stable wave pattern, as these depend on the plate separation D. We can state, however, that if D is chosen such that the vertical parts of the rivulet have a cross-section of type I (Fig. 4.2), the waves are much better behaved. We believe that this can be attributed to the stabilising effect of the thin film formed between the Plateau borders.

Unlike in the meandering on non-wetting planes [32], hysteresis does not seem to play a role in this experiment as long as the plates are wetted evenly. This means that a pattern obtained for a specific flow rate Q does not depend on whether Q has been increased or decreased up to that point.

Attempts to reproduce the patterns with chemically more pure and better characterised surfactants than Fairy have not proven successful in generating such regular and stable patterns. Using pure liquids (no surfactant) with very low surface tension (e.g. silicone oil) resulted in irregular patterns. Experiments with pure de-ionised water between glass or Plexiglas plates produce patterns very similar to those encountered in the meandering of water on hydrophobic surfaces (refer to §4.3.5), displaying very clearly the effects of pinning and contact angle hysteresis. But despite of the lack of regularity of the wave patterns, all systems mentioned in this paragraph display the
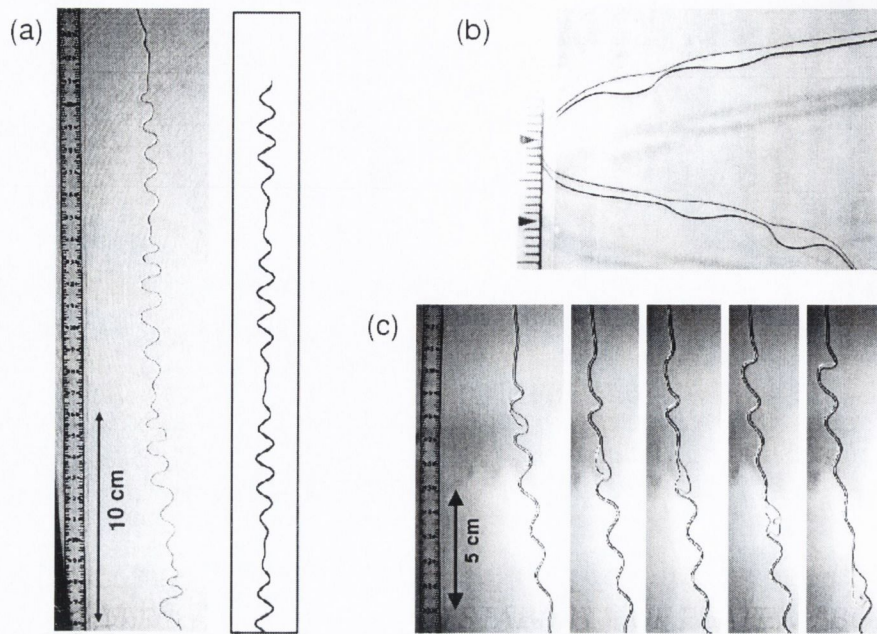
Figure 4.16: Some oddities observed in regime 4: a) Example of an experimentally observed and computationally generated "beating" pattern of two sinusoidal waves with a wavelength ratio of 5:6. The component with smaller wavelength travels down faster within the pattern. b) For large amplitudes a thickening instability develops on the horizontal sections of the rivulet. c) For very high flow rates a localised thickening might develop and travel downward in the rivulet without spreading out. The image sequence shows this process with the images being 0.2 s apart.

well defined instability at a critical flow rate.

4.3.5   Comparison with other meandering phenomena

Despite its significance for industrial applications and fundamental science, research on stream meandering has been surprisingly limited. Most of the experimental work up to date investigates the properties of rivulets of various liquids on inclined, non-wetting planes [67, 68, 31, 32, 86, 85, 109]. As in our case, these systems display several regimes with fairly well defined transition regions. With increasing flow rate these regimes have been identified to be: (i) individual droplets, (ii) straight rivulet, (iii) stable meandering rivulet, (iv) unstable meandering rivulet and (v) restable rivulet. Due to the irregularity of the patterns, quantitative analysis has been restricted to measurements of the sinuosity of the meanders, which is the ratio of total length of the rivulet to the distance between inlet and bottom of rivulet. Several attempts have been made to

map out phase diagrams of the various regimes, with one of the key parameters being the inclination of the surface.

Theoretical work has been similarly scarce, being limited to rather specific aspects of the problem or suffering from fairly strong simplifications [117, 33, 132, 34, 136, 18, 70]. Some of the models predict aspects of the experimental results, but fail to describe a more complete picture.

In general, the gap between theory and experiment seems to be rather large, seemingly dominated by the struggle to fully understand and implement the role of contact angle hysteresis.

Our system resembles that described above, the key similarities being the stabilising effect of surface tension forces and the destabilising effect of centrifugal forces of the liquid being forced around bends in the rivulet. However, as a result of the different set-up and wetting properties, certain aspects differ significantly and might help to overcome some of the difficulties encountered in the traditional work on meandering phenomena. The advantage of our system lies in its accessibility and the remarkable regularity of the wave patterns observed. Due to the rivulet being contained between two vertical surfaces, its cross section is well defined and measurable. Furthermore, the existence of a wetting film (see §4.3.3) eliminates the problems of contact angle hysteresis and pinning effects and hence leads to nearly perfect, travelling wave patterns, which can easily be analyzed and compared to theoretical models in terms of wavelength, amplitude, local curvature or rivulet width.

Detailed comparison between experimental results for stream meanders is difficult as a result of the different geometries and physical properties of the investigated systems, and the different parameters which researchers have focused on. However, a few general comparisons can be made: We do not observe rivulet breakup into separate droplets (low flow rate) or sub-rivulets (high flow rate) as a result of the surfactant loaded interfaces forming highly stable films. The overall characteristics of the various regimes seem to be similar and we are tempted to draw parallels between the "stable meandering" (iii) and our regime 2, and between the "unstable meandering" (iv) and

our regime IV. Nakagawa [85] reports an increase of sinuosity with flow rate in the former and a decrease in the latter, which is what we see in terms of increasing (regime 2) and decreasing (regime 4) wavelengths and amplitudes. The "unstable meander" was termed "pendulum rivulet" by Schmucki [109]. Its properties, especially its relationship between decay frequency and flow rate, are strikingly similar to our observations in regime 4. Our rivulet, however, does not break up into sub-rivulets, but stabilises into very regular, travelling waves.

We have not observed any surface waves, which seem to precede the onset of meandering on non-wetting surfaces [85, 109].

4.3.6   Conclusions, Outlook and remaining challenges

We have introduced novel investigations of a simple system which we believe will greatly enhance our understanding of the science of meandering. Our system poses many advantages over those employed for the traditional work on meandering on hydrophobic surfaces (see §4.3.5). It produces extremely regular and well controlled wave patterns, which will permit straightforward analysis and study of a great variety of physical and chemical parameters. It is very rich in interesting effects, and a successful and comprehensive theory may well be just as rich in interest. We therefore expect that this work will trigger a new wave of theoretical and experimental studies of meandering problems.

It remains to be seen how the underlying physics relates to seemingly similar problems such as that of §4.3.5, and also to fluid-structure interactions [90], such as the "garden hose instability", or viscous fluid buckling [30, 116].

In addition, we hope to employ our investigations for improving our understanding of foam drainage and dynamic effects in high velocity flows in Plateau borders and soap films.

Chapter 5

Flow in soap films

5.1 Introduction

The previous chapter focused on the flow of liquid through Plateau borders. There, the film connecting the two Plateau borders only played a role in terms of providing a restoring surface tension force or a specific flow boundary condition where it is joined to the Plateau border. In the discussions of Chapter 4 it became obvious that the general assumption of no slip at this point has to be reconsidered for higher flow rates.

Most work up to date neglects the contribution of films to drainage. For wet foams and high drainage rates it seems to become increasingly obvious, however, that a better understanding of the film dynamics and its contribution to foam drainage is required.

Therefore, this chapter is entirely devoted to observations of forced drainage through films of sizes of the order of a few square millimeter to centimeter. These films are "framed" by surface Plateau borders as we encountered them in the previous chapter. In order to allow for comparison with our previous work and enable us to put observations into a broader perspective, all experiments are carried out with Fairy and SDS, which are known to form very rigid and mobile interfaces, respectively.

The work introduced here is of highly exploratory character. As the observed effects are of rather complex nature, we will restrict ourselves to mostly qualitative descriptions and general conclusions and speculations.

A lot of research has been conducted on freely draining soap films [84] during the last century. However, it focused merely at the very bottom of the range of drainage velocities and film widths encountered in the dynamics of wet foams. The opposite

end of this regime has been studied extensively with a very different focus: quasi-2D film flow provides a powerful (and extraordinarily beautiful) tool for the experimental study of 2D-turbulence in fluid dynamics [24, 21, 51, 66, 105]. Results of this research can only guide our own exploration, as it focuses on yet another extreme, namely very large films (often order of square meters) and very large film velocities (several meters per second) of free-falling film. Furthermore, the use of thin fishing wire as a frame for the film suppresses the Plateau borders whose fluid dynamic properties we are trying to understand here.

5.2   Experimental setup

The experimental set-up was aimed at reproducing the constellation studied in the previous chapter, i.e. two surface Plateau borders connected by a film. This time, however, we focused on the dynamics of the film.

In order to obtain more flexibility regarding film size and geometry, we replaced the glass plates by a frame of flexible silicone tubing (5 mm outer diameter) spanned onto a wooden frame. By putting tension onto wires attached to the tubing, a range of film geometries were easily obtained, as demonstrated in Fig. 5.1.

Surfactant solution ("Fairy" [0.4 % by volume] and SDS [0.3 % by weight], both well above the CMC) was injected at the top of the frame at various constant flow rates. These were controlled and monitored by a flow meter with a high precision needle valve, which was attached to a large container providing constant hydrostatic pressure.

Surfactant solution wets silicone tubing slightly less than the glass plates, which has an effect on the size of the Plateau borders. So does the fact that the surface of the tubing is curved. However, these differences should be negligible considering the qualitative nature of the observations reported here. Using glass plates instead of the tubing results in the same overall behaviour.

In order to visualise the flow in the film, we employ the interference of monochromatic light (Sodium $\lambda_S \approx 580$ nm) reflected by the two interfaces of the film. The
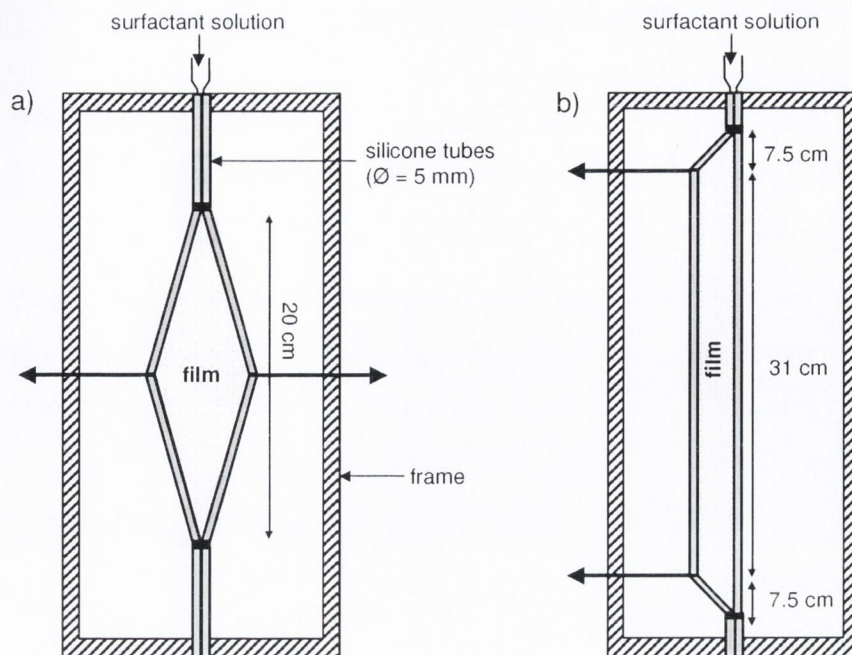
Figure 5.1: Setup to study forced drainage in soap films of various geometry contained between flexible silicone tubes. Surfactant solution is injected at a constant rate at the top of the vertical film.

set-up is the same as in Fig. 4.3, with the film and Plateau borders rotated by 90°. Destructive interference is obtained wherever the film thickness T obeys the following equation

$$T = (n^2 - 1)^{-\frac{1}{2}}(m + 1)\frac{\lambda_S}{2}, \tag{5.1}$$

where $n = 1.333$ is the refractive index of water and m an integer number. Plateau borders appear black in the images due to the large curvature of their interfaces.

Unfortunately, monochromatic light interference only provides measures of relative thickness. In order to obtain absolute film thickness one would have to use more sophisticated methods, which still remains a challenge for films significantly thicker than Newton Black films [105].

In order to obtain a (very) rough idea of the flow direction and magnitude, we probed the film with thin nylon fibers and micron sized nylon particles.

5.3   General observations (Fairy and SDS)

The overall behaviour of Fairy and SDS films over the range of tested flow rates displays striking differences. In the following sub-sections we give a brief description of each case.

Most of the images presented in this section were taken using the diamond shaped film shown in Fig. 5.1 a) with a width of 1.5 cm. The overall observed features are very similar to those of the stretched hexagon in Fig. 5.1 b), but confined to a smaller space and therefore easier to capture in one photograph.

5.3.1   SDS films

Fig. 5.2 a) shows a series of images of the interference pattern of the diamond shaped film for a range of flow rates. Fig. 5.2 b) attempts to sketch the flow directions of the film.

For low flow rates (image 1 & 2 in Fig. 5.2 a)) the motion of the film is turbulent, but overall *upward*, even though the flow in the Plateau borders is directed downward. Upon increase of flow rate (around 20 mm^{3}s^{-1} in this geometry) the film at the top starts to move down. For a range of flow rates the upward moving bottom and the downward moving top compete with each other, forming a beautiful, turbulent transition region which moves down in the film as the flow rate is increased (images 3 & 4 in Fig. 5.2 a)). For even higher flow rates (above $Q \approx 35$ mm^{3}s^{-1}) the whole film moves downward in a laminar flow (image 5 – 7 in Fig. 5.2 a)). For the highest flow rates considered here the film flow velocity seems to be nearly constant over a large horizontal section of the film (image 7). This is the type of flow employed for 2D-hydrodynamic studies [105].

5.3.2   Fairy films

Fig. 5.3 displays a sequence of images for the same film geometry used for the study of the SDS film described above. Sketches of the overall film flow are shown in Fig. 5.4 in comparison with those of the SDS film from Fig. 5.2 b).

For a large range of flow rates (up to $Q \approx 60$ mm^{3}s^{-1}) most of the film moves upward – apart from a small section at the bottom (images 1 – 7 in Fig. 5.3). Unlike in the case of SDS, this motion is much less turbulent, apart from the sections close to the Plateau borders.

The section of film within the transition region between the upward and downward moving part is almost stationary. This region moves up and expands upon increase of flow rate. At $Q \approx 80$ mm^{3}s^{-1} most of the film moves downward at a small velocity of the order of a centimeter per second. The upper part of this section forms a stationary film which we have termed the "Crocodile Belly", for obvious reasons. This stationary film displays beautiful patterns, in particular when irregularities rise in it like bubbles in a liquid (Fig. 5.5).

Experiments with the Fairy film provide us with several more surprises. Looking more closely at the upward moving films we see that *horizontal* thickness variations of about 4 μm (calculated using Equ. (5.1)) are stabilised. This is puzzling and has neither been observed nor explained, as far as we are aware. Fig. 5.6 shows what the interference images of such undulations look like and how they change with flow rate. A similar pattern is introduced and reconstructed in §5.4.

Fig. 5.7 shows an image and the sketched flow pattern of a transition region between two sections of downward (at the top) and upward (at the bottom) flowing film. These regions can be extraordinarily well defined and stable in Fairy films. How these fit into the overall picture is not clear.
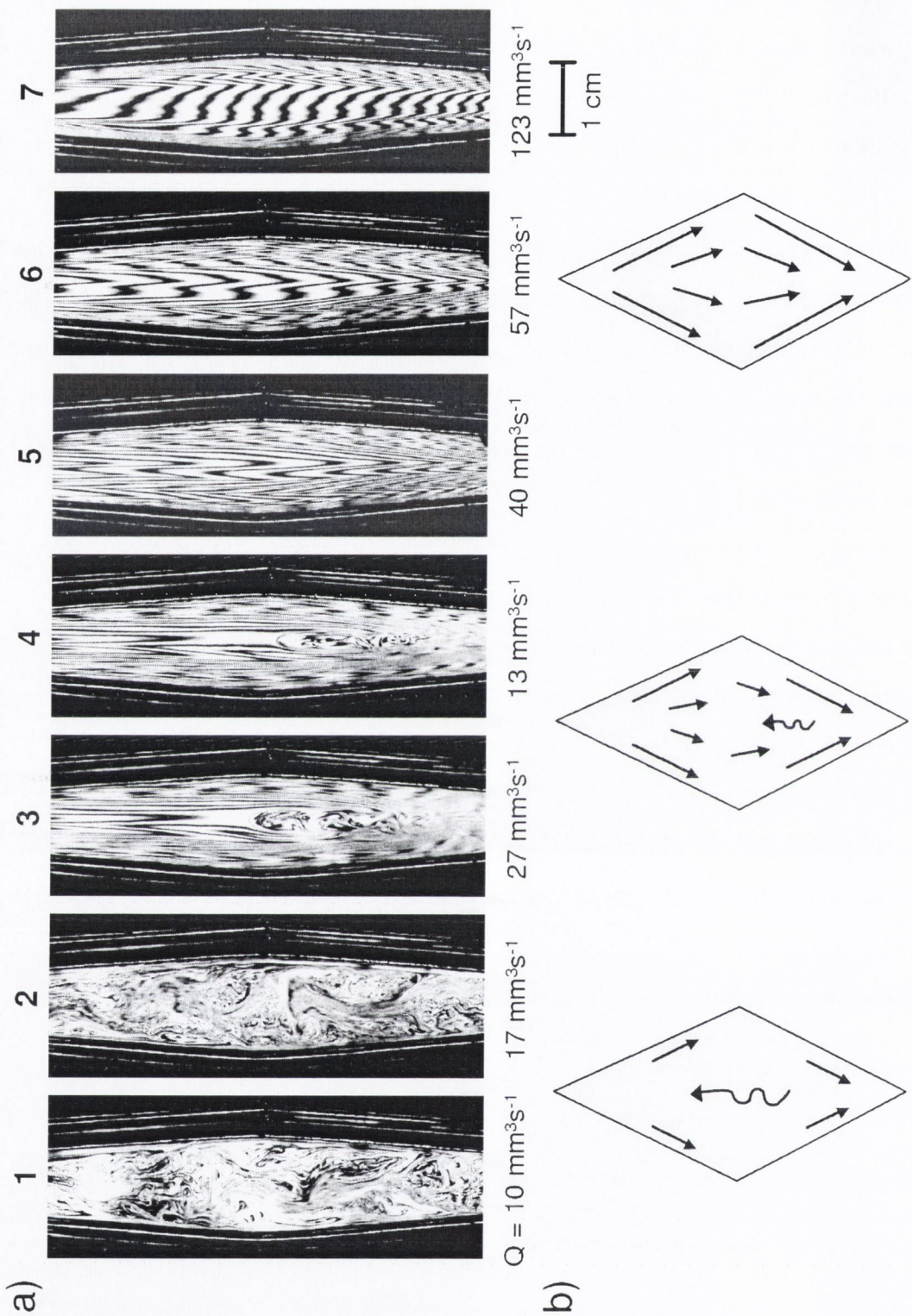
Figure 5.2: a) Interference pattern of an SDS film subjected to forced drainage at increasing flow rates in a diamond shaped film (Fig. 5.1). b) Sketches of the flow direction in the film corresponding to the images shown in a).
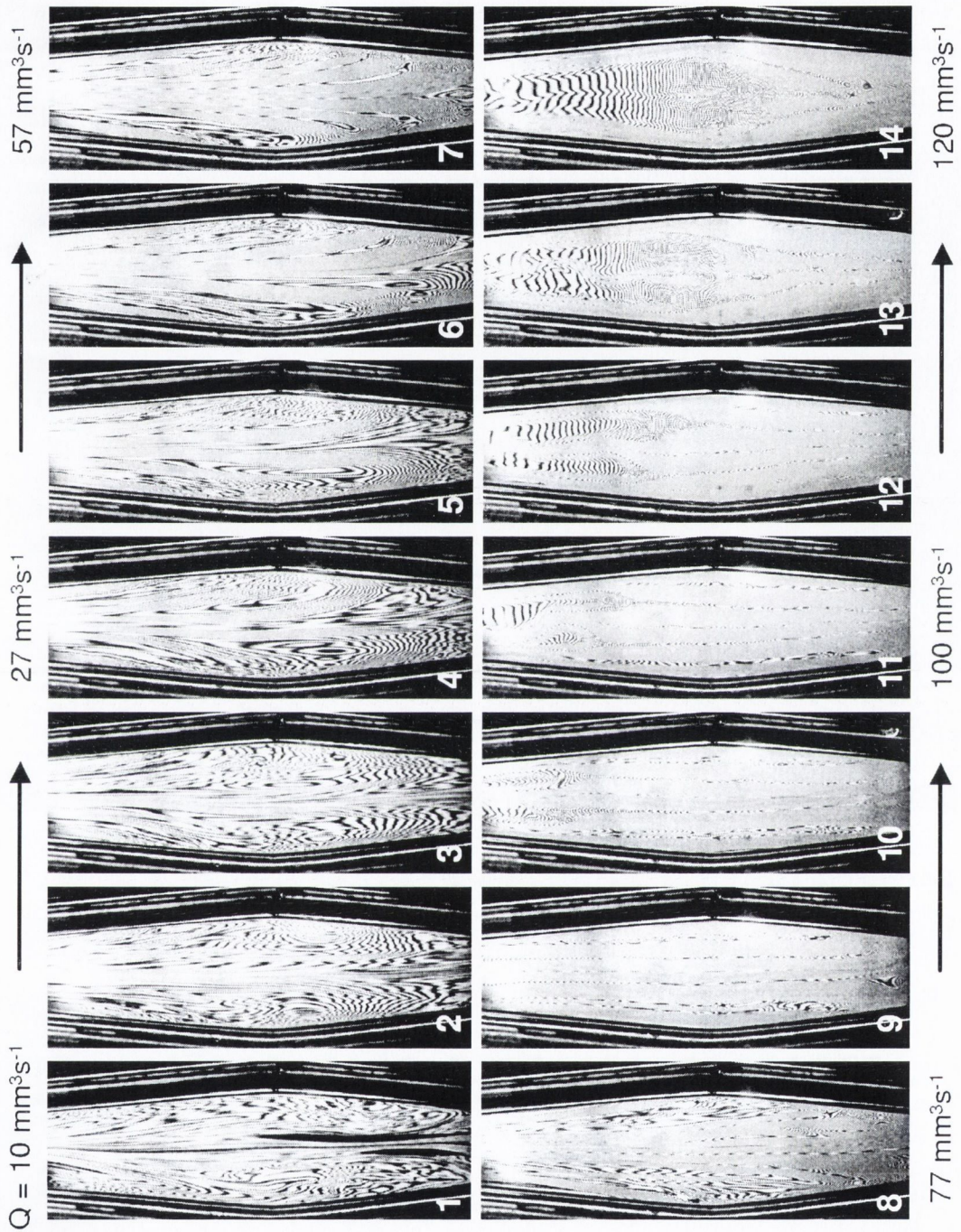
Figure 5.3: Sequence of images showing the interference pattern of a diamond shaped (Fig. 5.1 a)) Fairy film subjected to forced drainage at increasing flow rates. The corresponding flow patterns are sketched in the top row of Fig. 5.4.
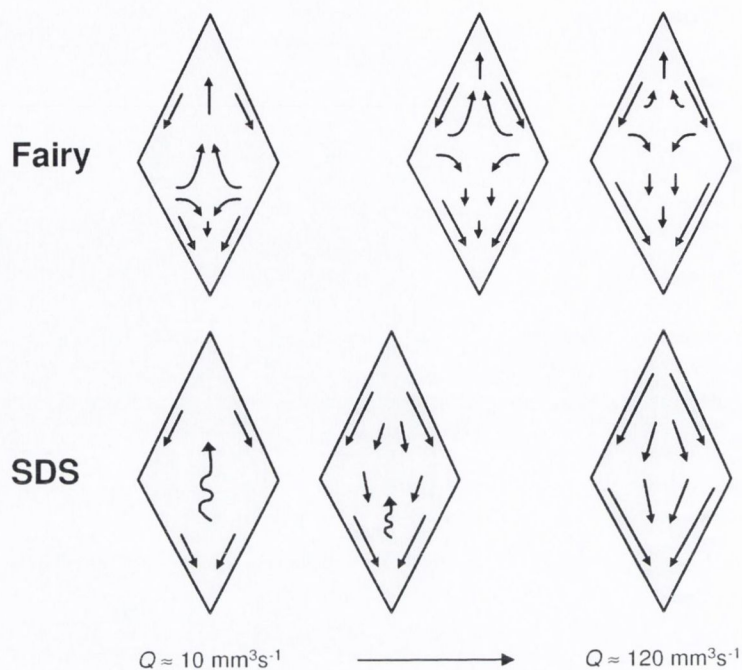
Figure 5.4: Comparison of the overall flow pattern of the Fairy (compare images Fig. 5.3) and SDS film (compare Fig. 5.2) for increasing flow rates.
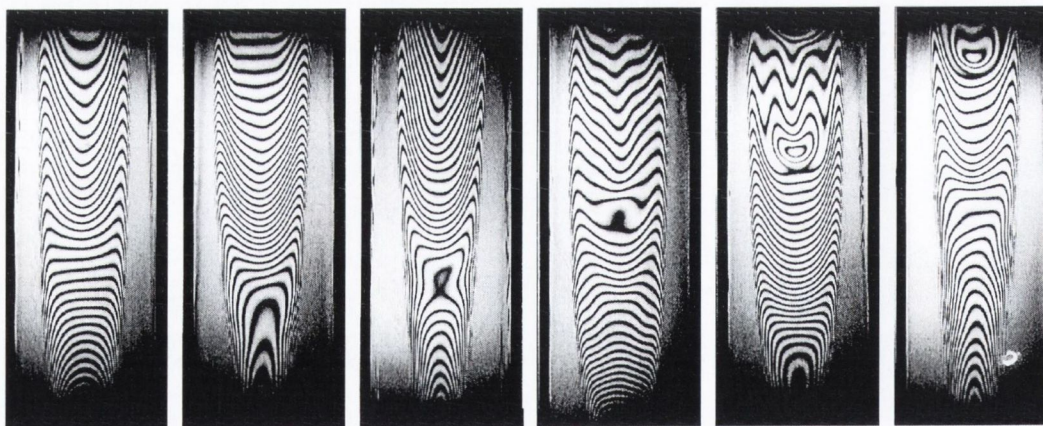
Figure 5.5: These beautiful *Crocodile Bellies* are formed at high flow rates in a Fairy film in the transition region between the upwared moving section at the top and the downward moving section at the bottom. This section of the film is more or less static. The image sequence shows how a piece of (probably) thinner film travels upward through such a Crocodile Belly.
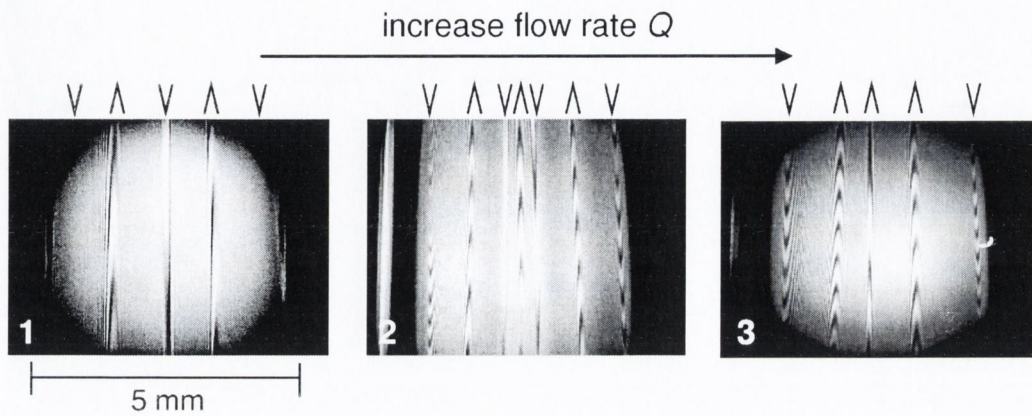
Figure 5.6: These images show the interference pattern at the very top of the diamond shaped Fairy film. The film is moving upward and stabilises a horizontal thickness undulation, whose wavelength seems to depend on the flow rate.
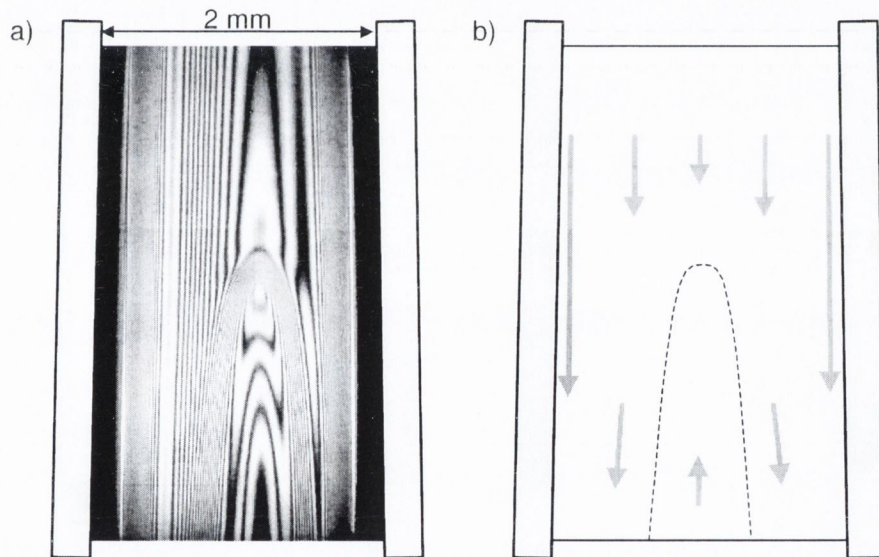
Figure 5.7: In Fairy films we sometimes obtain these type of transition regions, which look similar to those in a SDS film. a) Interference pattern. b) Sketch of flow pattern.
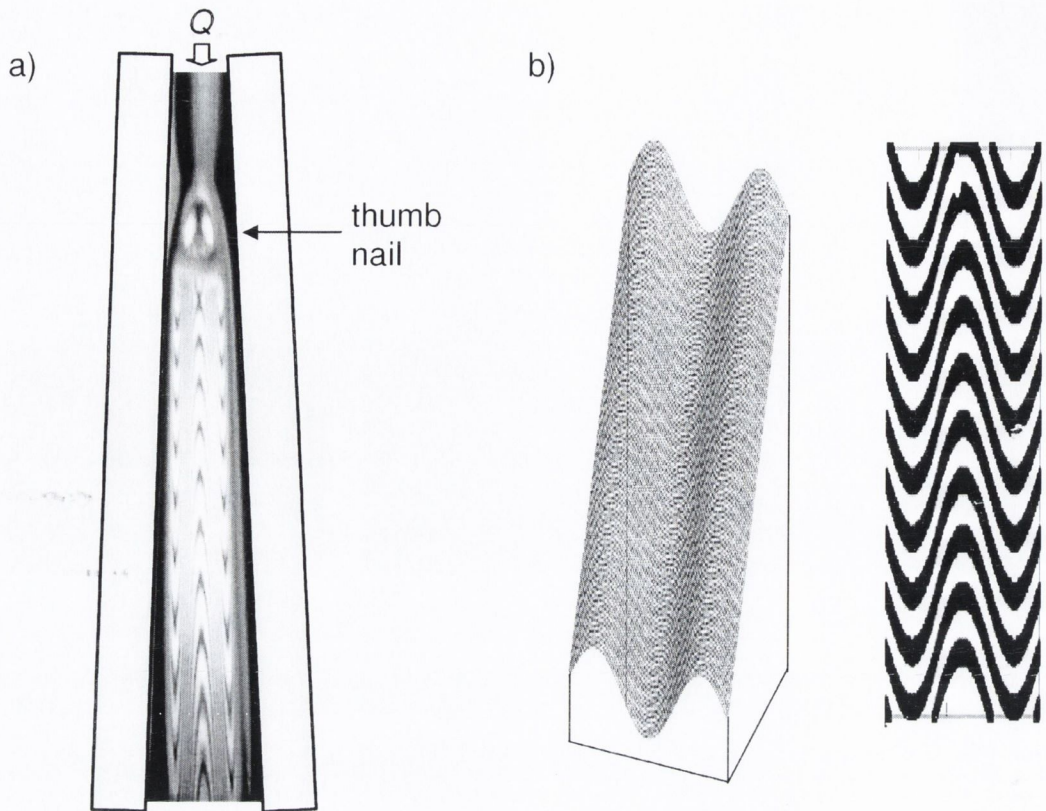
Figure 5.8: a) The "thumbnail effect": it seems that in small, triangular films a vortex is generated by the upward moving film at the Point where the two Plateau borders come apart. The film below the vortex displays a beautiful pattern, whose basic features are reproduced in b) by calculations assuming a linear thickness variation in the vertical and a sinusoidal thickness variation in the horizontal direction of the film. The left image of b) shows the film profile, whereas the right one shows the corresponding interference pattern.

5.4   Small Fairy films - the *Thumbnail*

If the film is sufficiently small (approx. 1 cm^2) and narrow (a few millimeters), we observe a peculiar phenomenon at the very top of the diamond. It seems like the upward moving film in the center generates something that looks like a vortex at the point where the Plateau borders separate (Fig. 5.8 a)). Its size increases with decreasing film area. The film below this *Thumbnail* is just as striking as it assumes a very regular, steady pattern with horizontal thickness variations of up to 2 μm. Fig. 5.8 b) attempts to reconstruct the general characteristic of this pattern by assuming a film width which decreases linearly with distance from the vortex and is subject to a sinusoidal thickness undulation in the horizontally direction. As in §5.3.2, it is not clear what generates and
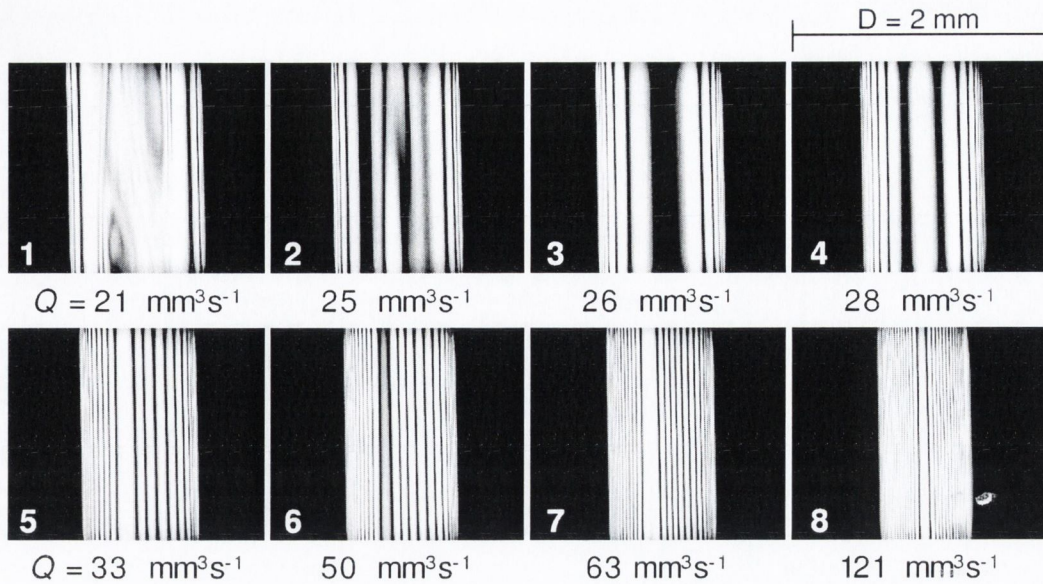
Figure 5.9: Interference images of two surface Plateau borders connected by a thin film formed between two narrowly spaced glass plates ($D = 2$ mm) for increasing flow rates. (1) Upward moving film; (2) Transition point where the film starts to move downward; (3)-(8) Downward moving film of increasing thickness and curvature. The flow in this film is highly laminar.

stabilises this pattern.

We had hoped that experiments of this type might elucidate some of the questions raised concerning the merging or separating of Plateau borders. Up to now we have not been able to relate these observation with the ones reported in §4.2.2.2. They might be of quite different nature as here we deal with non-parallel Plateau borders. The different geometry might lead to quite different dynamic effects.

5.5 Narrow films

The narrower the films the lower the flow rates that are required to drag the whole film along with the flow in the Plateau borders. As already mentioned in §4.2.2.1 and shown in Fig. 4.6, this has important consequences for the average flow velocity in the system. Most of all it shows that the assumption of fixed Plateau border corners has to be reconsidered for higher flow rates.

Fig. 5.9 shows an extensive series of images of the film between two Plateau borders between two glass plates of separation $D = 2$ mm for various flow rates. In this particular case we used glass plates instead of silicone tubes in order to allow
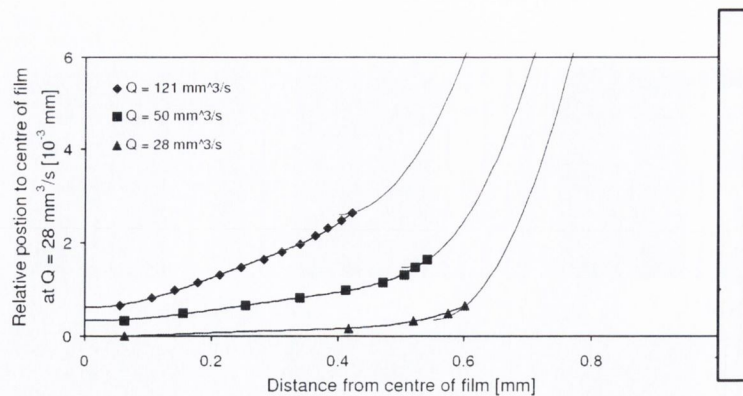
Figure 5.10: Profile of one half of the film interface shown in Fig. 5.9 for three different flow rates, calculated from the interference pattern using Equ. (5.1). All thicknesses are taken relative to the centre of the film at $Q = 28$ mm³s⁻¹. The data points are extended by arcs of circles presenting the Plateau borders. Their radii were obtained from the data presented in §4.2.2.1.

straighforward comparison with the investigations in §4.2.2.1. Image 1,2 and 4 were already used in Fig. 4.6 to illustrate the change of direction of the film flow. The black stripes of either side represent the Plateau borders, the bright stripe in the middle is the film.

We see that for low flow rates the film moves upward, producing quite regular vortices at the boundary to the Plateau borders (image 1, Fig. 5.9). As the flow rate is increased, the Plateau borders swell, forcing the film to become narrower. The interference pattern changes increasingly towards vertical, parallel stripes, marking the transition to downward flow in the film. In this particular geometry this transition occurs at a flow rate of about 25 mm³s⁻¹ (image 2, Fig. 5.9). The increasing number of interference fringes appearing upon increasing the flow rate emphasises that the interfaces become increasingly curved. Since the fringes are vertical and parallel over the whole vertical range of the film, we conclude that the film thickness does not change with vertical position. Counting the colour changes in the centre of the film whilst increasing the flow rate, we can furthermore conclude that the film thickness increases by approximately 2 μm between the onset of the laminar regime at $Q = 26$ mm³s⁻¹ and $Q = 120$ mm³s⁻¹.

Fig. 5.10 shows the profile of one half of the film interface for three different flow

rates, calculated using Equ. (5.1). All thicknesses are taken relative to the centre of the film at $Q = 28$ mm^{3}s^{-1}. The data points are extended by arcs of circles presenting the Plateau borders. Their radii were obtained from the data presented in §4.2.2.1.

5.6 Discussion

The observations made in this chapter generate a lot of questions. We focus on a small selection in the following discussion.

How can films move upward?

It seems counterintuitive that a liquid film subjected to gravity would move upwards. However, we have learnt by now that soap films are anything but ordinary objects (see §1.4). There are two important mechanisms at work in a soap film which can be brought forward as an argument. A third one might come into play for rigid interfaces.

1. *Marginal regeneration [84, 89]:* The pressure in a Plateau border is lower than the surrounding atmospheric pressure (interfaces are curved inward), whilst the pressure in the flat film is equal to the atmospheric pressure. This results in a pressure gradient, which sucks liquid from the film into the Plateau border. The film therefore thinnens in the vicinity of the Plateau border, the lower limit of its thickness being set by the *Common Black Film* [125] of approximately 30 nm. A locally thinned film surrounded by thicker film experiences an effective buoyancy force, causing it to rise in the film. Since these sections are very thin, they appear black in interference images.

   Fig. 5.11 shows very striking examples of marginal regeneration in sections of the Fairy film. These effects are only seen for the lowest flow rates considered here. They are much less striking in the case of SDS.

2. *Marangoni effect (see §1.4)* The flow in the film and Plateau borders generates surface tension gradients by locally diluting or accumulating surfactant molecules. This process generally occurs as a result of expanding and contracting films or by liquid flowing past an interface and thereby sweeping away the surfactant
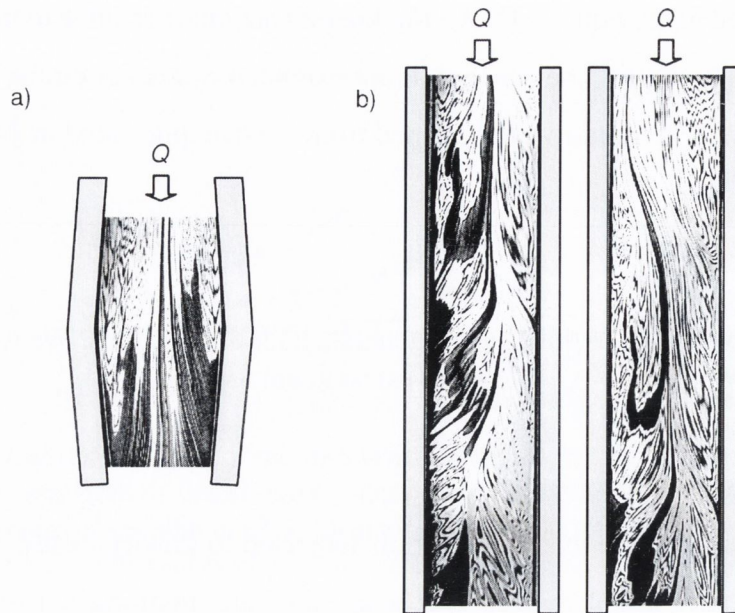
Figure 5.11: Striking examples of "Marginal Regeneration" in a "Fairy" soap film: The negative pressure in the Plateau borders sucks liquid out of the film, which leaves a thin (hence black) film behind. This thin film rises in the surrounding film as it is lighter. a) Example in a diamond shaped film. b) Examples in a long, narrow film.

molecules. As explained in §1.4, the resulting surface tension gradients generate movement of the interfaces and hence the thin film.

The details of the mechanism as it applies to the problems studied here are not clear and require a much more thorough investigation of different geometries and surfactants.

3. *Simple conservation of soap film?* If the interfaces are very rigid, like in the case of Fairy, it might be energetically quite "expensive" to destroy a film. Hence, the interfaces being dragged down along the Plateau borders might displace those in the middle of the bottom, which are then forced to move upward.

In order to understand the flow in soap films, it will be important to disentangle the various possible contributions of these effects.

The Crocodile Belly. What could the stationary film sections be?

The crocodile belly (Fig. 5.5) has only been observed with Fairy films. It looks like an island of very rigid film, of which bits and pieces literally break off at its boundaries.

We know that the various surfactant molecules used in Fairy make a very rigid interface. It may be a reasonable assumption that under certain conditions it might form very rigid islands. An important question arising from this assumption is whether the liquid between the two interfaces drains in a Poiseuille type flow. This question could be extended to many of the effects observed here. Since we deal with films of several micrometers thickness, one needs to ask whether it is still correct to assume that we can neglect flow variations along the film normal (lubrication approximation).

How could the film thickness variations be stabilised?

In the case of Fairy we have seen that large thickness variations of up to 4 μm are stabilised over a small region of a few mm^2. SDS has not displayed anything similar to this. A significant difference between the two surfactants is the existence of Polymers attached to the head groups of the fairy surfactant molecules. Polymers are know to have rather unusual flow properties, which could well be responsible for the observed phenomena.

How does this work relate to bigger, free-falling films?

The much bigger films (without Plateau borders) used by the hydrodynamics community display the well know Poiseuille profile flattened by the friction of the film with the surrounding air. Unlike in our case, the maximum flow velocities of several meters per second are obtained in the centre of the film, whilst they go to zero towards the frame [105].

We have seen in §4.2.1 that the maximum velocities ($\approx$ 0.5 ms^{-1}) achieved in our setup occur in the Plateau borders. Our film velocities are therefore significantly smaller than those studied by researchers like Rutgers et al. [105]. Since the principle idea of our experiments are very similar, but at different scales, it would be important to find out how they can be brought together in a model that combines both.

5.7 Conclusions and outlook

The observations made in this chapter generate a lot of interesting questions. They confirm that the rheology of soap films is very complex, in particular when surfactants

with complex rheological properties are involved.

The most important lesson to be learnt here is that the flow in soap films can either be upward or downward depending on the film geometry, its physico-chemical properties and the flow rate of the surfactant solution.

In order to proceed from here it will be important to establish a more quantitative approach to this matter. Modern technology [105] enables us to determine local flow velocities, film thicknesses and surfactant concentration to a high precision. These findings should be employed to establish phase diagrams for the flow properties of small films, taking into account the film geometry and the physico-chemical properties of the solution. In particular it will be important to study even smaller films - on the scale of a typical foam film.

It will be interesting to relate the findings of this chapter to the instability discussed in the previous chapter. Buckling instabilities of soap films at high film velocities have been observed at many occasions [105].

A very important step will be to employ the findings for individual soap films to the more complex scenario provided by foams. In particular, one needs to establish quantitative criteria below which it is justified to neglect the films by focusing on the Plateau border network only.

Not only does interface dynamics have an importnat effect on drainage in foams, but on the flow of foams as well. We refer to this in Part III.

Conclusions and outlook of Part II

This part of the thesis has investigated the properties of a simple system, namely that of fluid flowing through two surface Plateau borders connected by a thin film. We have seen that despite its simplicity, the system poses a variety of very complex problems due to the challenging dynamics of surfactant loaded interfaces. We believe that we have been able to point out a few general properties of such systems at high flow rates. A lot more thorough experimental investigations combined with computational and theoretical modelling need to be undertaken to establish a deeper understanding and quantifiable criteria.

In general, we have confirmed the significance of the interface mobility as an important parameter in the physics of foams.

We believe that for foam systems at low drainage velocities the traditional assumption of fixed Plateau border corners holds. For higher velocities, however, the film is being dragged along with the flow in the Plateau borders. We propose that this changes the geometry of the cross-section from the traditional picture of two Plateau borders connected by a thin, flat film (Fig. 5.12 a)) to one of two semi-merged Plateau borders connected by a liquid bridge (Fig. 5.12 b)). Even though the flow rate in the film itself is still negligibly small in comparison to the amount of liquid going through the Plateau borders (less than 1 %), it changes the boundary conditions and cross-section of the system, and hence the average velocity for a given flow rate. In this light it seems to make sense that the geometrical parameters determined in §4.2.2.1 are smaller than those predicted by the traditional picture. In Fig. 5.12 we have sketched our suggestion for the cross-section and velocity profile of narrow films between Plateau borders at high flow rates. For justification of the cross-section refer to Fig. 5.10. Within these
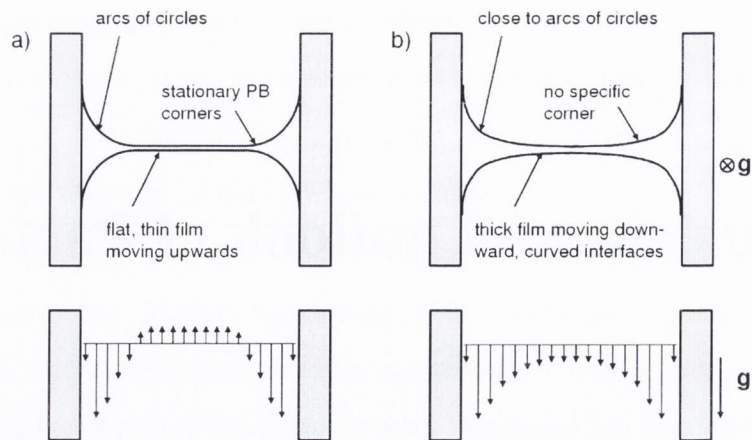
Figure 5.12: Cross-section and velocity profiles of a system of two surface Plateau borders connected by a film for a) low flow rates and b) high flow rates.

considerations it will be important to answer the question whether Plateau borders can still be approximated by arcs of circles at high flow rates.

As a result of these conclusions we suggest that in foams subjected to fast forced drainage, the contribution of the films has to be taken into account. This is mainly important regarding the flow boundary conditions in the Plateau borders, as even thick films of a few microns would only contribute a negligible part to the overall flow rate through the foam.

The physics of upward versus downward moving films and the relation of the turning point to the general physics of foams has to be understood. The interface mobilities at this point and the onset of the meandering instability seem to coincide with those marking the transition from rigid to mobile interfaces. Upon this transition, the flow resistance of a Plateau border is significantly reduced, which may result in the system becoming unstable to slight perturbations (private communication Arnaud Saint-Jalmes and Florence Elias). Effects of this nature may be related to convective instabilities in foams.

Our observations suggest that dynamice surface tension effects are important at hight drainage rates. In this light, it may be appropriate to re-introduce a second mobility parameter $N = \frac{\mu D_{eff}}{E r_{PB}}$, where D_{eff} is the effective surface diffusion coefficient and E the Gibbs elastic modulus of the surface [42].

Part III

Rheology
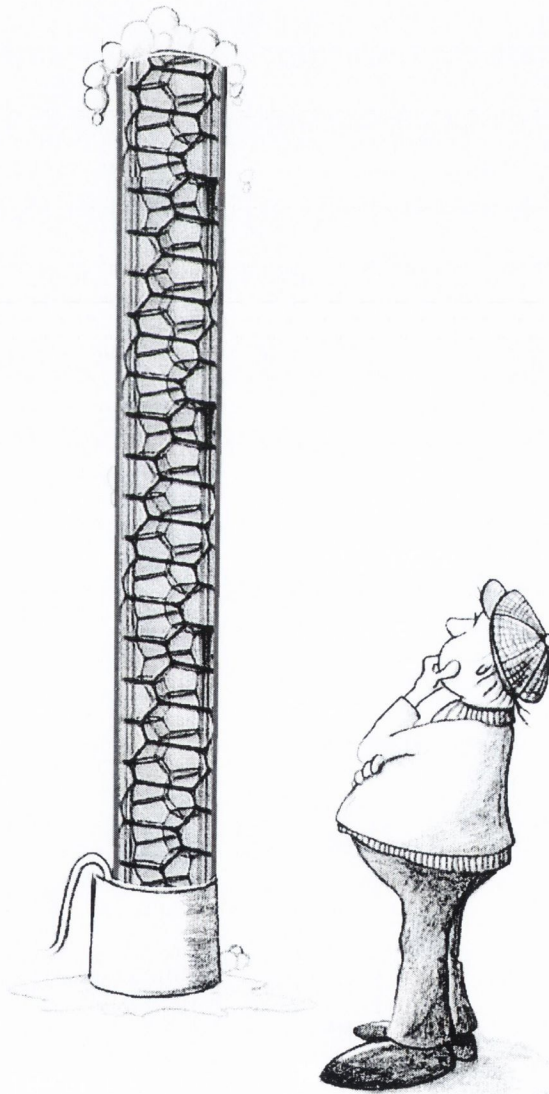
Chapter 6

Juggling bubbles - on the way to a Discrete Microfluidics

6.1 Introduction

Part II of this thesis dealt with the flow of liquid in the individual building blocks of a foam, namely Plateau borders and films. This is, however, only one of two major aspects of the dynamics of foams, as it generally leaves the structure of the foam unchanged (refer to §1.3).

In this part we focus on the second aspect, namely *foam rheology*, by considering simple model systems, which allow easy observation and comparison with computer simulations. This research elegantly combines highly applied and theoretical interests. Because the applicational side is very promising and has been the major driving force of this project, it will govern the approach and reasoning of the following chapters.

6.2 Motivation of this research

The handling of small quantities of liquids and gases has moved into the focus of various technological fields, ranging from pharmaceutical, medical and biological applications to printing. Today many of its challenges are met by quickly advancing microfluidic technologies [1, 2, 76, 120, 22, 23, 45], which utilise an assembly of micro-channels and detectors on small chips to manipulate liquids by various means. These *Total Analysis Systems* are at the verge of replacing traditional macro-sized labs by *Labs-on-a-Chip* [1, 83, 131], which contribute to an extraordinary downscaling of
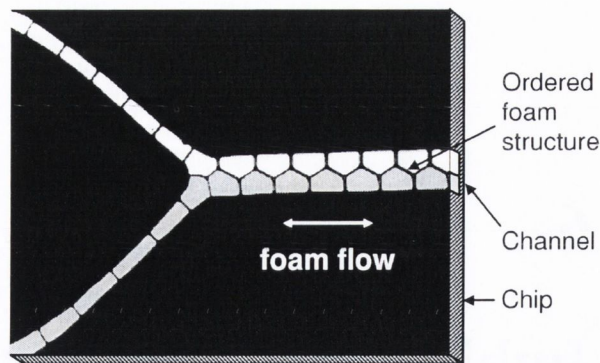
Figure 6.1: Example of the flow of ordered foam structures in a quasi-2D channel geometry. A Y-shaped channel can be used to split rows of bubbles.

space and financial requirements in a plethora of fields. However, even though the field of microfluidics has seen astonishing leaps in its development in recent years, important issues remain unsolved and have proven to be very difficult to tackle within the framework of traditional methods [2, 115].

New advances have been made in using individual droplets, rather than continuous liquids, for the purpose of controlled transport and mixing. This method of manipulation of discrete fluid samples has been termed *Digital Microfluidics* [91].

With our background in the physics of foams, we take the digital approach even further by utilising the manipulation of ordered foam or emulsion structures in specifically designed channel geometries. An illustrative example is shown in Fig. 6.1, where an ordered foam structure of two rows of samples is split into two separate individual rows in a Y-shaped channel on a chip.

The unique opportunity of sorting the discrete pockets of a two-phase system purely by moving the samples through specific channel geometries makes use of the most fundamental physical principle: minimisation of energy. The energy of a two-phase system is related to its interfacial area and therefore to its structure (refer to §1.2.1).

By trapping foams or emulsions in channels of purpose-designed shapes, we force specific boundary conditions upon the system and hence select particular sample arrangements. Upon moving through these channels, the sample structures will undergo well defined transitions, which can be utilised for sample manipulation in various ways

(see Chapter 7).

This novel method, which we have termed *Discrete Microfluidics* **??**, would have many advantages over current practice, of which some of the most striking are:

- Since the proposed technology is based on the minimisation of interfacial area, the samples can either be gaseous (foam) *or* liquid (emulsion) for the *same* channel geometry.

- If diffusion is prohibited, an indefinite number of *different* samples can be treated on the *same* chip.

- As most of the sample manipulation is based on pure geometry, the number of movable (and hence sensitive) parts on a chip can be greatly reduced.

- Due to the discrete nature of the method, sample manipulation becomes very reliable and quantifiable. Samples can be labeled and traced easily throughout the chip.

- The minimisation of interfacial area of a structure can be modelled more easily than the complex fluid dynamics of continuous (micro)fluidic processes. Hence, a major part of the channel design can be done by computer simulation, rather than expensive try and error procedures in the experiment (see §7.3) .

- A well-know problem of traditional microfluidics is an efficient link between the microchip, the micro-arrays (well plates) and sample storage. Our proposed technology unifies these in a straightforward way (see §8.3).

- If the sample material is chosen such that it makes up a small volume fraction of the two-phase system, the sample material can be greatly reduced whilst maintaining reasonably large channel sizes. This is particularly interesting for analysis methods requiring the application of beads, which would clock up small channels.

By arranging the various channel elements in a network that integrates means of sample generation, analysis and storage, we can design Total Analysis Systems in a

relatively straightforward manner. These may, for example, find use in the analysis of blood samples or environmental probes, or in the area of genotying.

Another exciting dimension of manipulation is added by using magnetic fluids and specifically designed magnetic fields (see §8.1 and §8.2) [60, 39].

In the remaining Part we give an overview of our recent investigations into several aspects of this concept of discrete microfluidics. We introduce a method of highly accurate bubble production (§8.1), the detection of bubbles in channels (§8.2) and sample storage (§8.3). Our main focus, however, lies on the introduction of the rheology of ordered two-phase structures in various channel geometries, guided by experiments and computer simulations (Chapter 7). At the outset we give a brief introduction to the physics of ordered foam structures (§6.3) and ferrofluids (§6.4).

All our investigations have been conducted on millimeter scale. It remains to be seen how easily the introduced principles can be applied to the length scales required by microfluidics. We do not expect this to pose major problems. For many potential applications it is not even necessary to go much below millimeter scale.

To reduce confusion and to take into account that most of our experiments have been conducted with foams rather than emulsions, we will only talk about *foams* and *bubbles* from now on. The reader should keep in mind, however, that everything said should similarly apply to *emulsions* and *droplets* [58].

6.3 Ordered foam structures

Due to their complex energy landscapes, foams are generally highly disordered. However, if bubbles of equal volume are introduced into regular containers of cross-sections of the order of a few bubble diameters, they order in a highly predictable manner [127, 94, 59, 60]. Fig. 6.2 shows photographs of some simple cases of these structures generated with foams and emulsions in cylindrical tubes. Their specific structure depends on the ratio δ of the tube diameter to the bubble or droplet diameter. They have been modelled very successfully in computer simulations using the Surface Evolver [16]. For the classification of these structures we use the (cylindrical) phyllotactic no-
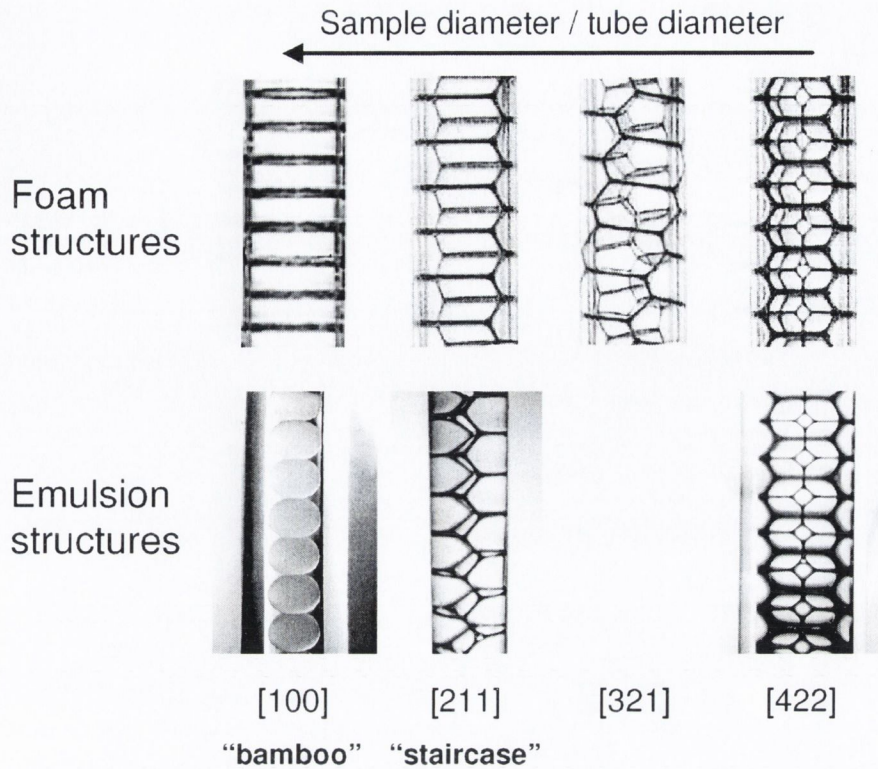
Figure 6.2: Ordered foam and emulsion structures in cylindrical tubes. Which type of structure is stable depends on the ratio of bubble/droplet diameter to tube diameter. The emulsion is silicone oil in water stabilised by "Fairy" (§1.5).

tation [i,j,k] of the hexagonal patterns formed on the surface of the container (refer to chapter 2 or [64]).

In two-dimensional systems these ordered structures reduce to i columns of bubbles, which we classify with the notation [i]. Fig. 6.3 shows an experiment of a series of highly localised transitions between consecutive structures of a mono-disperse foam continuously flowing through a wedge shaped, quasi-2D channel (transitions: [1] $\rightarrow$ [2] $\rightarrow$ [3] $\rightarrow$ [2] $\rightarrow$ [1]). More about the experimental set-up will be said in section §7.2. The image shows that there is a very strong hysteresis between the $[i] \rightarrow [i+1]$ and the $[i+1] \rightarrow [i]$ transition. At which channel width to bubble diameter ratio (δ) the transitions occur and how strong the hysteresis is, depends very much on the liquid fraction of the foam. The wetter the system is, the less hysteresis plays a role, as the foam can explore its energy space more easily. A similar system has been investigated for wet foams by Rosa and Fortes [100], ignoring the effects of hysteresis.
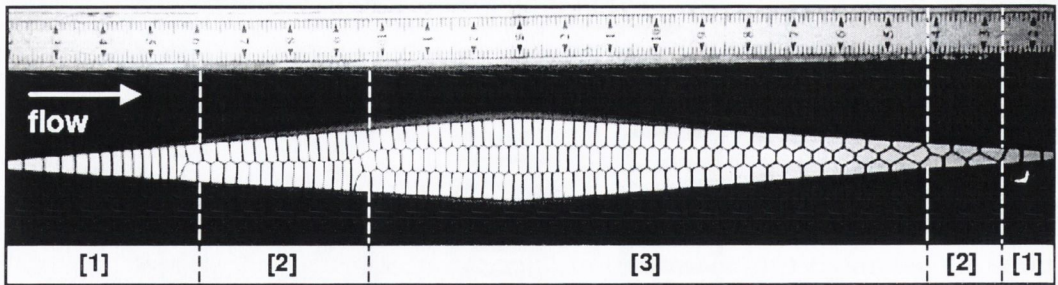
Figure 6.3: Transitions between ordered 2D foam structures as a result of foam flowing through a quasi-2D, wedge-shaped channel.
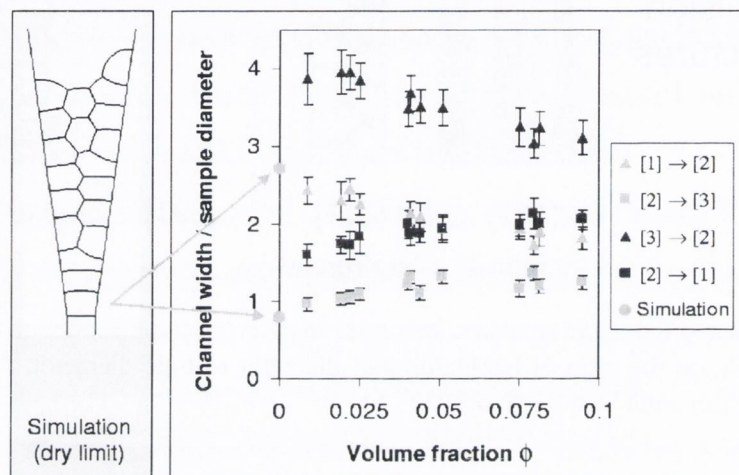
Figure 6.4: Experimental data showing δ as a function of liquid fraction for the wedge shaped quasi-2D channel displayed in Fig. 6.3. Computer simulations (by N. Kern) for the perfectly dry foam fit in very well with the data.

Fig. 6.4 comprises experimental data of δ for the first two transitions as a function of liquid fraction for the wedge shown in Fig. 6.3. Computer simulations for the dry limit ($\phi = 0$), undertaken by Norbert Kern using the Surface Evolver [16], fit in very well with the experimental data.

For a successful application of discrete microfluidics a thorough understanding of these transitions will be crucial. In order to manipulate and analyse samples and sample structures in networks of channels, it will be very important to predict and control the type of structure present at any point in the network. This is the case because some of the elements, which we introduce in Chapter 7, employ well controlled transitions to

perform specific sample operations.

6.4   Introduction to ferrofluids and ferrofuid foams

Ferrofluids are stable colloidal dispersions of solid, magnetic, single domain particles suspended in a liquid carrier. A typical ferrofluid contains 10^{23} particles of typically $3 - 15$ nm size per cubic meter . There are two main groups of ferrofluids, which are either *water based* or *oil based*. In order to prevent agglomeration (as a result of magnetic and van der Waals interaction), the particles are coated with long chain molecules generating a steric repulsion. Water based ferrofluids are generally of ionic nature, generating an additional electrostatic repulsion between the equally charged particles (Fig. 6.5 a)) .

At room temperature the magnetic moments of the particles are randomly oriented, which results in a zero net magnetisation of the ferrofluid (Fig. 6.5 a)). Upon the application of a magnetic field, thermal agitation competes with magnetic energy to produce an overall paramagnetic response (Fig. 6.5 b) and c)). Ferrofluids are of *superparamagnetic* type, as the small size of the magnetic particles leads to paramagnetic behaviour well below the Curie temperature of their bulk material.

Fig. 6.5 c) shows the general response of a ferrofluid to an external magnetic field. At low magnetic field strength, the magnetisation increases linearly, its slope providing the magnetic susceptibility χ of the suspension. Upon increasing the external field the magnetisation saturates at a value M_S.

In order to make ferrofluid foams, we simply replace the ordinary soap solution by a water based, ionic ferrofluid. The ferrofluid already contains SDS as a surfactant molecule to stabilise the suspension. We usually increase the SDS concentration in order to make sure that we work well above the CMC of the solution.

If ferrofluids of low susceptibility are used, the structural and hydrodynamic properties of the foam remain unchanged upon the application of magnetic fields. For high susceptibilities, however, particular care needs to be taken as strong magnetic dipole interaction leads to various effects influencing the viscosity of the solution and the
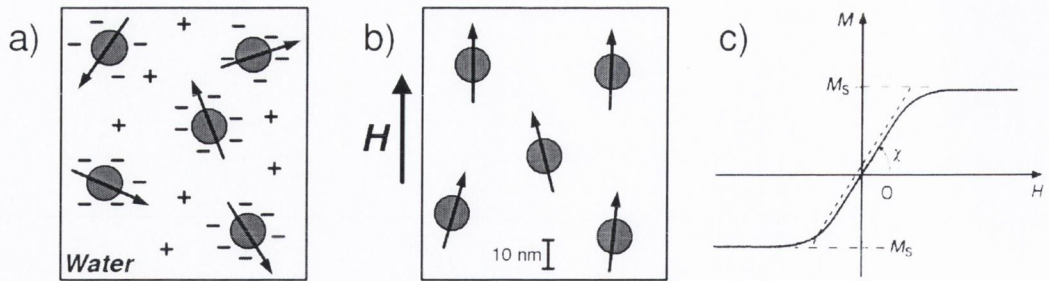
Figure 6.5: Ferrofluids are suspensions of nano-metre sized magnetic dipoles in a liquid carrier. a) At room temperature and zero applied magnetic field the net magnetisation of a ferrofluid is zero. b) Upon the application of a magnetic field, the dipoles align to give an overall paramagnetic response, which is sketched in c). χ is the magnetic susceptibility, M_s is the saturation magnetisation.

structural properties of the foam [62].

Initial work on the application of ferrofluid foams has been conducted by Hutzler et al. [60], who used magnetic field gradients to manipulate ordered ferrofluid foam structures. The research introduced in this thesis extends their work with the generation (§8.1) and detection (§8.2) of ferrofluid bubbles.

Chapter 7

Rheology of ordered foams

7.1 Introduction

We have shown in §6.3 that the structure of an ordered foam is determined by its confining geometry. Hence, by designing channels or containers of particular geometries, we cannot only control the structure of the foam, but we can use it to perform "logic operations" on the bubbles as the structure flows through these channel elements.

In the following sections we give a brief overview of our experimental procedure and the basics of our computational modelling. Even though the simulations have been entirely conducted by S. J. Cox or G. Delaney, they have been developed in very close collaboration and form an integral part of the motivation and outcome of this project. They therefore receive some consideration in this thesis.

Subsequently we demonstrate in a few striking examples how experiment and simulation can be combined very efficiently to purpose-design "building blocks" for a more complex network of channel geometries performing specific tasks of bubble manipulation.

7.2 Experimental set-up and procedure

Most of our experiments were conducted with aqueous foams on millimeter scale. Adaptation to emulsions should be straightforward [58]. It remains to be seen how the downscaling to micro-fluidic length scales affects the properties of our designs. Apart from the fact that micro-structures will be very wet due to the strong capillary
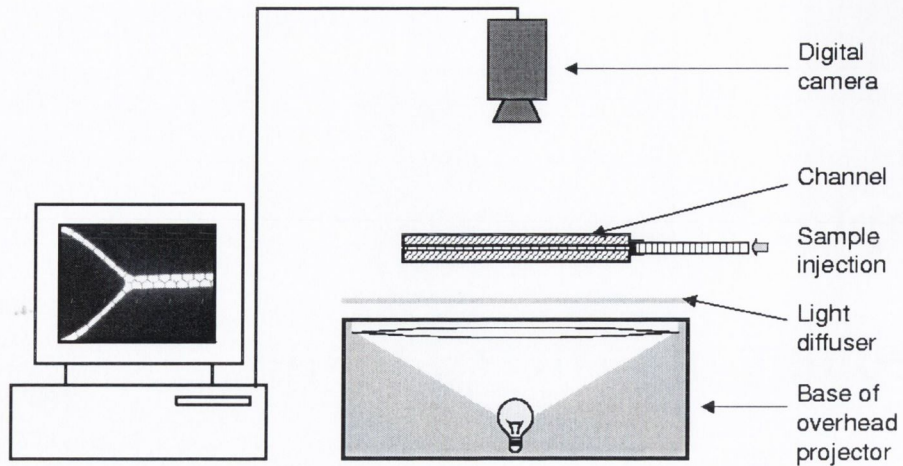
Figure 7.1: Setup for 2D-foam rheology: The channels were carved into a Plexiglas sheet, which was then glued onto another plain Plexiglas sheet. Monodisperse bubbles were injected into the horizontal channel system from a capillary by applying a constant (nitrogen gas) pressure. The system was lit from below with an overhead projector topped with a light diffusing sheet. Images and videos were recorded with a digital camera from above and consequently analysed on the computer using ImageJ [61].

forces and that much higher pressures/forces will be required to drive the structures in the channels, we do not expect significant changes in the general principles demonstrated here. Initial experiments on ordered microemulsions by Seemann et al. (private communication) have been very successfull.

We worked with quasi-2D systems of typically $0.5 - 1.5$ mm channel depth. For exploratory investigations these channels were created using a simple system of a rubber sheet sandwiched between two glass plates. Channels of arbitrary shape can easily be cut into the rubber sheet.

For more quantitative investigations, we designed the channel geometries in Autocad. These were carved into a Plexiglas sheet, which was glued onto a plain Plexiglas sheet in order to close the channel.

Bubbles of equal volume were generated by injecting nitrogen gas (low diffusivity) into Fairy dishwashing solution of 0.4 % concentration (as in all the experiments before). They were collected in a capillary, which was attached to the channel system. The foam structure was then driven through the system by applying a constant gas pressure at the inlet. For a sketch of the set-up see Fig. 7.1.

The quasi-2D setup has several advantages. Not only does it significantly simplify the observation, analysis and modelling, but it is more straightforward to manufacture. In any case, we believe that this will be the way to go for industrial applications, as most channel systems are generated by lithographic or stamping techniques, which will be significantly simpler for channels with rectangular cross-sections.

Images were recorded with a digital camera. Best image quality was achieved by placing the horizontal, transparent channel system between a diffusive light source and the camera. Due to the curved nature of the interfaces the films and vertex boundaries appear black in the images.

The reader should keep in mind that surface Plateau borders are formed wherever films are attached to the channel walls. This does not only have an effect on the apparent film thickness, but on the flow properties of the foam. It is a 3D-effect and can be neglected for most of the cases considered here. For higher flow velocities, however, it has to be taken into account (see §7.5).

7.3 Computational modelling

Computer simulations are vital for the efficient design of channel systems and to test our physical models of foams and foam flow. For the purpose of modelling flow in flat channels it is sufficient to apply 2D-simulation.

Simplification can be taken further without losing significant physics by modelling perfectly dry foams. In such a system films are represented by lines (edges) and vertices by the points, where these edges meet. The wetness of the foam can then be accounted for by adjusting the critical edge length at which neighbour switching processes occur (refer to §1.3.2 and Fig. 1.5). The wetter the foam, the longer this critical length is going to be.

For reasonably low flow velocities we can assume quasi-static flow, whereby simulations proceed by a process of small increments in position and energy minimization, allowing the foam structure to move via a sequence of equilibrium states. This can be done with the software package Surface Evolver developed by Ken Brakke [16]. The required 2D foam structure is pushed in this way through the channel boundaries. Af-
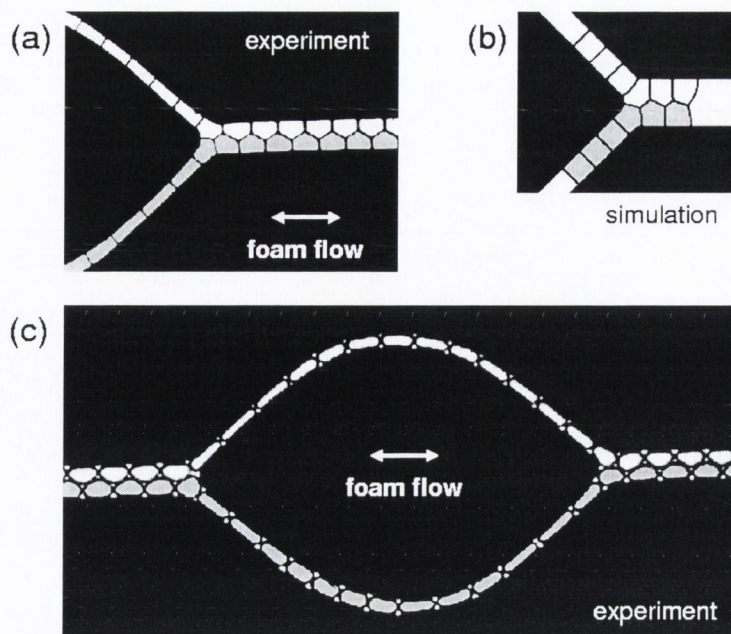
Figure 7.2: The Y-junction. a) Experiment and b) simulation of a channel geometry which divides a structure of two rows of bubbles into two structures containing one row of bubbles each. The reversibility of this process is demonstrated in c).

ter each step the total line length (energy) of the system is minimised, whilst keeping the bubble volumes constant.

For small flow velocities this procedure has proven very successful in reproducing the experimental observations. For higher velocities, however, viscous drag acting on the surface Plateau borders has to be taken into account. The magnitude of the critical velocity at which the *quasi-static* approach breaks down and the flow is dominated by *viscous* forces, depends on various parameters, of which the most important are the liquid fraction and the channel depth. Much of the work reported in section §7.5 attempts to explore this dependence.

7.4   Examples of network elements

7.4.1   The Y-junction

Branching channels can be used to sort bubbles into different parts of a network or to (re)combine them. The ratio of the channel widths of the branches determines the "sorting algorithm". A striking example is shown in Fig. 7.2, where one channel
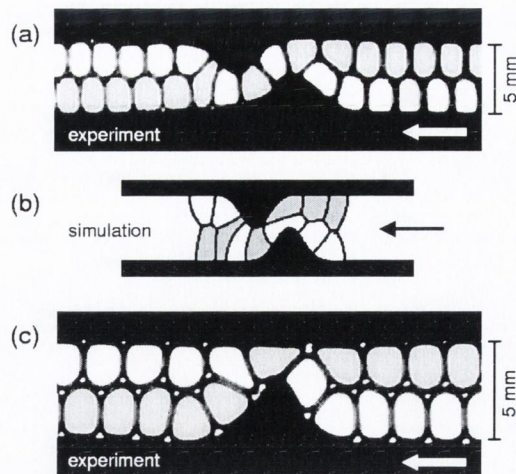
Figure 7.3: The Flipper. a) Two or b) one "Gaussian bumps" in a channel can be used to provoke controlled $[2] \rightarrow [1] \rightarrow [2]$ transitions, which result in a re-sorting of the bubbles such that the two rows of bubbles are switched withing a single channel. b) is a computer simulation of the experiment shown in a).

containing two rows of bubbles is split into two channels containing one row of bubbles each. Fig. 7.2 b) shows an image of a computer simulation for this device. Note the incredible similarity between simulation and experiment.

These processes are perfectly reliable and reversible. The reversibility is shown in Fig. 7.2 c). Here a double row of bubbles is split into two individual ones, which are then brought together again to form the same double row structure. This type of channel could furthermore be used to introduce a phase shift between the two rows of bubbles by choosing an appropriate length difference between the two separate branches.

7.4.2 The flipper

Specifically designed local narrowings or bulges in a channel can make use of consecutive transitions between structures to re-sort bubbles within a single channel. Fig. 7.3 shows experiments and simulations of two typical examples in which one or two "Gaussian bumps" cause a $[2] \rightarrow [1] \rightarrow [2]$ transition during which the bubbles are resorted such that the two columns of bubbles switch sides in the channel.

Care has to be taken, however, about the initial configuration of the double-row structure. When the foam flow is set up, one of the bubble rows will be advancing the other by one bubble at the very beginning of the foam structure. Depending on which
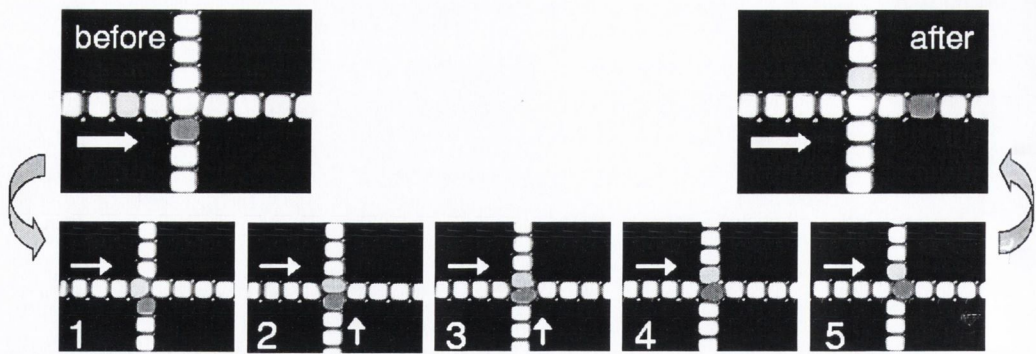
Figure 7.4: The magic cross. Two crossing channels contain a single row of bubble each. The bubbles in the horizontal channel flow continuously. Upon the application of an appropriate pressure pulse in the vertical channel, a bubble from the horizontal channel (light gray) can by replaced with a bubble (dark gray) from the vertical channel.

row this is, the channel element will or will not switch them. More thought will have to go into a design that will work independently of this initial condition.

7.4.3   The magic cross

Bubbles can easily be added to, removed from or replaced in a structure using T-junctions or crosses of channels with individually controlled flow/pressure.

An example of a very versatile device is demonstrated in Fig. 7.4. Two crossing channels contain a single row of bubbles each. The main flow occurs in the horizontal channel from left to right. If the top vertical branch is closed (equivalent to T-junction), appropriate pressure pulses or pressure drops applied to the bottom branch result in the controlled injection or removal of bubbles from the main channel. If the top branch is open, which is the example shown in Fig. 7.4, a well timed pressure pulse results in a bubble from the main channel (light gray) being replaced by a bubble from the crossing channel (dark gray).

Devices of this type could be very useful to inject tracer bubbles in a network, or to remove "bad" bubbles which failed a test at a detector. Most of all, it could be used to construct specific sequences of bubbles containing different chemical substances. A controlled breaking of films between them at a later stage could provoke chemical reactions or simply the mixing of minute quantities of gases (or liquids).
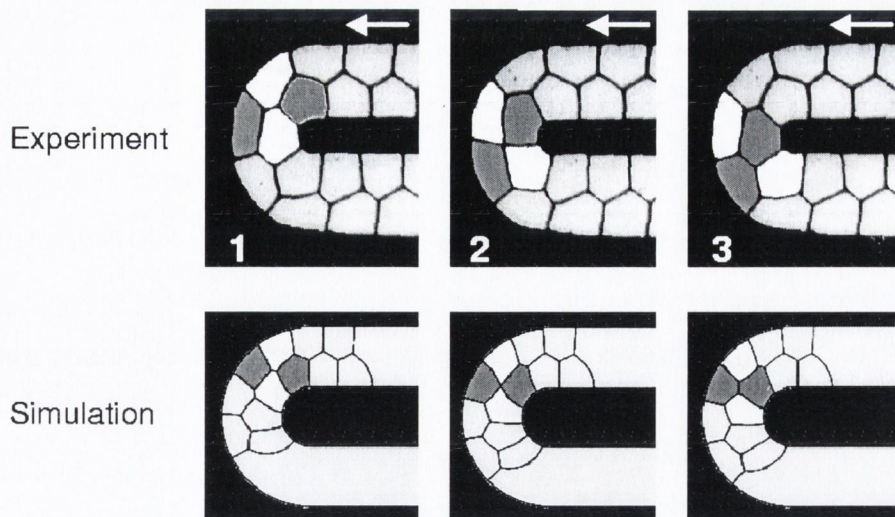
Figure 7.5: Around the bend. a) Experiment and b) computer simulation of a neighbour switching process (§1.3.2) trapped in a foam structure flowing around a narrow bend. This generates a phase shift of one bubble between the two bubble rows.

7.4.4 Around the bend

The flow around a narrow bend induces a localised shear on the structure, which can be used to induce one or more controlled neighbour switching processes (§1.3.2). If applied continuously, this results in an effective phase shift of the bubble rows.

Fig. 7.5 demonstrates an example in which one neighbour switching process is trapped in a 180° bend, which induces a phase shift of one bubble between two rows of bubbles. The same is possible with more than one, say n, T1-processes trapped in the bend, which results in a phase shift of n units between the bubbles.

Unlike in the other cases it is not sufficient to employ quasi-static models for a full understanding of the functioning of this device. Once a neighbour switching process has occurred in the bend, it can be modeled quasi-statically. The initial switching process, however, is triggered by the local shear of the sample structure, which is induced by the viscous drag on the walls and hence depends on the flow velocity. In order to tackle this problem we have developed a simple but powerful model, which has proven highly successful in reproducing experimental observations. In this context we revisit the bend in §7.5, giving a more extensive overview of the physics of this device and the related modelling.

7.5   The viscous froth

7.5.1   Introduction

In order to meet the industrial requirements of high sample throughput on a Lab-on-a-Chip, it will be important to consider the effect of high flow velocities on the methods introduced in the previous sections.

As we go down to smaller length scales, effects related to the channel walls will become increasingly important with respect to bulk effects. At high flow velocities, one of the most dominant contributions is expected from the viscous dissipation of the surface Plateau borders sliding along the channel walls. Questions related to this problem are very much at the core of current research activities in foam and emulsion rheology [75, 135, 19, 65]. It is not yet clear, what exactly the main dissipation mechanism is and how it is related to the physical properties of the bulk and interfaces. Despite these uncertainties, however, researchers have been able to show that the various contributions to the dissipation can be combined to a good approximation in one single drag coefficient λ. This coefficient is defined such that it relates the drag force on a point of a surface Plateau border sliding along a wall to a power of the normal velocity $v_\perp$ at this point [17, 19, 20]:

$$\boldsymbol{F}^*_{visc} = -\lambda\, \boldsymbol{v}^\alpha_\perp, \tag{7.1}$$

where $\boldsymbol{F}^*_{visc}$ is the viscous force on a line. The units of λ depend on the exponent α.

The interplay between the pre-factor λ and the exponent α is not yet clear as it involves a better understanding of the detailed hydrodynamics and interface dynamics involved [17, 110, 98, 133, 134, 57, 20]. Traditional experiments of the flow of individual bubbles in tubes established $\alpha = 2/3$ [17], which was confirmed by more recent work on quasi-2D foam flow by Cantat et al. [20]. Current research seems to assign α a range of values between 1/2 and 2/3, supposedly depending on the mobility of the interfaces of the foam [36, 35].

We incorporate this local friction force in our 2D-modelling by adding the velocity-dependent term (7.1) to the Laplace Equ. (1.2). The force balance acting locally at each

point of the soap film therefore becomes

$$\Delta p = 2\gamma\,\kappa - \lambda\,v_\perp^\alpha. \tag{7.2}$$

This relationship has already been established in the context of domain growth [54, 127]. The application to 2D foam flows turns it into the so-called *Viscous Froth Model*, introduced by Weaire et al. [128].

For an enormous simplification in the analysis and the numerical modelling we set $\alpha = 1$ [69]. We believe that this should leave the essential behaviour of the investigated systems largely unchanged. Detailed comparison between experiment and simulation will have to shed light on the fact whether this approximation is justified.

7.5.2   Example of the viscous froth: foam flow around a bend

We illustrate the strength of the Viscous Froth Model by applying it to foam flow around the tight bend introduced in §7.4.4.

For small flow velocities v, and hence in the quasi-static limit, the foam structure looks as shown on the left in Fig. 7.6. It flows around the bend without undergoing any topological changes. Upon increase of v, the viscous forces of the films being dragged along the top and bottom plate become of the order of magnitude of the surface tension force. Since the local velocity - and hence the viscous force - increases towards the outer boundary of the bend, a shear stress is imposed on the foam structure within the bend. For sufficiently high flow velocities this leads to a clearly visible distortion of the structure, as can be seen in Fig. 7.6. Simulations applying the Viscous Froth Model reproduce this distortion very well (bottom row of Fig. 7.6).

At a critical velocity v_c the shortest edge at the bottom of the bend flips to give a T1 (§1.3.2). Before this neighbour switching process sets in, all cells have 4 interior edges. Upon the flipping of the edge two pairs of 7- and 3-sided cells are generated, of which one pair follows the foam flow and leaves the bend. The other one moves into the bend to release the strain. This new topology generates a succession of neigbour switching processes for all the following bubbles (refer to Fig. 7.5).

As said in §7.4.4, this effectively shifts the two columns of bubbles with respect
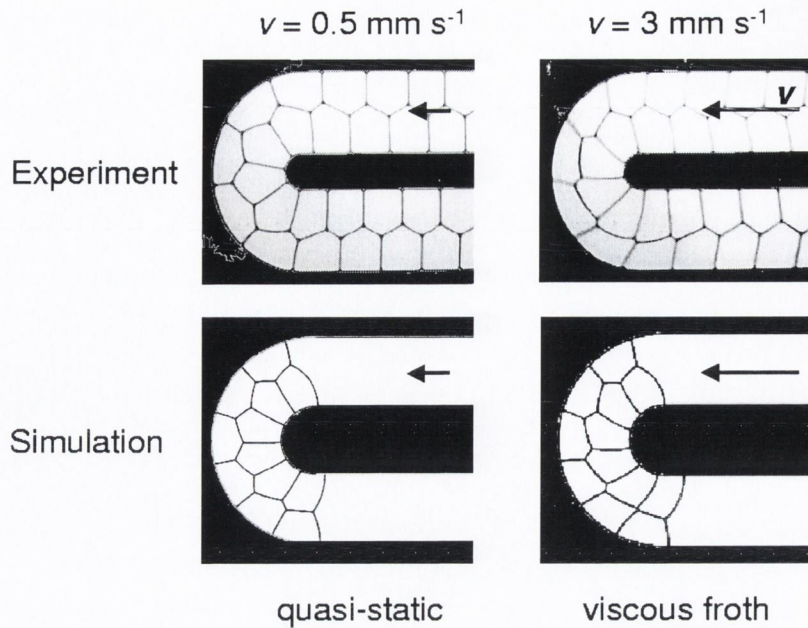
Figure 7.6: Comparison of the distortion of a foam structure going around a bend

to each other by one bubble. For even higher velocities, the structure will again be increasingly strained until another edge flips to give a second T1. This can be driven even further, with n T1 processes resulting in a phase shift of n bubbles between the two rows of bubbles.

Having the Viscous Froth Model at hand, we can make a range of predictions about the behaviour of the system as a function of various parameters, which can then be tested experimentally. One of the key quantities of interest in this problem is the critical velocity v_c as a function of various system parameters (e.g. bubble area, channel width and radius, liquid fraction, etc.). Simulations by S. Cox and G. Delaney [69] predict v_c to be inversely proportional to the bubble area for a perfectly dry foam.

The direct measurement of critical velocities of this nature in an experiment, however, are subject to significant errors. We therefore measure how the minimum length L of the critical edge (see Fig. 7.7) changes with the foam velocity v. We do this by very slowly increasing v to provide quasi-steady conditions. By doing this we cannot only extrapolate v_c, but also determine the drag coefficient λ by fitting the numerical prediction to the experimental data. This is possible, because λ acts like a scaling parameter for the velocity in Equ. (7.2). Hence, by setting $\lambda_{\text{sim}} = 1$ in the simulation
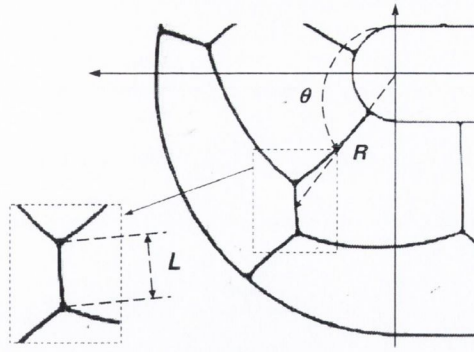
Figure 7.7: We measure the shortest edge length L as a function of foam flow velocity v (figure 7.8). If this edge gets short enough, a T1 occurs.

whilst using the proper physical parameters for the other quantities, we can fit L_{sim} to L_{exp} using λ as the fitting parameter. We do this by fitting the simulational data to the function

$$L_{sim} = a\, v_{sim}^{c} + b \tag{7.3}$$

via a,b and c. This function has no physical meaning, but fits the data very well. We then fit

$$L_{exp} = a(2\lambda\, v_{exp})^{c} + b \tag{7.4}$$

via λ, using a, b and c from Equ. (7.3). The factor 2 is included because friction occurs at the top and the bottom plate in the experiment.

The implementation of the surface tension in the model requires some more thought: In two dimensions, surface tension (γ_{3D}) becomes a line tension (γ_{2D}). An edge of length L in our experiment has an area $A = LD$, where D is the depth of the channel. Since surface tension is defined as change of energy E with change of area A, we can write

$$\gamma_{3D} = \frac{dE}{dA} = \frac{dE}{dL}\frac{dL}{dA} = \gamma_{2D}\frac{1}{D} \quad \rightarrow \quad \gamma_{2D} = D\,\gamma_{3D}. \tag{7.5}$$

Therefore, in order to obtain the line tension of an edge in our system, we have to multiply the surface tension by the depth of the channel. The obtained value is then used in the simulations.

Fig. 7.8 shows a striking example for a very dry foam in a bend of 0.5 mm channel depth, 7 mm channel width and 1.5 mm inner radius of the bend. For this particular
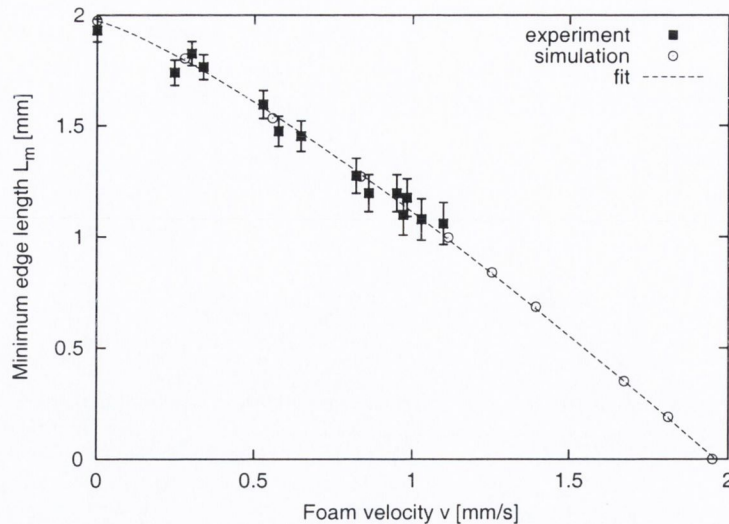
Figure 7.8: Experimental data showing how the minimum edge length L, shown in figure 7.7, varies with foam flow velocity v. Data from computer simulations (by G. Delaney) implementing the Viscous Froth Model is fitted using λ as fitting parameter.

setup and liquid fraction ($\phi \approx 1\%$) we obtain $v_c \approx 1.9$ mm s^{-1} and $\lambda = 15$ Nsm^{-2}.

Sequences of experimental data from this experiment can only explore a fairly short range of velocities for two main reasons:

- The velocities have to be increased very slowly to provide quasi-static flow conditions (see §7.5.3).

- The liquid fraction of the foam structure changes during the experiment as a result of the foam flow and the applied pressure. This is a real problem, as λ depends on the liquid fraction ϕ. In the future we will have to fit L as a function of v and ϕ.

We have done this experiment for very dry foams. Future work will aim at establishing a relationship between λ and a properly defined 2D liquid fraction.

Despite the excellent agreement between experiment and simulation, there are some important aspects arising from this work which deserve more attention in the attempt of testing the potential and limitations of the Viscous Froth Model. We will briefly illustrate the most important ones in the next sections.

(a) (b)
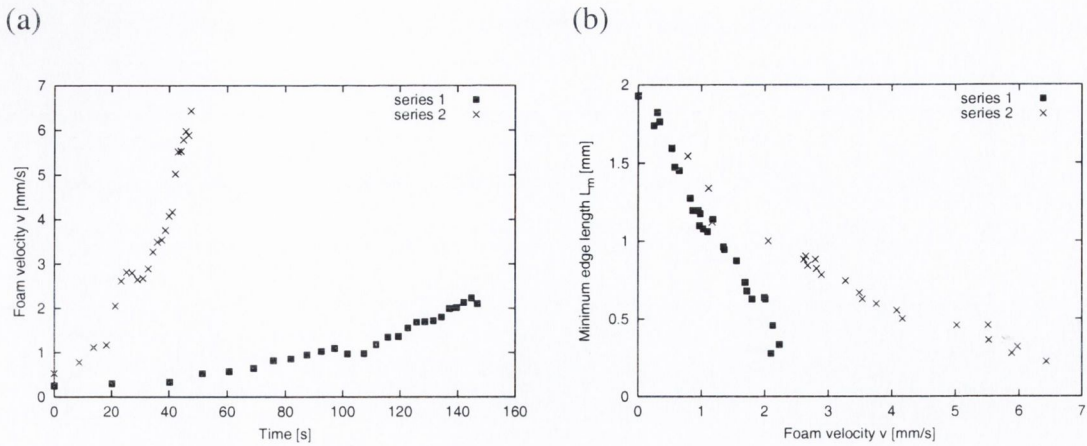
Figure 7.9: Effect of the long relaxation times in a quasi-2D geometry: The variation of L with foam flow velocity v depends significantly on how quickly the foam is accelerated.

7.5.3 Relaxation times

Viscous dissipation has a significant influence on how long it takes a 2D-foam to equilibrate. In order to provide quasi-steady conditions in experiments, it will be important to understand the magnitudes of the various times scales involved.

Fig. 7.9 shows a striking example of how measurements of the edge length L (introduced in the previous section) are influenced, if the foam flow velocity v is increased to quickly. In series 2 v was increased more rapidly than in series 1, leading to significantly longer L for the same velocity. We assign this to the fact that the the foam was accelerated more quickly than it could equilibrate. Hence, we deal with "out of equilibrium processes", which are far more difficult to model and should be avoided at this stage.

7.5.4 Rules of Equilibrium with the Viscous Froth Model

Considering that for the description of a viscous foam a local friction force is added to the Laplace Equ. (1.2), it is obvious that the first rule of equilibrium (edges are arcs of circle, §1.2.2) is not obeyed by a viscous, flowing foam.

The second rule of equilibrium concerning the angles at vertices, however, is still obeyed. To see this, consider a small control area around a vertex which is subjected to the pressure, surface tension and drag forces imposed by the edges. If we now make
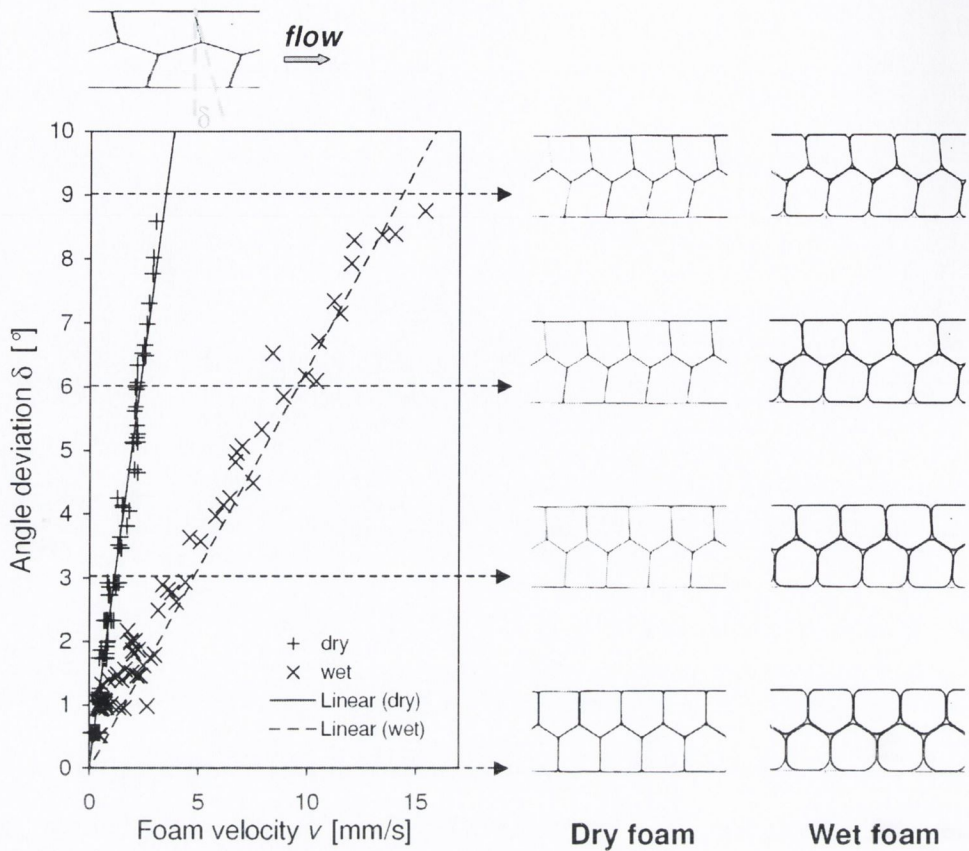
Figure 7.10: The angles between films and channel walls deviate notably from the predicted 90°. This deviation δ increases very linearly with the foam flow velocity v. The slope depends significantly on the liquid fraction of the foam.

the control volume infinitely small, only the surface tension forces remain. As they are equal for every edge, the angles between the edges must be equal, which gives 120° for interior vertices and 90° for vertices at the wall. The model would therefore not predict a difference between a quasi-static and a viscous froth vertex.

In the experiments we observe something very different. The most striking deviation concerns the angles of vertices at the wall, which differ notably from 90° even for low foam flow velocities. The drier the foam, the more evident this becomes. Fig. 7.10 illustrates this effect for the same structure ([2]) with two different liquid fractions, which we have not quantified for the reasons expressed in §1.2.2. The measurements are taken for the same channel cross-section (0.5 mm × 7 mm) and material used for the U-bend in §7.4.4. They seem to suggest a linear relationship between the angle deviation δ and the flow velocity of the foam, the slope depending on the liquid fraction.
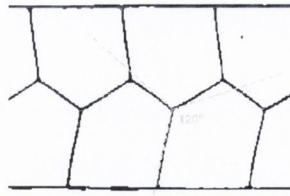
Figure 7.11: For high flow velocities the interior angles of a 2D foam seem to deviate from the predicted 120°. Example: Plexiglas channel, width: 7 mm, depth: 0.5 mm, flow velocity $v = 15$ mm/s.

For the highest velocities considered here, it furthermore seems that the interior angles deviate from the expected 120°. For an example see Fig. 7.11. The word "seems" is used in this context because the precise angles at the vertex are very difficult to determine due to the curved nature of the edges.

Possible explanations of these effects are still rather vague and will require rigorous testing. Two very different reasons may be considered possible candidates:

1. Tangential dissipative forces: In the present model, only normal forces acting on the edges are taken into account. Recent work by Cantat et al. [20] confirms that this is indeed a good approximation for dry foams at low foam flow velocities. At higher velocities however, the liquid transport along the Plateau borders might contribute to a *tangential* viscous force. Unlike the normal force, this would have an effect on the angles at vertices, as it acts parallel to the surface tension force.

2. Marangoni effect: Bubbles being dragged between two plates or rising in a liquid are known to experience a redistribution of surfactant molecules from the front to the back as a result of the viscous drag along the gas/liquid interface (refer to §1.4). This results in a local variation of surface tension and hence a surface flow (Marangoni effect) directed opposite to the drag, which increases the total drag on the object. In case of the vertices this effect might lead to differences of the surface tension of the edges or the wetting film along the wall. This in turn would lead to non-equal angles.

Guidance in the exploration of the true nature of these effects may come from extensive research carried out on the motion of bubbles and bubble trains in tubes of various cross-sections [17, 110, 98, 133, 134, 57].

7.5.5   Conclusions and Outlook

Using the simple experimental setup of an ordered, quasi-two-dimensional foam struc-
ture flowing around a tight bend, we have been able for the first time to qualitatively
and *quantitatively* test the predictive strength of the Viscous Froth Model. Even though
these investigations are very much at the beginning, we believe that the provided results
already demonstrate the success of the Viscous Froth Model. Despite its simplicity, we
find excellent agreement between experiments and simulations to the extent, that we
can employ them to extract physical parameters like the viscous drag coefficient λ of a
foam film sliding along a surface. It remains to be seen how this λ compares to similar
experiments like those of Cantat et al. [20], keeping in mind that we have chosen $\alpha = 1$
in Equ. (7.2).

Above all, it will be important to understand the detailed nature of the dissipation
mechanism, in particular the role of the bulk versus interface properties and the liq-
uid fraction ϕ. Fortunately, modern research provides us with a vast range of liquids,
surfactants and polymers to use as building blocks for thorough investigations of the
individual parameters of interest. In this process it will be equally important to es-
tablish values for the exponent α in Equ. (7.2). The quantification of an appropriate
2D liquid fraction and its measurement, however, is still an open problem (see §1.2.2),
which needs to be addressed in this process.

Understanding the precise interplay between λ and the various relevant system
parameters should enable us to fully purpose-design channel elements on the computer
using the Viscous Froth Model. For this and other purposes it will be necessary to
establish quantitative criteria of the various approximations that can be applied in the
modelling of the foam flow. The key parameter for this distinction is likely to be the
capillary number $Ca = \frac{\eta v}{\gamma}$, which characterises the ratio of the viscous to the surface
tension forces.

We have demonstrated some effects which cannot be accounted for within the Vis-
cous Froth Model. It will be important to understand their significance in order to de-
cide under which conditions they can be neglected or how they could be implemented
into the existing model.

Further questions arise regarding the dissipation of the T1 process itself. If a continuous pressure is applied to drive the foam through the channel, small pressure jumps should occur upon a T1. Their magnitude would give information about the amount of energy dissipated in a T1 process. This might be the first step into investigating the bulk dissipation in a foam.

Chapter 8

Bubble generation, detection and storage

8.1 Bubble Generation

8.1.1 Introduction

In order to control the type of foam structure present in a particular channel geometry, it is necessary to fine-tune the bubble volume. Bubbles are generally generated by injecting gas into a liquid at constant gas flux. The nozzle radius r and liquid density ρ_l control the critical bubble diameter D_c at which a bubble detaches from the nozzle for low gas flux Q_g [46]:

$$D_s \sim \left(\frac{\gamma r}{\rho_l g}\right)^{\frac{1}{3}}. \tag{8.1}$$

For higher gas discharge, the bubble surface expands so quickly that the dynamic surface tension (§1.4) has to be taken into account, which results in bigger bubble volumes. For very high Q_g the bubble volume is determined by the viscosity η_l of the liquid, rather than the surface tension [46]:

$$D_c \sim \left(\frac{Q_g \eta_l}{\rho_l g}\right)^{1/4}. \tag{8.2}$$

Adjusting the gas flow rate seems therefore a good parameter to set the desired bubble volume. Unfortunately, if the nozzle size is fixed, this method produces highly monodisperse bubbles only over a fairly small range of volumes.
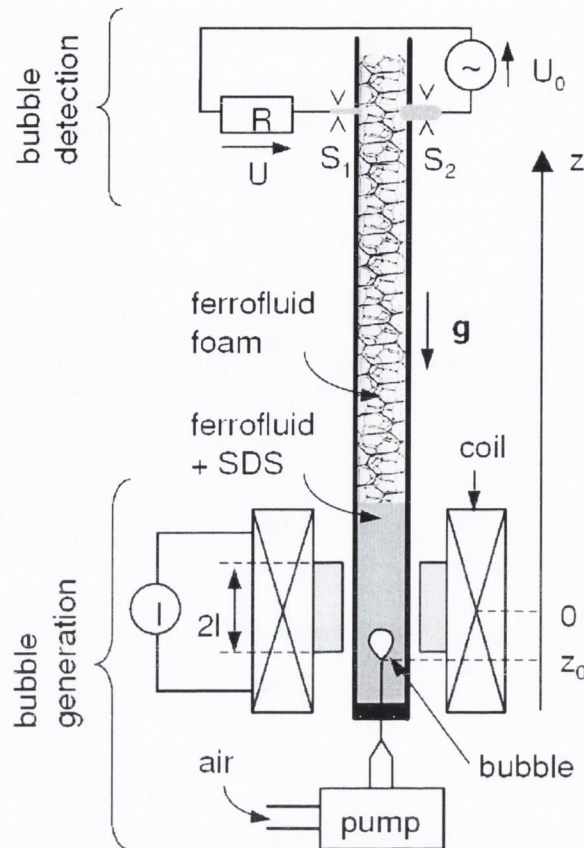
Figure 8.1: Bubbles are generated by blowing air at a constant flow rate through a nozzle into a ferrofluid pool at the bottom of a vertical Plexiglas tube. The nozzle is placed into a horizontal magnetic field created by two coils fitted with soft iron cores. At the top of the tube the local resistance of the generated foam structure is measured between two electrodes of different cross-section in contact with the foam.

We have been able to show that an elegant solution to this problem is provided by injecting the gas into a ferrofluid-surfactant solution. The bubble volume can then be varied very accurately over up to 3 orders of magnitude by applying a magnetic field gradient during bubble production [39]. In the following we present data and a simple model, which describes the experimental results very well.

8.1.2   Experimental set-up and procedure

For the continuous phase of the foam, an ionic, water-based ferrofluid is used. In our case it is a dispersion of maghemite (γ-Fe2O3) colloidal particles in water at a volume fraction of 1.92 percent, stabilised by the presence of a negative electrostatic charge

at the surface of each particle [6]. In order to achieve the required foam stability, two percent (by weight) of sodium dodecyl sulfate (SDS) are added as surfactant. Fig. 8.1 shows the experimental set-up. The ferrofluid is injected into a vertical, cylindrical Plexiglas tube with an inner diameter of 7 mm. A monodisperse foam is produced by blowing air through a nozzle into the ferrofluid at a constant air flux Q_A of 10 ml/min using a micro pump. The bubbles order in the tube. The foam structure which is formed depends on the bubble volume (as shown in Fig. 6.2). These structures are observed by video imaging. Since each of them corresponds to a particular number of bubbles per unit cell, the bubble volume can be derived from the number of unit cells filling a chosen section of the tube.

A magnetic field gradient is generated in the region of bubble production by placing the nozzle along the vertical line through the center of a two-coil system (Fig. 8.1 and Fig. 8.2), supplied with a direct current I. The coils are fitted with soft iron cores of height $2l = 30$ mm, which form a gap of 12 mm. An air ventilation system prevents the ferrofluid solution from heating appreciably.

Fig. 8.2 shows the variation of the experimentally determined magnitude of the horizontal magnetic field $H(z)$ and its gradient between the two coils along the z-axis for $I = 2$ A. For $|z| < l$, $H(z)$ is roughly constant, whereas it decreases almost linearly with $|z|$ for $|z| \approx l$.

The nozzle is placed at different vertical positions z_0 in the magnetic field, and the variation of bubble volume with magnetic field strength is observed by varying the current through the coils. The effect of the strength of the current I on the bubble volume V is found to strongly depend on the location of bubble production. For $z_0 < -l$ the bubble volume increases with I, for $z_0 > +l$ it decreases with I, whereas it remains constant for $-l < z_0 < +l$. This indicates the important role of the field gradient in bubble size control. Above a critical current bubbles can even be observed to move downwards in the ferrofluid.

Fig. 8.3 presents data taken for different nozzle diameters d and different positions z_0 of bubble production within the region of positive field gradient ($z_0 < -l$). For the purpose of fitting and plotting the data, the bubble diameter D is used to represent bub-
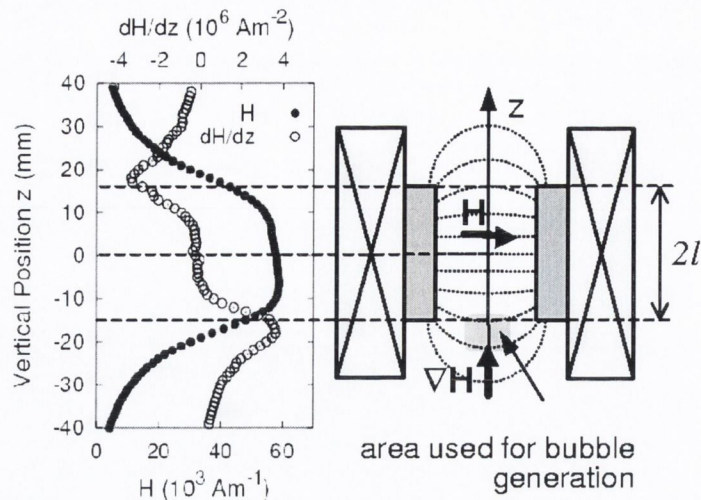
Figure 8.2: Magnetic field created by the pair of coils fitted with soft iron cores. On the right the shape of the field lines is sketched. The graph on the left shows the measured values of the amplitude of the horizontal magnetic field (full circles) and of the vertical magnetic field gradient (empty circles) along the z-axis for $I = 2$ A. The amplitude of the magnetic field and the amplitude of the magnetic field gradient are proportional to I. By placing the tip of the nozzle at the appropriate position a positive, negative or zero magnetic field gradient can be applied during the bubble formation.

ble size. As the current is varied between zero and 1.8 A, the bubble diameter is very reproducibly increased by a factor of up to three. Hysteresis is not observed. The range of accessible bubble volumes could in theory be much larger, since the bubble diameter diverges as the current approaches a value of about 1.8 A. However, the monodispersity of the foam decreases noticeably when the bubble diameter exceeds the tube diameter, and also when the bubble extends over a region of significant variation of the field gradient.

We did not quantitatively investigate the decrease of bubble volume with increasing current in the region of positive field gradient, as the bubble diameter decreases very quickly to a value smaller than the internal nozzle diameter. This leads to very irregular bubble volumes, probably due to the wetting of the internal nozzle boundary by the ferrofluid.

In order to investigate whether the demagnetising field of the ferrofluid (due to the magnetic dipolar interaction [101]) leads to a deformation of the bubble during formation, we conducted accompanying experiments of the same type using a Hele-Shaw cell

(a)

(b)
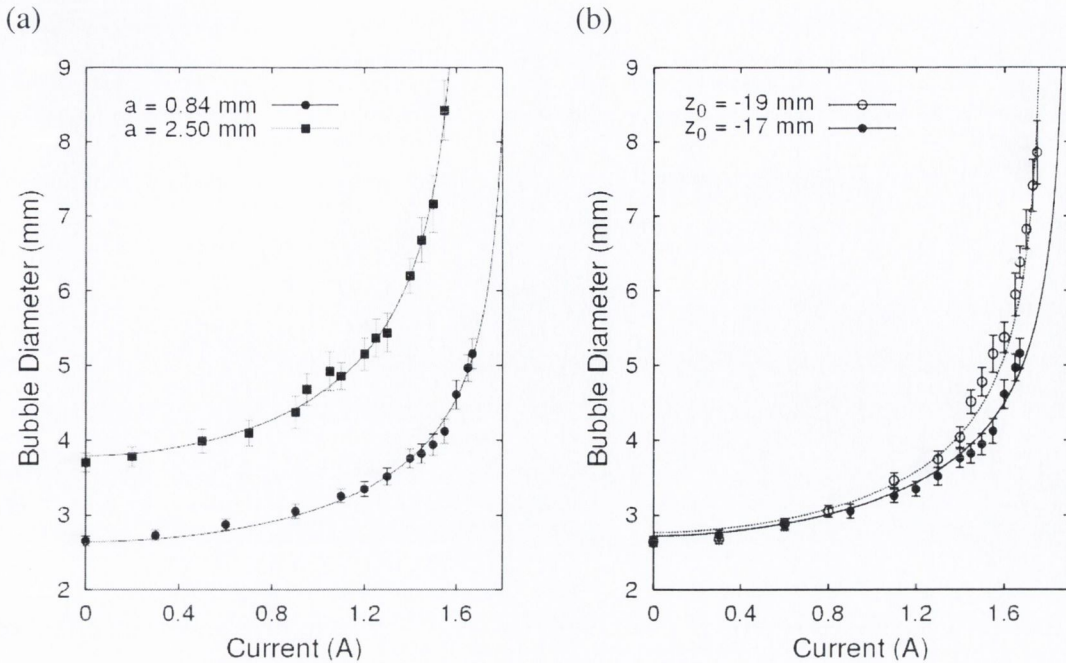
Figure 8.3: Bubble diameter D as a function of current through the coils at constant air flux for two different a) nozzle sizes a and b) positions z_0. The bubbles are generated in the region of positive field gradient. The lines represent the best fits of the data using equ. (8.10). a) The two data sets correspond to measurements with different nozzle diameters d at the same position $z_0 = -21$ mm. Circles: $d = 0.84$ mm, $\gamma f = 39.1 \times 10^{-3} \mathrm{Nm}^{-1}$ and $\partial_z \beta(z)|_{z_0} = 1.91 \times 10^6 \mathrm{Am}^{-1}$; Squares: $d = 2.5$ mm, $\gamma f = 38.4 \times 10^{-3} \mathrm{Nm}^{-1}$ and $\partial_z \beta(z)|_{z_0} = 2.26 \times 10^6 \mathrm{Am}^{-1}$; b) The two data sets correspond to measurements with the same nozzle ($d = 0.84$ mm) at different positions z_0. Empty circles: $z_0 = -19$ mm, $\gamma f = 42.8 \times 10^{-3} \mathrm{Nm}^{-1}$ and $\partial_z \beta(z)|_{z_0} = 1.53 \times 10^6 \mathrm{Am}^{-1}$; Full circles: $z_0 = -17$ mm, $\gamma f = 45.0 \times 10^{-3} \mathrm{Nm}^{-1}$ and $\partial_z \beta(z)|_{z_0} = 1.78 \times 10^6 \mathrm{Am}^{-1}$

instead of the Plexiglas tube. In this cell the ferrofluid is contained between two glass plates separated by a gap of one millimeter, thus forming a quasi-two-dimensional system, which allows easy observation of bubble shapes. Fig. 8.4 shows an example. Apart from the hydrodynamic deformation due to the rising of the bubble in the ferrofluid, no additional deformation could be observed, indicative of the negligible demagnetising effect of the ferrofluid.

8.1.3 Modelling and analysis

The effect of increasing bubble volume with magnetic field strength has already been reported for a quasi-two-dimensional cell containing ferrofluid submitted to a constant,
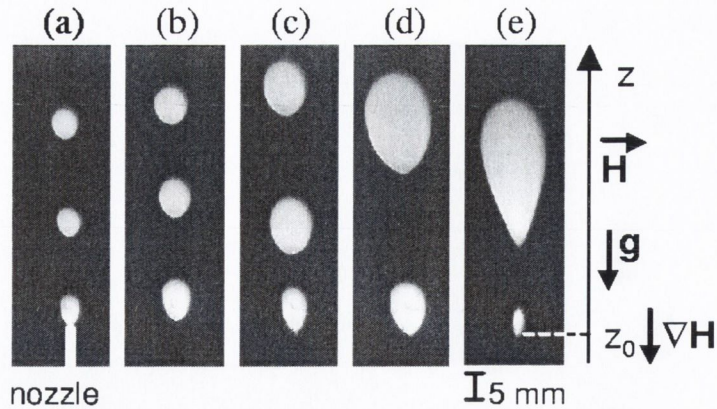
Figure 8.4: Variation of bubbles size and initial shape with current I through the coils in a Hele-Shaw cell (quasi-two-dimensional), which was placed between the coils. (a) $I = 0$; (b) $I = 1$ A; (c) $I = 2$ A; (d) $I = 3$ A; (e) $I = 4$ A.

perpendicular magnetic field [11]. This effect was, however, interpreted as an effect of magnetic dipole interaction between the magnetic particles.

In the present case a ferrofluid is used whose concentration of magnetic particles is small enough for the demagnetising energy to be negligible with respect to interfacial energy, as shown in our experiments in the Hele-Shaw cell. The influence of the magnetic field on the variation of bubble size then only depends on the existence of a magnetic force generated by a magnetic field gradient.

We develop a simple model of force balance, which very accurately reproduces the experimental data. The underlying idea is as follows. A magnetic field gradient generates a magnetic volume force on a bubble in a magnetic fluid [101]. Depending on the direction of the field gradient, the magnetic force results in the reduction or magnification of the effective buoyancy of the bubble, which changes the critical bubble volume required for the detachment of the bubble from the nozzle.

Since our experiments in the Hele-Shaw cell show that no noticeable deformation of the bubbles takes place in the magnetic field, dipolar interactions within the ferrofluid are neglected in the derivation of the bubble volume as a function of the system parameters. Furthermore, all derivations are considered in the quasi-static limit, which is provided experimentally by choosing a very low air-flux ($Q_A = 10$ ml/min) for bubble generation.

A bubble detaches from the nozzle when the interfacial force $\boldsymbol{F}_S$ between nozzle

and bubble, the buoyancy force F_G and the magnetic force F_M on the bubble equalise. The interfacial force can be described by

$$F_S = -\pi \gamma df_s e_z. \tag{8.3}$$

Here d is the diameter of the nozzle, γ is the surface tension of the air-ferrofluid interface, e_z is a unit vector pointing upwards, and f_S is a correction factor close to unity [3]. This is a rather crude model, but has proven sufficient for a very accurate description of the experiments conducted here.

The buoyancy force is given by

$$F_G = \Delta \rho g V e_z, \tag{8.4}$$

where $\Delta \rho$ is the density difference between the continuous (ferrofluid) and dispersed (air) phase, g is the gravitational acceleration and V is the volume of the bubble.

The derivation of the magnetic force on the bubble requires a closer look at the physical properties of the ferrofluid - bubble system. The maghemite particles in the ferrofluid carry a permanent magnetic moment. In response to an applied magnetic field, thermal agitation competes with the magnetic energy, which tends to align the particles in the same direction as the external field. The resulting macroscopic magnetic behavior of the solution is of paramagnetic type, the magnetisation $M(H)$ of the ferrofluid having the same direction as the applied field H. $M(H)$ was experimentally determined using a Foner device [7]. The obtained data for the magnetisation, see Fig. 8.5, can in principle be described by a Langevin model, taking into account the polydispersity of the particles [10]. However such a model does not give an analytical expression for the magnetisation, making further derivations difficult. Alternatively, the experimental data can be fitted very accurately using the empirical expression:

$$M(H) = \frac{\chi M_S H}{M_S + \chi H} \tag{8.5}$$

where χ and M_S are the magnetic susceptibility and the saturation magnetisation of the solution respectively. In our case: $\chi = 0.176 \pm 0.001$ and $M_S = 5230 \pm 10$ Am^{-1}.
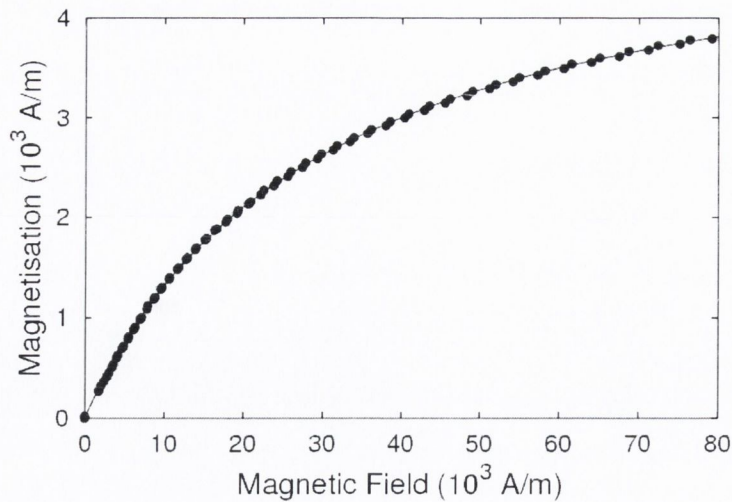
Figure 8.5: magnetisation of the ferrofluid-surfactant solution as a function of the applied external magnetic field, performed using a Foner device [7]. Solid line: best fit of data using Equ. (8.5).

The magnetic force on the bubble can be found by noting that a non-magnetic bubble inside a magnetic fluid of magnetisation $M(H)$ is physically equivalent to a magnetic bubble of magnetization $-M(H)$ inside a non-magnetic fluid [111, 112]. Therefore, the magnetic force acting on the bubble is given by [101]

$$\boldsymbol{F}_M = -\mu_0 V (\boldsymbol{M}(\boldsymbol{H}) \cdot \nabla) \boldsymbol{H}. \tag{8.6}$$

In the region of bubble generation, the vertical components of the magnetic field and the ferrofluid magnetisation are negligible in comparison to their horizontal components. Using furthermore the Maxwell Equ.s $\nabla \times \boldsymbol{H} = 0$ and $\nabla(\boldsymbol{M} + \boldsymbol{H}) = 0$, the magnetic force on the bubble can be written as:

$$\boldsymbol{F}_M = -\mu_0 V M(H) \frac{\partial H(z, I)}{\partial z} \boldsymbol{e}_z, \tag{8.7}$$

where $H(z, I)$ is the magnetic field strength as a function of position z and current I through the coils. Although local horizontal forces occur in the system, they can be neglected in the derivation. For symmetry reasons they would only slightly deform the bubble but not result in a net force on it.

z	vertical position
z_0	position of the nozzle
I	current through the coils
γ	surface tension of the ferrofluid - SDS solution
d	internal nozzle diameter
$\Delta\rho$	density difference between air and ferrofluid
g	gravitational acceleration
f_S	correction factor (close to unity)
μ_0	constant of magnetic permeability
χ	magnetic susceptibility of the ferrofluid (in low fields)
M_S	saturation magnetization of the ferrofluid
$\beta(z)$	coefficient relating the coil current I and local magnetic field strength H

Table 8.1: Overview of variables used in this section.

Since $H(z, I)$ is proportional to I it can be written as

$$H(z, I) = \beta(z)I, \tag{8.8}$$

and

$$\frac{\partial H(z, I)}{\partial z} = \partial_z H(z, I) = \frac{\partial \beta(z)}{\partial z}I = \partial_z \beta(z)I, \tag{8.9}$$

where $\beta(z)$ depends on the position only and can be determined for the particular experimental set-up using a Hall-probe (see Fig. 8.2). Equating $\boldsymbol{F}_S + \boldsymbol{F}_G + \boldsymbol{F}_M = 0$ (Equ.s (8.3), (8.4) and (8.7)) and using Equ.s (8.8) and (8.8), allows to determine the bubble diameter as a function of nozzle position z_0 and the current I through the coils:

$$D(z_0, I) = \left(\frac{6}{\pi} V\right)^{\frac{1}{3}} = \left(\frac{6 \, d \, \gamma \, f_S}{\Delta\rho \, g - \mu_0 \, M(z_0, I) \, \partial_z \beta(z)|_{z_0} I}\right)^{\frac{1}{3}} \tag{8.10}$$

where $M(z_0, I)$ is given by Equ.s (8.5) and (8.9):

$$M(H) = \frac{\chi M_S \beta(z_0) \, I}{M_S + \chi\beta(z_0) \, I}. \tag{8.11}$$

Formula (8.10) is in accord with our experimental observations: the bubble diameter D increases with I when the gradient $\partial_z H(z, I)|_{z_0} > 0$ for $z_0 < -l$, it decreases with I when $\partial_z H(z, I)|_{z_0} < 0$ for $z_0 > -l$, whereas it remains constant when $\partial_z H(z, I)|_{z_0} = 0$ for $+l > z_0 > -l$. If the applied field gradient is positive, the bubble diameter diverges when the denominator in Equ. (8.10) tends to zero for a critical

current I_c, which corresponds to the situation where the magnetic and buoyancy force on the bubble equalize. In our experiments this is the case for $I_c \approx 1.8$ A. For currents above this value the magnetic force on the bubble is strong enough to force it to move downwards in the ferrofluid.

Equ. (8.10) is fitted to the data (8.3) using two fitting parameters: the product γf_S and the gradient $\beta(z)|_{z_0}$. This was necessary because neither of these values could be determined with sufficient accuracy. Although approximate values for $\beta(z)|_{z_0}$ were obtained from measurements of $\beta(z)$ using a Hall-probe (Fig. 8.2), they vary significantly with position across the region of bubble formation and were therefore only used as starting parameters in the fitting procedure. The fitted product γf_S is of the same order of magnitude for all sets of data, on average: $\gamma f_S = (41.3 \pm 3.1) \times 10^{-3}$ Nm^{-1}. This is a reasonable order of magnitude since $\gamma \approx 30 \times 10^{-3}$ Nm^{-1} for a solution of SDS in water [92], and f_S is of the order of unity [3]. The fitting results for $\beta(z)|_{z_0}$ (see caption of Fig. 8.3) are usually within 15 % of the experimentally obtained values.

8.1.4   Conclusions and outlook

We showed that the application of ferrofluids and magnetic field gradients provides a highly reliable and precise method for the generation of very monodisperse bubbles with volumes ranging over up to three orders of magnitude. A simple model of force balance can be used to predict these volumes to high accuracy, if the field gradient, the surface tension and the nozzle specific factor f_S are known for the system.

Even though demonstrated for gas bubbles, the introduced methods will equally apply to droplets.

A related application may be the use of an appropriate magnetic field gradient to precisely balance gravity, so that bubbles can be made free-floating in a ferrofluid. We have been able to do this experimentally for small bubble clusters. If this can be achieved with sufficient uniformity over large volumes, it will offer a convenient alternative to microgravity experiments in space or on parabolic flights [82, 124].

In general, the use of ferrofluid foams provides a new dimension of remote manipulation. Hutzler et al. [60] demonstrated, for instance, how appropriate magnetic fields

can trigger transitions between ordered foam structures or twist them.

The introduced methods of bubble volume control may only be appropriate for micro-litre bubbles. In order to go down to the nano-litre scale required by microfluidics, other methods may have to be invoked. This is because on this length scale surface tension forces dominate all processes. A very promising candidate is the capillary flow focusing method, based on the breakup of a gas ligament surrounded by a co-flowing liquid. This produces highly monodisperse nano-litre bubbles [50, 49].

8.2 Bubble detection

8.2.1 Introduction

Differences between the physical properties of the two phases of a foam or emulsion can be used for sample counting and sample volume measurements. There are a variety of properties to chose from: optical, acoustic or conductivity.

In this section we demonstrate how conductivity measurements in a foam can be applied for this purpose.

8.2.2 Experimental setup and procedure

In these experiments only the [100] ("bamboo", as in 6.2) and the [211] ("staircase", as in 6.2) structures are considered. We are still using ferrofluid foams. This is because their ionic nature makes them highly conductive; and we consider this work as an extension of the previous section. Any other (less fancy) conducting and foaming solution would suffice for these purposes.

Bubbles are continuously generated at the bottom of the vertical tube at a gas flux Q, which causes the foam structure to rise at a constant velocity (approximately 2.5mms^{-1} in our case). The local resistance R_F of the foam structure is measured indirectly by determining the voltage U across a reference resistance $R = 10 \text{ k}\Omega$, which is in series with R_F for an applied voltage $U_0 = 0.5$ V. For a sketch of the setup refer to Fig. 8.6. An alternating voltage (frequency: 10 kHz) is applied to avoid electrolysis at the electrodes, and a lock-in amplifier is used to measure the voltage U in phase
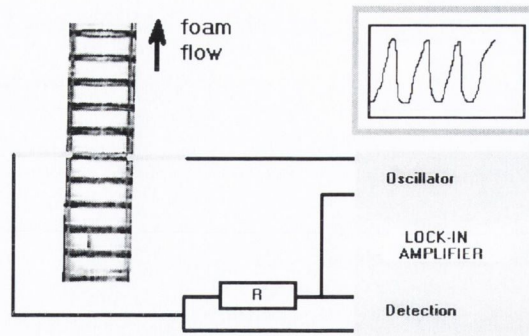
Figure 8.6: Two small electrodes implanted into a tube probe the local resistance of a foam structure.

with U_0. In order to achieve a sensitivity of the measurement to the foam structure, the electrodes have different cross-sections $S_1 = 1.1$ mm^2 and $S_2 = 12$ mm^2. They are made of conducting wire of diameters being smaller than the spacing between the Plateau borders of the foam structure.

8.2.3   Observations and interpretation

Foams contain a network of Plateau borders, which are formed where foam films meet or touch the container wall. Since the Plateau borders contain most of the liquid, foams can be considered equivalent to a network of conducting wires between the electrodes [125]. Since the cross-sections of the electrodes are smaller than the separation of the Plateau borders, the detected signal U reflects the structure of the foam. As the structures are periodic and flow within the tube at a constant velocity, the signal U is periodic in time, being superimposed upon a constant signal due to a conducting wetting film of ferrofluid around the inside of the tube. Typical data for the bamboo and staircase structures are displayed in Fig. 8.7. A peak in the electrical signal is recorded whenever a Plateau border is in contact with one or both of the electrodes. In the case of the bamboo structure, both electrodes are in contact with the same Plateau border at the same time, giving a regularly spaced sequence of identical spikes in conductivity (8.7 (I)). A more complicated signal characterises the staircase structure (Fig. 8.7 (II)). When one electrode touches a Plateau border, the other one is only in contact with the wetting film. This leads to the occurrence of two alternating peak heights in the
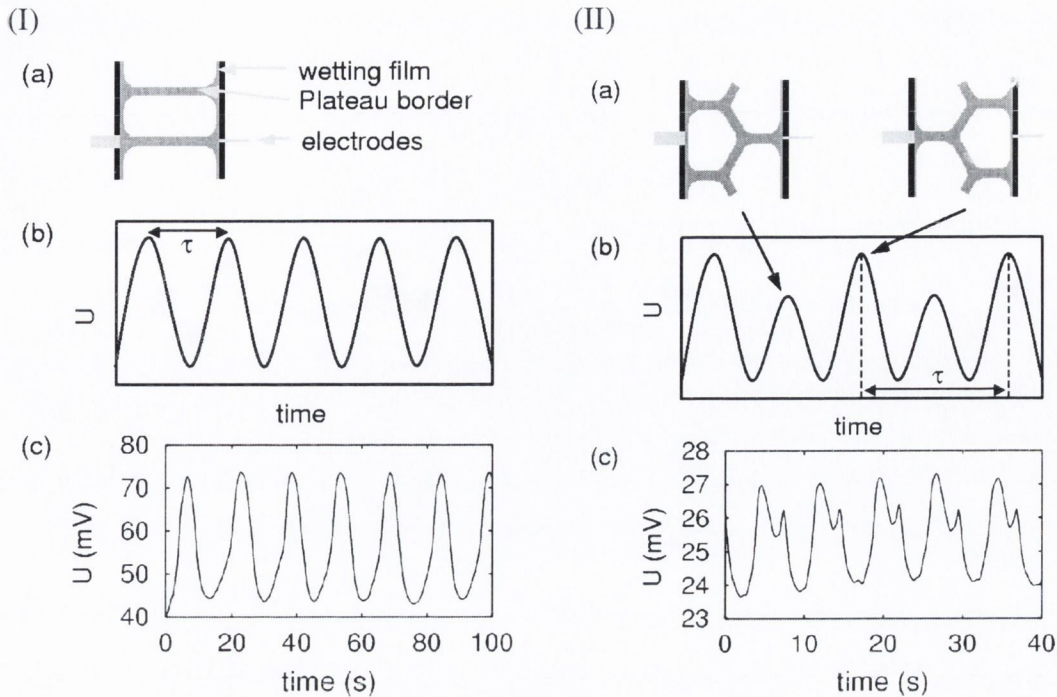
Figure 8.7: Signal U as a function of time obtained for the (I) bamboo and (II) staircase structure. I a) Configuration in the tube when the signal is at maximum; I b) Theoretically expected signal profile; I c) Experimentally detected signal. II a) The two possible configurations in the tube when the signal is at maximum - corresponding to two different peak heights; II b) Theoretically expected signal profile; II c) Experimentally detected signal. The deviation from the expected signal is due to the fact that the electrodes where not placed at exactly the same height in the tube.

periodic signal . The small peak is recorded when the smaller electrode is in contact with a Plateau border (Fig. 8.7 II(a) left), whereas the large peak corresponds to the case where the bigger electrode is in contact with a Plateau border (Fig. 8.7 II(a) right).

Since in both structures each peak in the signal corresponds to one bubble, threshold techniques can be applied for the counting of bubbles. Furthermore the period τ of the signal can be used to calculate the bubble volume V independently of the liquid fraction of the foam

$$V = cQ_A\tau, \tag{8.12}$$

where Q_A is the gas flux for bubble generation, and c is a structure dependent constant with $c = 1$ for the bamboo structure and $c = 1/2$ for the staircase structure.
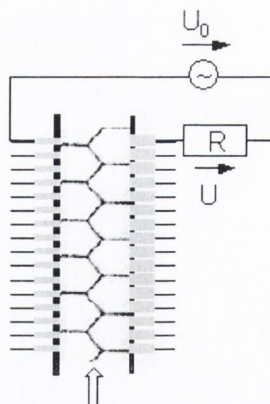
Figure 8.8: Possible setup for detection of the foam structure as a function of position in the channel by use of multiple electrodes.

In many applications it will be desirable to determine the bubble volume without taking into account the air flux. This could be achieved by using a set-up of several pairs of unequally sized electrodes along the tube or channel (see Fig. 8.8), which would allow the measurement of local conductivity of the structure versus position in the tube instead of versus time. However, when using this method, the liquid fraction of the structure has to be taken into account.

8.2.4   Conclusions and outlook

Bubbles can be detected in a straightforward manner by utilising the conductivity of the films separating them. These type of "clocking machines" can be combined with the bubble generation and manipulation in various feedback loops. Furthermore they can be used to trigger certain actions, for instance the removal or injection of bubbles at certain points in the channel network.

In many applications it will be important to probe the type of structure present in a channel without actually having to look into the channels. Multiple electrodes of various sizes may prove to be a practical solution to this problem, in particular because the evaporation of electrodes onto micro- and nano-chips is a commonly used and much tested technique today.

As already mentioned, there are various more physical properties waiting to be explored for this kind of purpose. Among them are, for instance, optical transparency
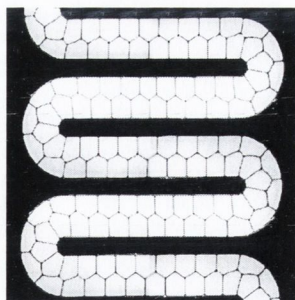
Figure 8.9: Example of a channel arrangment which could be used for sample storage and analysis purposes.

or the propagation of sound.

8.3 Sample storage and analysis

Traditional microfluidic systems lack an efficient connection between the microfluidic chip, the micro-assay (well plate) and sample storage. Our proposed technology solves this problem very naturally, as all three systems can be accommodated and easily connected by simply designing appropriate channel geometries for the required purposes.

Possible examples are plentiful. The most obvious geometry for a micro-assay and storage device would be a serpentine channel containing a single column of samples. Fig. 8.9 shows an example of this type of device with two rows of samples in the channel. Another promising possibility would be to arrange a spiraling channel on a chip of conventional CD format. This would allow to built on the knowledge and technology already developed for traditional CD purposes.

If the channel system is sealed properly and diffusion between samples prohibited, the system can be stored for a very long time. These timescales depend on the chemistry of the system.

Chapter 9

Conclusions and Outlook of part III

In this part of the thesis we introduced a novel method of sample manipulation for microfluidic applications, based on the interaction between ordered sample structures and channel geometries. We have termed this technology *Discrete Microfluidics*.

The proposed approach would have many advantages over current practice. We believe that it could not only solve several of the problems encountered in fluid/gas sample handling, but also has the potential to generate a plethora of exciting new possibilities of sample manipulation, analysis and storage. In an attempt to give an overview of the basic ideas of Discrete Microfluidics this thesis could only touch on most of these issues. Various aspects of the method will have to be thoroughly investigated in order to explore the feasibility of the proposed technology for the vast range of applications in this field.

Most importantly, we have to find out about possible problems entailed upon downscaling of the proposed methods to the scales required by microfluidics. We would like to emphasise, however, that not every promising application requires microfluidic dimensions. Even on millimeter scale we could envisage interesting opportunities, for instance in the production of medical pills, the analysis of environmental gas samples or blood samples.

The investigation of various surfactants will become a key issue for chemically sensitive applications. Chemists have provided the research community with a broad range of surface active molecules (ionic or non-ionic), from which the appropriate ones can be chosen. The food industry is a major driving force in developing foams

and emulsions stabilised by particles instead of molecules.

Associated with this aspect is the question of diffusion of chemicals between the samples. The continuous phase will have to be chosen very carefully to prohibit or reduce diffusion. In some cases, however, it might be of interest to allow a certain amount of controlled diffusion for mixing purposes.

For some applications it might be advantageous to use the continuous phase as sample material. The volume of the often expensive substances could then be reduced easily down to 0.5 % of the channel volume, whilst keeping reasonably big channels.

The implementation of magnetic fluids and specifically designed magnetic fields adds an additional exciting dimension of remote manipulation. We have demonstrated its usefulness for sample generation (§8.1). We could also show how using ferrofluids for the continuous phase allows to deform and twist sample structures, provoke transitions between them and to locally vary the volume fraction using magnetic fields [60].

In our simple, big-scale geometries it was possible to move the sample structures simply by applying a pressure at the inlet of the channel system. For more complicated networks on smaller scales this will not be sufficient. Alternative methods will have to be developed. These could either be based on methods already used in continuous or digital microfluidics, or exploit some of the particular strength of the discrete nature of our system. Magnetic fluids, for instance, could be employed to drive the structures through the channels using traveling magnetic fields. For this purpose, the magnetic fluids could either constitute the continuous phase or a certain number of the dispersed samples. These magnetic droplets could easily be added to and removed from an existing structure using, for instance, the method proposed in §7.4.3. Dielectric media in combination with electric fields might prove equally promising.

For future applications it will be essential to design methods for the controlled merging and splitting of samples. Using lasers to "pop" individual films between samples has proven very successful for foams. The development of channel sections with adjustable wetting properties may be just as promising. The splitting of samples has been successfully demonstrated using suspensions of low volume fraction in a pointy

Y-junction (like Fig. 7.2) with only one column of samples (bamboo structure) in the bigger channel.

The minimization of interfacial energy and the forces associated with it, could be utilized for various other aspects. One of the more obvious examples would be the design of valves. If a channel geometry is designed such that the interfacial area of a structure increases or decreases more quickly by moving into one direction than into the other, it could potentially be used as a rectifier.

In the long run it would be useful to create dynamic channel designs, which can change shape to adjust to the required task. For instance, the "bump" in the switching element in Fig. 7.3(c) could be varied in shape depending on whether sample columns have to switch sides or not. Again, magnetic fluids might be a very promising candidate for this purpose.

To sum up: we to have introduced basic concepts of very exciting and commercially attractive tools for the handling of small liquid and gas samples. We have been able to demonstrate their key features and are looking forward to exploring the vast landscape of scientific and applied opportunities opening up in front of us.

Appendix A

Drainage in a solidifying metal foam

A.1   Introduction

In the metallic foam fabrication process developed by the Fraunhofer Institute (Bremen) [9], a foaming liquid metal is frozen to create a solid metallic foam. The MetFoam program models this process, to enable the prediction of quantities such as freezing time and the degree of inhomogeneity in terms of the physical parameters for a particular system. A screenshot of the software tool is shown in Fig. A.1.

The simulation starts from a state where the foam is fully expanded and molten, and then models the process of solidification. Since the foam cannot solidify instantaneously, there must be a certain amount of drainage which makes the solid foam inhomogeneous. For an in-depth discussion of the mathematics and the necessary physical assumptions, the user is referred to the publication [29]. We give here a brief synopsis to enable the interested user to make a start in applying the package to his particular situation.
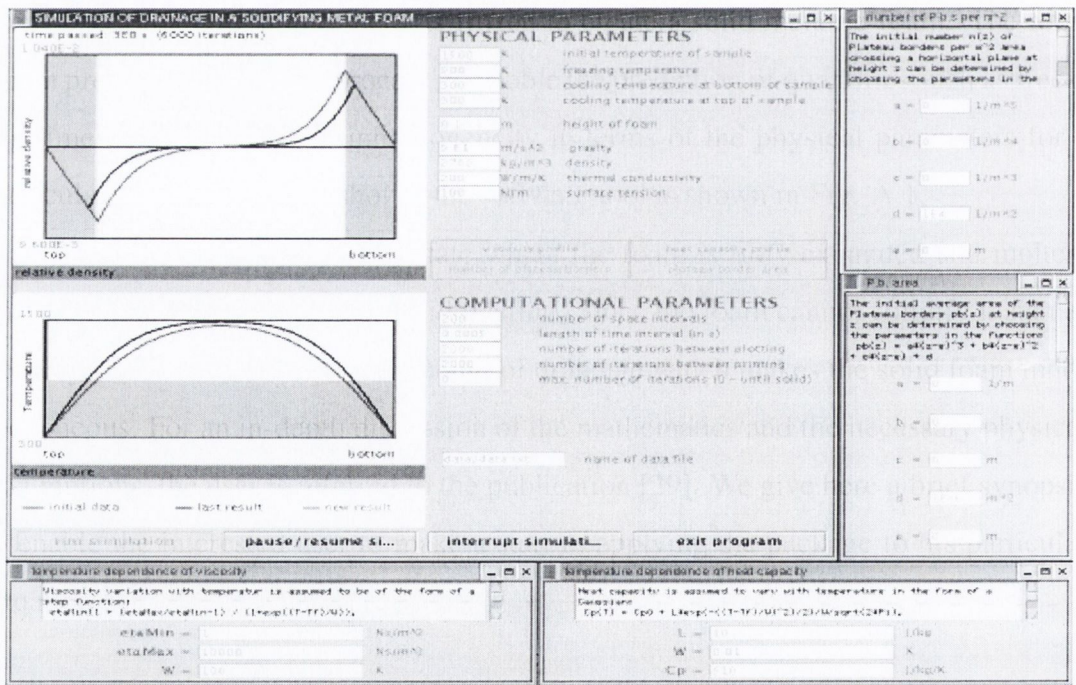
Figure A.1: Screenshot of the "MetFoam" software tool. It allows the user to input a broad range of parameters to simulate the competing drainage and solidification process in a metal foam.

A.2   Theory

In the simulation the foam drainage equation [119, 125, 128]

$$\frac{\partial \phi_l}{\partial t} + \frac{\partial (\phi_l u)}{\partial z} = 0 \tag{A.1}$$

and the heat flow equation

$$\rho \phi_l C_p \left(\frac{\partial T}{\partial t} + u \frac{\partial T}{\partial z} \right) = \frac{\partial}{\partial z} \left(\kappa \phi_l \frac{\partial T}{\partial z} \right) \tag{A.2}$$

with liquid fraction

$$\phi_l = NA \tag{A.3}$$

and liquid flow velocity

$$u = \frac{1}{150\eta} \left(\rho g A - \left(\sqrt{3} - \frac{\pi}{2} \right) \gamma \frac{1}{2\sqrt{A}} \frac{\partial A}{\partial z} \right) \tag{A.4}$$

are simultaneously solved for one dimensional solidification and drainage using a finite difference method. For the meaning of the variables refer to table A.1.

The program allows the input of the physical parameters given in table A.2. Table A.3 summarises the various pop-up menus which can be used to specify the initial profiles of viscosity, heat capacity and Plateau border distribution. The default values used in the program are approximately those of pure aluminium. About the values used for viscosity and surface tension needs to be said that they are not well known as the influence of additives and oxidation in the foam production is not fully understood. The computational parameters in table A.4 are those which can be adjusted. In particular, reducing Δx or Δt (but keeping the ratio $\Delta x/\Delta t$ small) will generally improve stability at the expense of increasing computational time.

A.3   Assumptions

A.3.1   Viscosity

The variation of the metal's viscosity with temperature is represented by a step function

$$\eta(T) = \eta_{min} + \frac{\eta_{max} - \eta_{min}}{1 + \exp\left((T - T_f)/W_\eta \right)}, \tag{A.5}$$

symbol	explanation
t	time
z	position ($z = 0$ at top of foam)
ρ	metal density
g	gravity
κ	thermal conductivity of metal
$T(z, t)$	temperature (in Kelvin)
$A(z, t)$	average Plateau border area at height z
$N(z)$	number of Plateau borders per unit area
	crossing horizontal plane at height z
$\phi_l(z, t)$	relative density of foam
$u(z, t)$	fluid velocity
$\eta(T)$	viscosity of metal (see §A.3.1)
$C_p(T)$	specific heat capacity at constant pressure (see §A.3.2)

Table A.1: Variables used in solving the drainage and solidification equations.

quantity	symbol	unit	default value
initial temperature		K	1500
freezing temperature	T_f	K	900
cooling temperature at bottom		K	300
cooling temperature at top		K	300
foam height		m	0.1
gravity	g	$m s^{-2}$	9.81
metal density	ρ	$kg\,m^{-3}$	2700
thermal conductivity	κ	$W m^{-1} K^{-1}$	200
surface tension	γ	$N m^{-1}$	10

Table A.2: Physical parameters that can be manipulated in the program.

where the maximum (η_{max}) corresponds to the solid and the minimum (η_{min}) to the liquid state. The parameter W_η measures the range of temperature over which the viscosity changes between η_{max} and η_{min}. T_f is the freezing temperature of the metal. The parameters η_{max} (etaMax), η_{min} (etaMin) and W_η (W) can be chosen in the program in a separate window that appears after clicking the "viscosity profile" button.

The default values used in the program are:

$$
\begin{array}{lcl}
\eta_{max}\ (\text{etaMax}) & 10^4 & N s\,m^{-2} \\
\eta_{min}\ (\text{etaMin}) & 1 & N s\,m^{-2} \\
W_\eta\ (\text{W}) & 10 & K^{-1}
\end{array}
$$

quantity	symbol	unit	note
viscosity of metal	$\eta(T)$	$Ns\,m^{-1}$	see §A.3.1
specific heat capacity of metal	C_p	$Jkg^{-1}K^{-1}$	see §A.3.2
average number of Plateau borders per unit area at height z	N	m^{-2}	see §A.3.3
average Plateau border area at height z	$A(z,t)$	m^2	see §A.3.4

Table A.3: The available commands for setting initial profiles.

number of space intervals	each of length Δx
length of time interval (in s)	length of time step Δt
number of iterations between plotting	number of finite difference steps between the re-plotting of the graphs
number of iterations between printing	number of finite difference steps between writing data into file
maximum number of iterations	the simulation will be interrupted after this number of finite difference steps, if you choose 0 (default value) the simulation will run until the foam is frozen
file name	The data (parameters, z, ϕ_l, A, T, N, η, C_p) is written into this file, which will be stored in the "data" directory of the MetFoam program. Be careful: choosing a file name that already exists will result in OVERWRITING the old one.

Table A.4: Computational parameters that can be manipulated in the program.

A.3.2 Heat Capacity

The temperature dependence of the heat capacity (at constant pressure) is chosen to be of the shape of a Gaussian

$$C_p(T) = C_p^0 + \frac{L_f}{W_{C_p}\sqrt{2\pi}}\exp\left(-\frac{(T-T_f)^2}{2W_{C_p}^2}\right), \qquad (A.6)$$

where the peak represents the latent heat of freezing. C_p^0 is the heat capacity away from the freezing point, L_f the latent heat of freezing and T_f the freezing temperature of the metal. W_{C_p} determines the width of the peak. The parameters C_p^0 (Cp), L_f (L)

and W_{C_p} (W) can be chosen in the program in a separate window that appears after clicking the "heat capacity profile" button.

The default values used in the program are:

$$
\begin{array}{lrl}
L_f \text{ (L)} & 3.78 \times 10^5 & Jkg^{-1} \\
W_{C_p} \text{ (Wc)} & 10 & K \\
C_p^0 \text{ (Cp)} & 900 & Jkg^{-1}K^{-1}
\end{array}
$$

A.3.3   Initial Profile of Number of Plateau Borders per Unit Area

The initial profile of the number of Plateau borders $N(z)$ crossing a horizontal plane at height z per unit area relate to the bubble size distribution in the sample. In the program the general cubic function

$$N(z) = a(z - e)^3 + b(z - e)^2 + c(z - e) + d \tag{A.7}$$

is provided, which can be used to generate a variety of initial profiles by manipulating the parameters a,b,c,d and e .

The default values used in the program are for a constant profile:

$$
\begin{array}{llll}
a: & 0 \quad m^{-5} & d: & 10^4 \quad m^{-2} \\
b: & 0 \quad m^{-4} & e: & 0 \quad m \\
c: & 0 \quad m^{-3} &
\end{array}
$$

A.3.4   Initial plateau border area

The initial profile of the Plateau border area A(z) at height z can be chosen by manipulating the parameters of the cubic function

$$A(z) = a(z - e)^3 + b(z - e)^2 + c(z - e) + d. \tag{A.8}$$

The default values used in the program are those for a constant profile::

$$
\begin{array}{llll}
a: & 0 \quad m^{-1} & d: & 10^{-6} \quad m^2 \\
b: & 0 \quad - & e: & 0 \quad m \\
c: & 0 \quad m &
\end{array}
$$

A.4 Running the program

The program is written in Java (user interface) and C++ (calculations). It requires Java version 1.2 or later which is available for free download from

```
http://www.java.sun.com/   .
```

If you want to run the program under Windows use MetFoamWindows. If you want to run it under Linux use MetFoamLinux.

Because the program works with dynamically linked libraries you have to set the environment variable LD_LIBRARY_PATH to the MetFoamLinux/MetFoamWindows directory. If you are not sure how to do this, refer to appendix A.5.

To run the program make sure that the location of the java interpreter is in the search path of your computer, change into the MetFoamLinux/MetFoamWindows directory and type at the command prompt:

```
java MetFoamFrame
```

Before running the program you can choose a variety of parameters and profiles (refer to section A.2 and A.3).

A.5 How to set Environment Variables

A.5.1 Linux

The procedure for setting the environment variable depends on the shell you use. For example,

```
c-shell:   setenv LD_LIBRARY_PATH <path>/MetFoamLinux
ba-shell:  export LD_LIBRARY_PATH=<path>/MetFoamLinux
```

`<path>` is the path to the MetFoamLinux directory on your computer. If you do not want to set the variable every time you log on to your computer or change the shell, add the corresponding line to either your .cshrc (c-shell) or your .bashrc (ba-shell) file. The variable and its path should now appear in the list when you type `printenv` or `env`.

A.5.2 Windows

Open the command line tool (e.g. MS DOS Prompt) and type

```
set LD_LIBRARY_PATH=<path>\MetFoamWindows
```

where `<path>` is the path to the MetFoamWindows directory on your computer.

Appendix B

Inertial forces in the meandering rivulet

Here we give the detailed derivation of Equ. (4.8) from §4.3.2.2.

We choose the frame of reference to be that of the lab, with the x-coordinate parallel to gravity. For an illustration see Fig. B.1, for a summary of the variables used in this section refer to Table B.1.
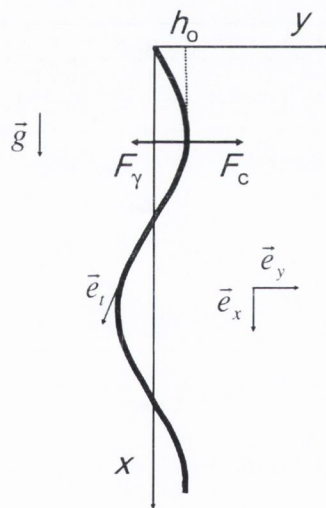
Figure B.1: Geometrical description of the meandering rivulet as sinusoidal wave. The frame of reference is chosen to be that of the lab.

Let us assume that the small-amplitude meandering rivulet of regime 2 (Fig. 4.8) can be approximated by a sinusoidal wave $h(x, t)$, with amplitude h_o

$$h(x, t) = h_o \, e^{i(kx - wt)}. \tag{B.1}$$

135

variable	description
x, y	Cartesian coordinates; reference frame is the lab; x is parallel to gravity
$\vec{e}_x, \vec{e}_y$	unit vectors along x and y
$\vec{e}_t$	unit vector along the tangential of the rivulet, $\vec{e}_t = \vec{e}_t(x, y)$
t	time
Q	flow rate
A_{PB}	area of the Plateau border cross-section
U	average velocity of the liquid flow in Plateau border
V	phase velocity of the travelling wave
κ	curvature of the rivulet
$h(x, t)$	wave form of the rivulet
h_o	amplitude of $h(x, t)$
k, w	wave vector and angular frequency the meander

Table B.1: Summary of variables used in this section

Here, t is time, and k and w are the wave vector and the angular frequency, respectively.

We take the rivulet to consist of two separate Plateau borders connected by a thin film (regime I in Fig. 4.2). This is the case for plate separations of $D > 1.4$ mm, which we determined by combining the experimental results for the flow rate Q_1 at the onset of the instability for various plate separations and the variation of the rivulet width W with flow rate Q. The amount of liquid flowing in the film is negligibly small in comparison to the contribution of the Plateau borders and is therefore neglected. The film therefore solely serves to provide a stabilising surface tension force.

Let us assume that the wave amplitude is small enough so that the average fluid velocity $u(x, t)$ can be taken as constant U along the rivulet. As a result of the constant flow rate Q applied at the top, this assumption leads to a constant area $a(x, t) = A_{PB}$ of the Plateau border cross-section, with

$$Q = 2A_{PB}\, U. \tag{B.2}$$

This basically means that we consider the rivulet to be of quasi-one-dimensional nature. Measurements of the variation of the the width of the undulating rivulet in the experiment confirm that this assumption is justified.

Let us look at the forces acting on a small section of the rivulet. The assumption

of small wave amplitudes allows us to neglect terms of second order in $h(x,t)$ in the following derivations.

The total velocity $\vec{v}(x,t)$ of a fluid element is given by the super-position of the liquid velocity and the horizontal motion of the rivulet:

$$\vec{v}(x,t) = U\,\vec{e_t} + \left.\frac{\partial h}{\partial t}\right|_x \vec{e_y} \tag{B.3}$$

with

$$\vec{t} = \vec{e_x} + ik\,h(x,t). \tag{B.4}$$

For the acceleration we therefore find

$$
\begin{aligned}
\vec{a} &= \frac{d\vec{v}}{dt}\\
&= U\left(\frac{\partial \vec{t}}{\partial t} + \frac{\partial \vec{t}}{\partial x}\frac{\partial x}{\partial t}\right) + \left(\frac{\partial^2 h(x,t)}{\partial t^2} + \frac{\partial^2}{\partial x \partial t}\frac{\partial x}{\partial t}\right)\vec{e_y}\\
&= (-\omega^2 + 2\omega k U - k^2 U^2)\,h(x,t)\,\vec{e_y}\\
&= -(\omega - kU)^2\,h(x,t)\,\vec{e_y}
\end{aligned}
\tag{B.5}
$$

Using the fact that the local curvature κ of the rivulet is given by

$$\kappa = \frac{\partial^2 h(x,t)}{\partial x^2} = -k^2 h(x,t), \tag{B.6}$$

and the phase velocity V (which we measure in the experiment) by

$$V = \frac{\omega}{k}, \tag{B.7}$$

we can rewrite the acceleration in Equ. B.5 as

$$
\begin{aligned}
\vec{a} &= -(V-U)^2\,k^2 h(x,t)\,\vec{e_y}\\
&= (V-U)^2\,\kappa\,\vec{e_y}.
\end{aligned}
\tag{B.8}
$$

This acceleration leads to a destabilising inertial force F_c (per unit length)

$$\vec{F_c} = 2A_{PB}\rho(V-U)^2\kappa\vec{e_y}, \tag{B.9}$$

which is Equation 4.8 from §4.3.2.2.

Bibliography

[1] *Lab-on-a-Chip: The Revolution in portable instrumentation*. John Wiley and Sons, 2 edition, 1997.

[2] *Microfluidics Technology and Applications*. Microtechnology and Microsystems Series. Research Studies Pr, 2000.

[3] A. W. Adamson. *Physical Chemistry of Surfaces*. John Wiley and Sons, New York, 4 edition, 1982.

[4] H. Aref and T. Herdtle. *Topological Fluid Mechanics*, page 745. Cambridge University Press, 1990.

[5] P. Atela, C. Golé, and S. Hotton. Phyllotaxis, an interactive site for the mathematical study of plant pattern formation. http://www.math.smith.edu/~phyllo.

[6] J.-C. Bacri, R. Perzynski, D. Salin, V. Cabuil, and R. Massart. Phase diagram of an ionic magnetic colloid: experimental study of the effect of ionic strength. *J. Colloid Interface Sci.*, 132:43, 1989.

[7] J.-C. Bacri, D. Salin, R. Perzynski, V. Cabuil, and R. Massart. Magnetic colloidal properties of ionic ferrofluids. *J. Magn. Magn. Mat.*, 62:36, 1986.

[8] P. Ball. *The Self-Made Tapestry: Pattern Formation in Nature*. Oxford University Press, 2001.

[9] J. Banhart. Foam metal: The recipe. *Europhys. News*, January/February:17–20, 1999.

[10] B Berkovski, editor. *Magnetic Fluids and Applications Handbook.* Begell House, New York, 1996.

[11] E. Blums, A. Cabers, and M. M. Maioron. *Magnetic Fluids.* Walter de Gruyter, 1999.

[12] F. Bolton and D. Weaire. The effects of plateau borders in the two-dimensional soap froth .ii. general simulation and analysis of rigidity loss transition. *Phil. Mag. B*, 65:473–487, 1992.

[13] M. J. Boussinesq. The application of the formula for surface viscosity to the surface of a slowly falling droplet in the midst of a large unlimited amount of fluid which is at rest and posesses a smaller specific gravity. *Ann. Chim. Phys.*, 29:357, 1913.

[14] L. Bragg and J. F. Nye. A dynamical model of a crystal structure. *Proc. R. Soc. Lond. A*, 190:474–481, 1947.

[15] Brakke. private communication, 2004.

[16] K. Brakke. The surface evolver. *Exp. Math.*, 1:141–156, 1992.

[17] F. P. Bretherton. The motion of long bubbles in tubes. *J. Fluid Mech.*, 10:166, 1961.

[18] R. Bruinsma. The statistical mechanics of meandering. *J. Phys. France*, 51: 829–845, 1990.

[19] I. Cantat and R. Delannay. Dynamical transition induced by large bubbles in two-dimensional foam flows. *Phys. Rev. E*, 67, 2003.

[20] I. Cantat, R. Delannay, and N. Kern. Dissipation in foam flowing through narrow channels. *Europhysics Lett.*, 65(5):726–732, 2003.

[21] J. M. Chomaz and B. Cathalau. Soap films as two-dimensional classical fluids. *Phys. Rev. A*, 41(4):2243–2245, 1990.

[22] T. Chovan and A. Guttman. Microfabricated devices in biotechnology and bio-chemical processing. *TRENDS in Biotechnology*, 20(3):116–122, 2002.

[23] S. Colin. Verrueckte fluide. *Spektrum der Wissenschaft*, pages 46–50, Januar 2004.

[24] Y. Couder, J. M. Chomaz, and M. Rabaud. On the hydrodynamics of soap films. *Pysica D*, 37:384, 1989.

[25] S. J. Cox, G. Bradley, S. Hutzler, and D. Weaire. Vertex corrections in the theory of foam drainage. *J. Phys. - Cond. Matter*, 13(21):4863–4869, 2001.

[26] S. J. Cox and F. Graner. Large two-dimensional clusters of equal-area bubbles. *Phil. Mag.*, 83:2573–2584, 2003.

[27] S. J. Cox and F. Graner. Large two-dimensional clusters of equal-area bubbles: the influence of the boundary in determining the minimum-energy configuration. *Phil. Mag.*, 83:2573–2584, 2003.

[28] S. J. Cox, F. Graner, M. F. Vaz, C. Monnerau-Pittet, and N. Pittet. Minimal perimeter for n identical bubbles in two-dimensions: calculations and simulations. *Phil. Mag.*, 83:1393–1406, 2003.

[29] S.J. Cox, G. Bradley, and D. Weaire. Metallic foam processing from the liquid state: the competition between solidification and drainage. *Euro. J. Phys: Appl. Physics*, 14:87–97, 2001.

[30] J. O. Cruickshank and B. R. Munson. Viscous fluid buckling of plane and axisymmetric jets. *J. Fluid Mech.*, 113:221–239, 1981.

[31] J. B. Culkin. *Rivulet Meandering*. PhD thesis, North Western University, Chicago, 1982.

[32] J. B. Culkin and S. H. Davis. Meandering of water rivulets. *AIChE JL*, 30: 263–267, 1984.

[33] S. H. Davis. Moving contact lines and rivulet instabilities. part 1: the static rivulet. *J. Fluid Mech.*, 98:225–242, 1980.

[34] T. R. H. Davis and C. C. Tinker. Fundamental characteristics of stream meanders. *Bull. Geol. Soc. Am.*, 95:505–512, 1984.

[35] R. Delannay, 2004. private communication.

[36] N. Denkov, 2004. private communication.

[37] W. Drenckhan, S. Cox, H. Holste, D. Weaire, and N. Kern. Rheology of ordered foams - on the way to discrete microfluidics. to appear in *Colloids and Surfaces A*, 2005.

[38] W. Drenckhan, S. Cox, and D. Weaire. The demonstration of conformal maps with two-dimensional foams. *Eur. J. Phys.*, 25:429–438, 2004.

[39] W. Drenckhan, F. Elias, S. Hutzler, D. Weaire, E. Janiaud, and J.-C. Bacri. Bubble size control and measurement in the generation of ferrofluid foams. *J. Appl. Phys.*, 93(12):10078–10083, 2003.

[40] W. Drenckhan, S. Gatz, and D. Weaire. Wave patterns of a rivulet of surfactant solution in a hele-shaw cell. *Physics of Fluids*, 16(8):3115–3121, 2004.

[41] W. Drenckhan and D. Weaire. Flow in vertical plateau borders: a reluctance to coalesce. 2004. submitted to Eur. J. Phys.

[42] M. Durand and D. Langevin. Physicochemical approach to the theory of foam drainage. *Eur. Phys. J. E*, 7:35–44, 2002.

[43] D. A. Edwards, H. Brenner, and D. T Wasan. *Interfacial Transport Processes and Rheology*. Butterworth-Heinemann Series in Chemical Engineering. Butterworth-Heinemann,Stonheam,USA, 1991.

[44] F. Elias, J.-C. Bacri, F. H. deMougins, and T. Sprengler. Two-dimensional ferrofluid foam in an external force field: gravity arches and topological defects. *Phil. Mag. Letts.*, 79:389–397, 1999.

[45] D. Erickson and D. Li. Integrated microfluidic devices. *Analytica Chimica Acta*, 507:11–26, 2004.

[46] D. Exerova and P. M. Kruglyakov. *Foam and Foam Films; Theory, Experiment, Application*, volume 5 of *Studies in Interface Science*. Elsevier Science B.V., Amsterdam, Netherlands, 1998.

[47] R. Bel Fdhila and P. C. Duineveld. The effect of surfactant on the rise of a spherical bubble at high reynolds and peclet numbers. *Phys. Fluids*, 8:310, 1996.

[48] Procter & Gamble. http://www.scienceinthebox.com/index.html.

[49] A. M. Ganan-Calvo. Perfectly monodispers microbubbling by capillary flow focussing: An alternate physical describtion and universal scaling. *Phys. Rev. E*, 69(027301), 2004.

[50] A. M. Ganan-Calvo and J. M. Gordillo. Perfectly monodisperse microbubbling by capillary flow focussing. *Phys. Rev. Lett.*, 87(274501), 2001.

[51] M. Gharib and P. Derango. A liquid (soap film) tunnel to study two-dimensional laminar and turbulent shear flows. *Physica D*, 37:406–416, 1989.

[52] J. W. Gibbs. *The collected Works of J. Willard Gibbs*, volume 1. Yale University Press, New Haven, 1957.

[53] J. A. Glazier, S. P. Gross, and J Stavans. Dynamics of two-dimensional soap froths. *Phys. Rev. A*, 36:306–312, 1987.

[54] J. A. Glazier and D. Weaire. The kinetics of cellular patterns. *J. Phys.: Condens. Matter*, 4:1867, 1992.

[55] T. C. Hales. The honeycomb conjecture. *Discrete Comput. Geom.*, 25:1–22, 2001.

[56] F. K. Hansen and G. Rodsrud. Surface tension by pendant drop : I. a fast standard instrument using computer image analysis. *J. Colloid Interface Sci.*, 141: 1–12, 1991.

[57] A. L. Hazel and M. Heil. The steady propagation of a semi-infinite bubble into a tube of elliptical or rectangular cross-section. *J. Fluid Mech.*, 470:91–114, 2002.

[58] S. Hutzler, N. Peron, D. Weaire, and W. Drenckhan. The foams/emulsion analogy in structure and drainage. *Eur. Phys. J. E*, 14:381, 2004.

[59] S. Hutzler, D. Weaire, and R. Crawford. Moving boundaries in ordered cylindrical foam structures. *Phil. Mag. B*, 75:845, 1997.

[60] S. Hutzler, D. Weaire, F. Elias, and E. Janiaud. Juggling wih bubbles in cylindrical ferrofluid foams. *Phil. Mag. Lett.*, 82:297–301, 2002.

[61] ImageJ. `http://rsb.info.nih.gov/ij/`.

[62] E. Janiaud. *Elasticity, Morphology and Magnetic Drainage of liquid Foams*. PhD thesis, University of Paris 6, 2004. in french.

[63] I. L. Jashnani and R. Lemlich. Foam drainage, surface viscosity, and bubble size bias. *J. Colloid Interface Sci.*, 46:13–16, 1974.

[64] R. V. Jean. *Mathematical Approach to Patterns and Form in Plant Growth*. Wiley and Sons, New York, 1984.

[65] A. Kabla and G. Debregeas. Local sress relaxation and shear banding in a dry foam under shear. *Phys. Rev. Lett.*, 90, 2003.

[66] H. Kellay, X. L. Wu, and W. Goldburg. Experiments with turbulent soap films. *Phys. Rev. Lett.*, 74:3975–3978, 1995.

[67] J. Kern. Zur hydrodynamik der rinnsale. *Verfahrenstechnik*, 3:425–430, 1969.

[68] J. Kern. Stabilitätsprobleme der rinnsalströmung. *Verfahrenstechnik*, 5:289–294, 1971.

[69] N. Kern, D. Weaire, A. Martin, S. Hutzler, and S. J. Cox. The two-dimensional viscous froth model for foam dynamics. in print in Phys. Rev. E.

[70] H.-Y. Kim, J.-H. Kim, and B. H. Kang. Meandering instability of a rivulet. *J. Fluid Mech.*, 498:245–256, 2004.

[71] S. A. Koehler, S. Hilgenfeldt, and H. A. Stone. Liquid flow through aqueous foams: The node-dominated foam drainage equation. *Pys. Rev. Lett.*, 82(21): 4232–4235, 1999.

[72] S. A. Koehler, S. Hilgenfeldt, and H. A. Stone. A generalized view of foam drainage: Experiment and theory. *Langmuir*, 15(15):6327–6341, 2000.

[73] S. A. Koehler, S. Hilgenfeldt, E. R. Weeks, and H. A. Stone. Drainage of single plateau borders: Direct observation of rigid and mobile interfaces. *Phys. Rev. E*, 66, 2002.

[74] V. Yu. Kolosov. Nontranslation atom ordering in crystals growing in amorphous films. In G. Chapius, editor, *Aperiodic'94*, page 26. World Sci. Publ. Co., 1995.

[75] A. M. Kraynik. Foam flows. *Annual Rev. Fluid Mech.*, 20:325–357, 1988.

[76] L. J. Kricka. Microchips, microarrays, biochips and nanochips: personal laboratories for the 21st century. *Clinica Chimica Acta*, 307:219–223, 2001.

[77] P. S. Laplace. *Mécanique Céleste*. 1906. supplement to Book 10.

[78] R. A. Leonard and R. Lemlich. A study of interstitial liquid flow in foam. *AIChE*, 11:18–25, 1965.

[79] V.G. Levich. *Physicochemical Hydrodynamics*. Englewodd Cliffs, New Jersey, 1969.

[80] M. Mancini and C. Oguey. Foams at solid boundaries: equations and symmetries. Poster at EUFOAM 2004, 2004.

[81] C. Marangoni. Ueber die ausbreitung der tropfen einer fluessigkeit auf der oberflaeche einer anderen. *Ann. Phys. (Leipzig)*, 143:337–354, 1871.

[82] C. Monnereau, M. Vignes-Adler, and B. Kronberg. The influence of gravity on foams. *J. Chem. Phys.*, 96:958, 1999.

[83] S. Mouradian. Lab-on-a-chip: applications in proteomics. *Curr. Opinion Chem. Biol.*, 6:51–56, 2001.

[84] K. J. Mysels, K. Shinoda, and S. Frankel. *Soap Films, Studies of their Thinning*. Pergamon Press Ltd., New York, 1059.

[85] T. Nakagawa. Rivulet meanders on a smooth hydrophobic surface. *Int. Journal Multiphase Flow*, 18(3):89–99, 1984.

[86] T. Nakagawa and J.C.Scott. Stream meanders on a smooth hydrophobic surface. *J. Fluid Mech.*, 149:89–99, 1984.

[87] Z. Nehari. *Conformal mapping*. Dover Publications, New York, 1975.

[88] A. V. Nguyen. Liquid drainage in single plateau borders in foams. *Journal of Colloid and Interface Science*, 249:194–199, 2002.

[89] V. A. Nierstrasz and G. Frens. Marginal regeneration in thin vertical films. *J. Colloid Interface Sci.*, 207:209–217, 1998.

[90] M. P. Paidoussis. *Fluid-Structure Interactions*, volume 1. Academic Press, 1998.

[91] P. Paik, V. K. Pamula, and R. B. Fair. Rapid droplet mixers for digital microfluidic systems. *Lab on a Chip*, 3:253–259, 2003.

[92] A. Patist, V. Chhabra, R. Pagidipati, R. Shah, and D. O. Shah. Effect of chain length compatibility on micellar stability in sodium dodecyl sulfate/alkyltrimethylammonium bromide solutions. *Langmuir*, 13:432, 1997.

[93] S. Perkowitz. *Universal foam: the story of bubbles from cappucino to the cosmos*. Walker & Co, New York, 2000.

[94] N. Pittet, N. Rivier, and D. Weaire. Cylindrical packing of foam cells. *Forma 10*, 10(1):65–73, 1995.

[95] J. A. F. Plateau. Experimental and theoretical researches into the figures of equilibrium of a liquid mass without weight viii. researches into the causes upon which the easy develompent of the persistence of liquid films depend. – on the superficial tension of liquids. – on a new principle relating to the surfaces of liquid. *Phil. Mag.*, 38:445–455, 1869.

[96] L. Prandtl and O.G. Tietjens. *Applied hydro- and aeromechanics*. McGraw Hill, New York, 1934.

[97] R. K. Prudhomme and S. A. Khan, editors. *Foams; Theory, Measurement and Application*. Marcel Dekkar Inc., 1995.

[98] J. Ratulowski and H.-C. Chang. Transport of gas bubbles in capillaries. *Phys. Fluids A*, 1(10):1642–1655, 1989.

[99] N. Rivier, R. Occelli, J. Pantaloni, and A. Lissowski. Structure of bénard convection cells, phyllotaxis and crystallography in cyllindrical symmetry. *J. Physique*, 45:49–63, 1984.

[100] M. E. Rosa and M. A. Fortes. Nucliation and glide of dislocations in a monodisperse two-dimensional foam under uniaxial deformation. *Phil. Mag. A*, 77(6): 1423–1446, 1998.

[101] R. E. Rosensweig. *Ferrohydrodynamics*. Dover, New York, 1999.

[102] F. Rothen and P. Pierański. Mechanical equilibrium of conformal crystals. *Phys. Rev. E*, 53:2828–2842, 1996.

[103] F. Rothen, P. Pierański, N. Rivier, and A. Joyet. Cristaux conformes. *Eur. J. Phys.*, 14:227–233, 1993.

[104] A. I. Rusanov and V. A. Prokhorov. *Interfacial Tensiometry*, volume 3 of *Studies in Interface Science*. Elsevier Science B.V., Amsterdam, Netherlands, 1996.

[105] M. A. Rutgers, X. L. Wu, and W. B Daniel. Conducting fluid dynamics experiments with vertically falling soap films. *Review of Scientific Instruments*, 72(7): 3025–3037, 2001.

[106] Dukhin S. S., Kretschmar G., and Miller R. *Dynamics of Adsorbtion at Liquid Interfaces; Theory, Experiment, Application*, volume 1 of *Studies in Interface Science*. Elsevier, 1995.

[107] M. Safouane, M. Durand, A. Saint Jalmes, D. Langevin, and V. Bergeron. Aqueous foam drainage. role of the rheology of the foaming fluid. *Journal de physique IV*, 11:275–280, 2001.

[108] A. Saint-Jalmes, Y. Zhang, and D. Langevin. Quantitative describtion of foam drainage: Transitions with surface mobility. submitted, 2004.

[109] P. Schmuki and M. Laso. On the stability of rivulet flow. *J. Fluid Mech.*, 215: 125–143, 1990.

[110] L. W. Schwartz, H. M. Princen, and A. D. Kiss. On the motion of bubbles in capillary tubes. *J. Fluid Mech.*, 172:259–275, 1986.

[111] A. T. Skjeltorp. One- and two-dimensional crystallization of magnetic holes. *Phys. Rev. Lett.*, 51:2306, 1983.

[112] A. T. Skjeltorp. Monodisperse particles and ferrofluids: a fruit-fly model system. *J. Magn. Magn. Mat.*, 65:195, 1987.

[113] C. S. Smith. Grain shapes and other metallurgical applications of topology. In *Metal Interfaces*, pages 65–108. American Society for Metals, Cleveland. 1952.

[114] H. A. Stone, S. A. Koehler, S. Hilgenfeldt, and M. Durand. Perspectives on foam drainage and the influence of interfacial rheology. *J. Phys. - Cond. Matter*, 15: S283–S290, 2003.

[115] P. Tabeling. Some basic problems of microfluidics. In *14th Australasien Fluid Mechanics Conference*, 2001.

[116] B. Tchavdarov, A. L. Yarin, and S. Radev. Buckling of thin liquid jets. *J. Fluid Mech.*, 253:593–615, 1993.

[117] G. D. Towell and L. B. Rothfeld. Hydrodynamics of rivulet flow. *AIChE Jl*, 12: 972–980, 1966.

[118] D. J. Tritton. *Physical fluid dynamics*. Oxford University Press, Oxford, 2 edition, 1988.

[119] G. Verbist, D. Weaire, and A.M. Kraynik. The foam drainage equation. *J. Phys.: Condensed Matter*, 8:3715–3731, 1996.

[120] F. Vinet, P. Chaton, and Y. Fouillet. Microarrays and microfluidic devices: miniaturized systems for biological analysis. *Microelectronic Eng.*, 61–62:41–47, 2002.

[121] J. Walker. What forces shape the behaviour of water as a drop meanders down a windowpane? *Scient. Am.*, 253:132–137, 1985.

[122] D. Weaire. *The Kelvin Problem: foam structures of minimal surface area*. Taylor & Francis, London, 1996.

[123] D. Weaire. The equilibrium structure of soap froths: inversion and decoration. *Phil. Mag. Lett.*, 79:491–495, 1999.

[124] D. Weaire, S. J. Cox, S. Hutzler, and G. Bradley. Foams in microgravity. *J. Phys. IV France*, 11:Pr6–213–220, 2001.

[125] D. Weaire and S. Hutzler. *The Physics of Foams.* Clarendon Press, Oxford, 1999.

[126] D. Weaire, S. Hutzler, S. Cox, N. Kern, M. D. Alonso, and W. Drenckhan. The fluid dynamics of foams. *J. Phys.: Condens. Matter*, 15:65–73, 2003.

[127] D. Weaire, S. Hutzler, and N. Pittet. Cylindrical packings of foam cells. *Forma*, 7:259, 1992.

[128] D. Weaire, S. Hutzler, G. Verbist, and E. Peters. A review of foam drainage. *Advances in Chemical Physics*, 102:315–374, 1997.

[129] D. Weaire and R. Phelan. Optimal design of honeycombs. *Nature*, 367:123, 1994.

[130] D. Weaire and N. Rivier. Soap, cells and statistics–random patterns in two dimensions. *Contemp. Phys.*, 25:59–99, 1984.

[131] B. H. Weigl, R. L. Bardell, and C. R. Cabrera. Lab-on-a-chip for drug development. *Adv. Drug Delivery Rev.*, 55:349–377, 2003.

[132] R. H Weiland and S. H. Davis. Moving contact lines and rivulet instabilities. part 2: long waves on flat rivulets. *J. Fluid Mech.*, 107:261–280, 1980.

[133] H. Wong, C. J. Radke, and S. Morris. The motion of long bubbles in polygonal capillaries. part 1. thin films. *J. Fluid Mech.*, 292:71–94, 1995.

[134] H. Wong, C. J. Radke, and S. Morris. The motion of long bubbles in polygonal capillaries. part 2. drag, fluid pressure and fluid flow. *J. Fluid Mech.*, 292:95–110, 1995.

[135] Q. Xu and W. R. Rossen. Effective viscosity of foam in periodically constricted tubes. *Colloids and Surfaces A: Physicochem. Eng. Aspects*, 00:1–20, 2002.

[136] G. W. Young and S. H. Davis. Rivulet instabilities. *J. Fluid Mech*, 176:1–31, 1987.

[137] T. Young. An assay on the cohesion of fluids. *Phil. Trans. Roy. Soc.(London)*, 5:65–87, 1905.